The East Australian Potassic Suite: Petrology, Bulk Chemistry, and Origin

Anthony W. Lanati, Joshua J. Shea, Stephen F. Foley, Marthe Klöcking, Arno Rohrbach, and Stephan Klemme

Author affiliation, contact details, and ORCID information are on Page 2.

This preprint, originally submitted to EarthArXiv on 27.03.2025, is the final version before Editorial proofing.

It has been peer-reviewed and accepted for publication in ***Journal of Petrology****.*

Version: *3*

Date: *05.01.2026*

Revised draft for Journal of Petrology, 2025, pp. 1–68

doi:
Revised manuscript resubmitted for review

REVISED MANUSCRIPT RESUBMITTED FOR REVIEW

The East Australian Potassic Suite: Petrology, Bulk Chemistry, and Origin

Anthony W. Lanati[1,2*] Joshua J. Shea[3] Stephen F. Foley[2,4] Marthe Klöcking[1] Arno Rohrbach[1] and Stephan Klemme[1]

[1]Institut für Mineralogie, Universität Münster, 48149 Münster, Germany, [2]School of Natural Sciences, Wallumattagal Campus, Macquarie University, Sydney, NSW 2109, Australia, [3]Department of Earth Sciences, University of Cambridge, Cambridge CB2 3EQ, UK and [4]Research School of Earth Sciences, Australian National University, Acton, ACT 2601, Australia
[*]Corresponding author. a.lanati@uni-muenster.de

Abstract

The Eastern Australian Potassic Suite (EAPS) is an alkaline volcanic province made up of over 20 widely dispersed outcrops that extend almost 700 km, inferred to form the southern portion of the Cosgrove continental hotspot track. In contrast to the large basaltic volcanic complexes to the east and north, the EAPS occurs exclusively as mafic potassium–rich occurrences with inferred low–volume expressions with outcrop extents on the order of hundreds of metres to a few kilometres. These localities mostly occur on lithosphere thicker than 120 km suggesting that the lithosphere–asthenosphere boundary may have a strong influence on their depth of generation. The primary felsic mineral in these rocks is leucite, which has previously seen the EAPS defined as leucitites in constantly evolving classifications of exotic, but potentially economically significant alkaline rocks. However, this classification does not reflect their chemical or genetic affinity. In this study, we undertake a systematic re–evaluation of these occurrences with the aim of understanding their source enrichment processes and melting conditions. Newly acquired major, trace, and volatile element whole–rock data shows that the EAPS is chemically variable, but exceptionally enriched in potassium compared to other East Australian volcanism, with high K_2O/Na_2O and MgO (Av.: K_2O 4.98 wt%; K_2O/Na_2O 3.23; K/Na 2.12; MgO 12.14 wt%). We report the only complete volatile element data for the EAPS which show the lavas are similarly enriched in nitrogen compared to other lamproites, while being more CO_2-rich despite being partially degassed (N: 44–350 ppm; CO_2: 1129–10274 ppm). Despite not occurring on a craton, the EAPS trace element patterns and chemistry most closely resemble cratonic (anorogenic) lamproites. Additionally, the mineralogy, major and trace element concentrations closely match the classification criteria for lamproites. Trace element ratios of these near-primary mantle melts have a primitive signature generated from a highly enriched source that has previously undergone a degree of mixed silicate–carbonatite metasomatism. The most likely source for these rocks based on these new data is a hydrous phlogopite–bearing and olivine–poor assemblage that originates in the garnet stability field (i.e. phlogopite–garnet–pyroxenite). The inherited titanian affinity and elevated phosphorus contents of these magmas suggest apatite and oxide minerals were also present in the source. This new data helps inform interpretations of regional variations in melt generation and mantle source mineralogy in the highly heterogeneous metasomatised mantle beneath eastern Australia. We further suggest that the mechanisms that generated the EAPS likely include a combination of edge–driven convection and shear–driven upwelling as well as channelised melt flow which contributed to metasomatic depletion and refertilisation cycles. These cycles are synonymous with the initial stages of continental destabilisation that could develop toward rifting.

Key words: leucitite, lamproite, pyroxenite, potassic magmatism, intraplate volcanism, mantle metasomatism, Australia, Eastern Australian Volcanic Province

Introduction

Volcanism in Eastern Australia is dominated by large-volume basaltic eruptive centres ranging in age from late Mesozoic times to near present day (Johnson, 1989). This activity has recently been shown to have been generated from a chemically similar mantle source, forming a 3,000 km long volcanic province, the Eastern Australian Volcanic Province (EAVP; Shea et al., 2022). However, potassic and ultrapotassic magmatism of a similar age is also common, spanning over 25 volcanic expressions spread over approximately 700 km (Figure 1a,b), and

provides a unique insight into the geodynamic processes occurring beneath the Australian continental lithosphere. Potassium-rich mafic magmas (i.e. potassic magmas; where K_2O exceeds Na_2O, K/Na $\geq$1, and MgO $\geq$3 wt%) are comparatively rare globally, yet they are important in our understanding of melting and recycling processes in the mantle, including processes linked to the concentration of critical metals (Foley et al., 1987; Mitchell, 2021; Müller et al., 1992; Müller and Groves, 1993; Wang et al., 2006, 2022). Despite their relative scarcity when compared with tholeiites, alkaline magmas, and more specifically potassic magmas, are present in almost all tectonic settings and are believed to represent some of the first melts generated in magmatic provinces. They tend to be more enriched in volatile and moderately volatile elements such as water, carbon, nitrogen, sulfur and fluorine (Edgar et al., 1994; Ezad and Foley, 2022; Foley et al., 1987, 2022; Foley and Ezad, 2024; Pe-Piper and Piper, 1992; Pe-Piper et al., 2014; Prelević et al., 2004, 2005). Thus, they prove a useful tool to examine mass transfer processes such as metasomatism and incipient or partial melting in the mantle. However, due to the preferential mobility of alkali elements in low-temperature fluids, potassic volcanic rocks are susceptible to mineral-scale alteration and rapid breakdown of potassic minerals leading to a preservation bias (Ngwenya and Tappe, 2021; Putnis et al., 2007; Roux and Hamilton, 1976). Alkaline volcanic fields such as those in western North America and Europe (e.g. Sierra Nevada (USA), Roman Province (Italy), Western Mediterranean Lamproites (Spain)) are often used as natural laboratories for understanding metasomatic processes and the interdependencies between melting, metasomatism and tectonic and geodynamic conditions including cratonic, orogenic, and active subduction environments (Farmer et al., 2002; Elkins-Tanton and Grove, 2003; Lee et al., 2006; Lustrino et al., 2019; Prelević et al., 2005, 2007; Prelević and Foley, 2007; Prelević et al., 2008b, 2012, 2013). The Eastern Australian alkaline occurrences are similarly young ($<$ 35 Ma) and have yet to undergo significant alteration. Thus they represent a unique tectonic setting with elements of recent subduction and orogenic processes, potentially currently undergoing cratonisation. These rocks, however, are relatively unknown beyond the Australian geoscientific community and offer a unique opportunity to study these processes in an intraplate setting that exhibits a number of poorly understood phenomena.

In eastern Australia, volcanism was geographically expansive during the Cenozoic (Figure 1) while eruptions continued until roughly 5,000 years ago within the Newer Volcanic Province of Victoria in the south, and Kinrara in North Queensland (Blackburn et al., 1982; Cohen et al., 2017; Heath et al., 2020; Johnson, 1989; Smith and Prescott, 1987). The Newer Volcanic Province and the Cenozoic volcanism are both generally thought to be associated with plume activity due to a north–south age–progressive trend displayed in some of the volcanic regions (Cohen et al., 2008, 2013; Cundari et al., 1978; Davies et al., 2015; McDougall and Wellman, 1976; Sutherland, 1983; Wellman and McDougall, 1974). The alkaline magmas comprise a suite of leucite–bearing potassium-rich rocks known within the regional literature as the "New South Wales Leucitites", named for the state within which most of the rocks erupted (Figure 1b; Cundari, 1973; Davies et al., 2015; McQueen et al., 2007). While the vast majority of previous work centres on the basaltic volcanoes with compositions spanning tholeiitic through alkali basalt, information about the potassic fields is relatively sparse.

Within these potassic rocks, which we define here as the Eastern Australian Potassic Suite (EAPS), the presence of leucite as well as other potassic phases such as the amphibole K–richterite, sanidine, and most commonly phlogopite mica, gives rise to primitive melt compositions that are extremely enriched in K compared to basalts. Much like the basalts, these potassic lavas have been explained as plume–derived magmatism due to an apparent age progression when corrected for suspected erroneous ages (Cohen et al., 2008, 2013; Wellman and McDougall, 1974). Plume related genesis for the EAVP remains an open point of scientific interest with numerous recent geophysical studies investigating the mechanisms of magma generation, and a mechanism involving plume activity has not been excluded (Davies et al., 2015; Sutherland, 1983; Rawlinson et al., 2017).

The Cosgrove Track, as it is commonly known, spans over 2000 km of the Australian continent from Airlie Beach in far–north Queensland through central–western New South Wales and Victoria (Figure 1a–b; Davies et al., 2015; Sutherland, 1983). It comprises predominantly sub–aerial effusive volcanism of basaltic to basanitic composition within the volcanic fields of Hillsborough through to Buckland in Queensland

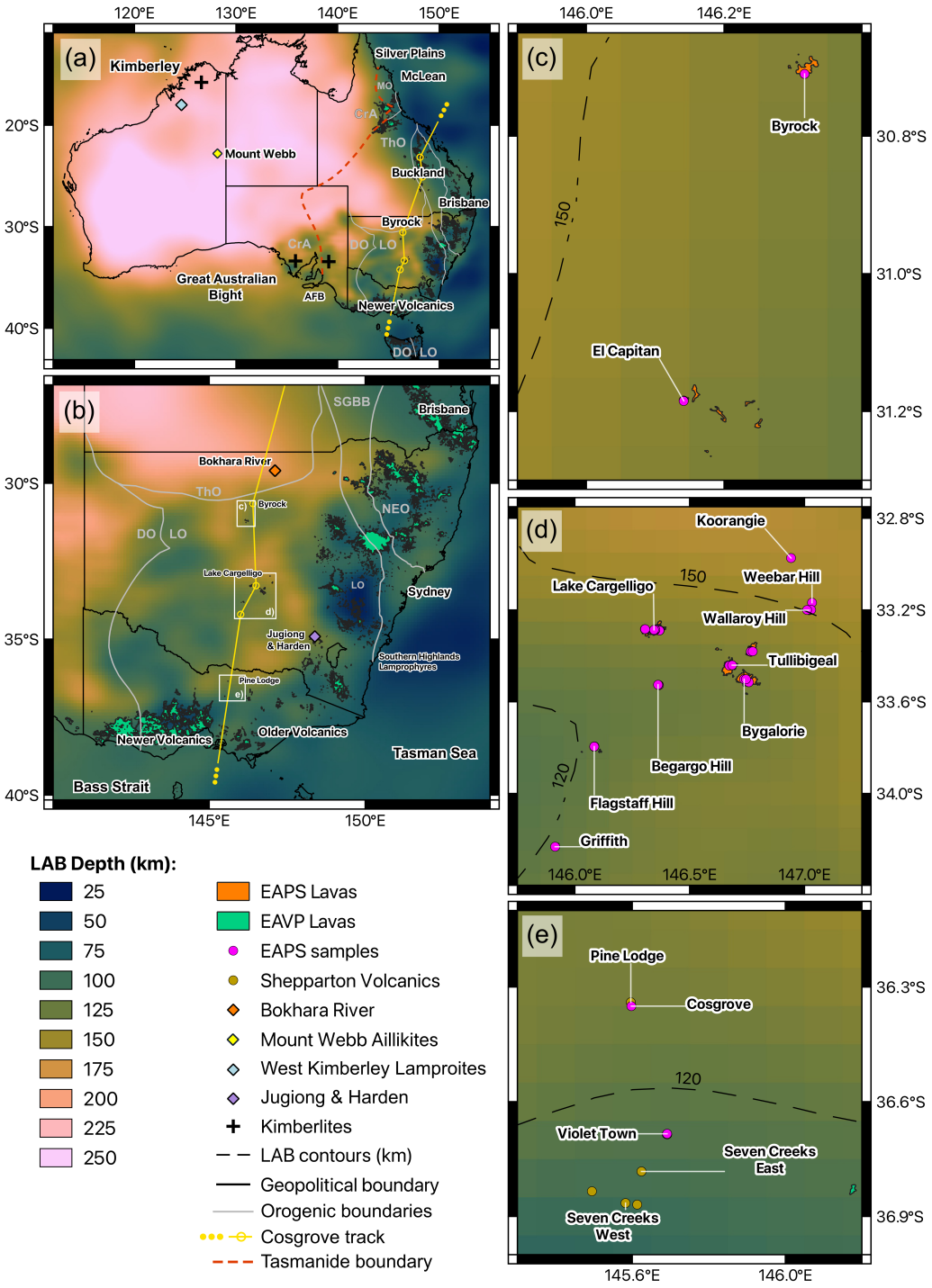

Fig. 1. (Caption next page.)

followed by a gap in volcanism of roughly 700 km until the next eruptive centre at Byrock at the northern end of the EAPS (Figure 1a Shea et al., 2022). The EAPS centres traverse the remainder of New South Wales and have been interpreted previously to extend into northern Victoria before a transition in both composition and eruptive style that straddles the geographic margin of the Older and Newer Volcanic Provinces (Heath et al., 2020; Shea et al., 2022). Geodynamically, this north–south sequence of volcanism has been used to link lithospheric architecture to compositional differences within the magmas as a function of plume–lithosphere interactions and mechanical processes such

Fig. 1. (a) Distribution of the EAVP (green) and EAPS (orange) outcrops as defined in Shea et al. (2022) and this contribution, respectively. Map coloured by depth of the lithosphere-asthenosphere boundary (LAB) from Rawlinson et al. (2017). Orogenic blocks (grey lines) and the western boundary of the Tasmanides (red dashed line) inferred to demarcate cratonic Australia to the west and orogenic Australia to the east from Glen et al. (2016); note mismatch to LAB depth where the 180 km contour is used by geophysical studies (Hoggard et al., 2020). Yellow line = the interpreted path of the Cosgrove plume (Davies et al., 2015) with inferred offshore progression of the plume (dotted line); open circles along the path mark the approximate locations of the outcrops with preferred ages as described in Cohen et al. (2008). (b) Zoom of Eastern Australia that also shows the location of the basanitic diatremes from Bokhara River (orange diamond) (Shea et al., 2024), leucite-bearing lavas at Jugiong and Harden (Harvey and Joplin, 1940), and EAPS sample areas (white boxes). Panels (c), (d), and (e) show the north, central and southern field areas and EAPS sample locations (pink circles) of this study. Dashed black lines = LAB contours at 120 and 150 km. These depths are commonly inferred to represent the depth of melting for the source assemblages of the leucite–bearing EAPS lavas. The volcanic fields around Shepparton from Paul et al. (2005) are included in (e), while the Mount Webb aillikites of Sudholz et al. (2023) are shown in (a) along with kimberlites of the Adelaide Fold Belt (*AFB*; Dalton et al., 2025), and Kimberley block kimberlites and *(Cenozoic)* West Kimberley lamproites (Jaques et al., 1984, 1986); the chemistry of these lavas are compared with the EAPS lavas in text. Abbreviations: Cratonic Australia (CrA); Delamarian orogen (DO); Lachlan orogen (LO); Mossman orogen (MO); New England orogen (NEO); Sydney–Gunnedah–Bowen basin (SGBB); and Thomson orogen (ThO).

as edge–driven convection (EDC) and shear–driven upwelling (SDU) (Davies et al., 2015; Duvernay et al., 2021, 2022; Manassero et al., 2024; Rawlinson et al., 2016, 2017). Other recent work has also highlighted the potential for volumetrically large changes in slab flux from subduction at the Tonga–Kermedec trench (3,500 km east of the EAPS) to influence magma generation in eastern Australia (Mather et al., 2020). The recent focus on geophysical interpretations has decoupled discussions of the EAPS genesis from the petrology of the magmatic sources and concentrated them on lithospheric architecture and mantle flow control. This is best exemplified by the observation that the northern– and southern–most portions of the Cosgrove track are on thin lithosphere of roughly 50 km thickness and erupt relatively normal basaltic compositions in contrast to the EAPS which erupts through much thicker lithosphere that exceeds 120 km and is in some cases up to 150 km (Figure 1a–e; Glen, 2005; Shea and Foley, 2019; Shea et al., 2022). Previous work in subduction–related magmatic arcs has correlated elevated K contents to an increased melting depth (Dickinson, 1975). However, this correlation was shown to be highly dependent on arc type and is likely more sensitive to source composition than depth of melting (Dickinson, 1975). To our knowledge, there is currently no published petrological explanation to demonstrate why leucite–bearing magmas would preferentially erupt through thicker lithosphere in an intraplate setting. Instead it is much more feasible that the distributions of leucite–bearing magmas both in Eastern Australia and globally is a function of favourable source mineralogy and melt extraction conditions (Bergman, 1987; Bracco Gartner et al., 2023, 2025; Foley et al., 1987; Fraser et al., 1985; Jaques et al., 1984, 1986; McCulloch et al., 1983; Mitchell and Bergman, 1991).

The last detailed appraisals of the EAPS were in the 1970s and 80s, and did not consider all of the mapped occurrences (Birch, 1976, 1978, 1980; Cundari, 1973; Cundari and Ferguson, 1982; Cundari and Salviulo, 1989). As such, there are a number of gaps in our understanding of the EAPS, their chemistry, and genesis. In this contribution we present the most complete set of modern whole–rock chemical analyses for the EAPS. We provide an updated classification of these rocks in line with the current understanding of alkaline rocks. Using this new data, we present a number of likely mechanisms for the formation of the EAPS, identify source assemblages, and isolate the most likely metasomatic agents.

Leucite–bearing Lavas in Eastern Australia

The vast majority of the leucite–bearing rocks in Eastern Australia occur as part of the "NSW leucitite suite" shown in Figure 1c and d. However, there are a number of other occurrences which are reported to contain leucite including at Harden and Jugiong (Harvey and Joplin, 1940), within a lamprophyre near Wollongong (Southern Highlands), and in far–north Queensland within the McLean Volcanic field (Figure 1a–b; Barron et al., 1996).

The first leucite–bearing volcanic occurrences in Australia were described by Judd and Curran in separate papers in 1887 focusing on the Byrock and El Capitan volcanoes (Figure 1b–c; Curran, 1888; David and Anderson, 1889; Judd, 1887). Both papers described the outcrops as leucite–basalts, and Curran noted that to his knowledge this was the first leucite–basalt described outside of the Wyoming and Roman

Leucitite fields. Further occurrences of leucite–bearing volcanics to the south of Byrock and El Capitan were identified in the Lake Cargelligo, Tullibigeal, and Condobolin areas (Figure 1d) and were classified as leucite–basalts, following the then established terminology (Browne, 1933; David and Anderson, 1889; Stonier, 1893). Curran (1891) was the first to undertake any microscopic assessment of the leucite–basalts, but it was not until Harvey and Joplin (1940) that detailed petrography and geochemical analyses were carried out. This work involved a summary of the mineralogy of a sample each from Byrock, El Capitan and Lake Cargelligo as well as descriptions and comparison of the whole rock major elements as determined by wet chemistry for these three samples with 17 others from around the world. These chemical analyses were the first analyses of EAPS rocks and, coupled with the comparison to other leucite and mica bearing volcanic rocks worldwide, led Harvey and Joplin to suggest that the NSW occurrences be called mica–leucite–basalts or, more generally, lamproites (Harvey and Joplin, 1940). In particular, the comparison was made to recently described lamproites of the West Kimberley in Western Australia by Prider and Wade (Prider, 1939; Wade and Prider, 1940) noting similar K_2O and MgO enrichment, but also similarly low SiO_2 and Na_2O shared between the EAPS and the West Kimberley lamproites (Harvey and Joplin, 1940). Furthermore, Harvey and Joplin (1940) noticed that K_2O/Na_2O of the EAPS was considerably higher than the average analysis of other leucite–basalts globally which, when coupled with the higher MgO and TiO_2 and the distinct mineralogy of the EAPS samples (i.e. abundant titanian poikilitic phlogopite) led to the conclusion that the NSW leucitites should be removed from the leucite–basalt grouping on both mineralogical and chemical basis.

The next examination of these samples saw the application of the name “olivine leucitite” to these rocks (Wellman et al., 1970), effectively ignoring the work and classification of Harvey and Joplin despite citing the paper. The samples were then classified by Aldo Cundari as melanocratic leucitites in a series of papers that examined the field, petrological, and geochemical characteristics of both the whole-rock and mineral compositions, including geochronological work that yielded ages of ∼14 Ma for Begargo Hill (Figure 1d; Cundari, 1973; Cundari et al., 1978; Cundari and Ferguson, 1982; Cundari and Salviulo, 1989). The most complete petrological and field description of the EAPS to date is given by Cundari (1973) and includes modal mineralogy, whole–rock, and selected mineral analyses by electron microprobe. Ewart et al. (1988) referred to the EAPS lavas as either ”high–potassium mafic regions”, or leucitites; confirming the classification given by Wellman and McDougall (1974) that has been used since. Ewart et al. (1988) also included the Pine Lodge basalt near the town of Cosgrove in northern Victoria as part of the series, based on the observation of leucite in the outcrop and the geochemical assessment by Birch (1976) and Birch (1978) (Figure 1b and e). Birch (1978) suggested that leucite–bearing basalts may extend south from Pine Lodge toward Euroa and into the Newer Volcanic Province. The observation by Paul et al. (2005) of 5% leucite in basalt occurrences to the south of Pine Lodge–Cosgrove at Seven Creeks East, to the south of Euroa, extended the known occurrences of leucite in Eastern Australian basaltic rocks even further south, well into the Newer Volcanic Province of Victoria (Figure 1b and e). Significantly, the area around Euroa includes a number of volcanic outcrops that display mixed chemistry, indicating links in magmatic origin to the eastern edge of the Newer Volcanic Province (Figure 1b and e; Heath et al., 2018, 2020; Paul et al., 2005).

Although leucite is known to be present in other volcanic rocks in Eastern Australia, such as the McLean volcanic field in far–north Queensland, in lamprophyres near Wollongong, and in a ”monchiquitic basalt” at Harden, these outcrops vary drastically in age, chemistry, and interpreted geodynamic setting (Figure 1a–b). Harvey and Joplin (1940) also interpreted the Harden basalts to be lamprophyric, specifically leucite monchiquites. Chemically, when compared to the EAPS, this corresponds to lower SiO_2 (39–41 wt%), much higher Al_2O_3 (10–15 wt%) and Na_2O (3–5 wt%), and significantly lower K_2O (1–2 wt%). The Hoskings Peak outcrop within the McLean field is yet to be studied in its entirety, largely due to its limited exposure and geographically isolated location. Given the age and genetic association of other outcrops to the south with the Cosgrove hotspot track (i.e. Buckland (Figure 1a); Shea and Foley, 2019), it is possible that the McLean field is an additional expression of volcanism synonymous with the EAPS (Barron et al., 1996).

Methods

A comprehensive description of methods can be found in the supplement with an abridged version presented here. Aliquots of each sample were inspected for alteration features and the most representative portions were disaggregated and powdered. Aliquots were taken from areas free from iddingsite, xenocrysts, and xenoliths. Powders were produced by cutting and drying a small block close to the location of the thin section block, then partially disaggregated using a rock crusher. Rock fragments from the disaggregated samples were collected and only fragments in the size range of 5–15 mm were used to ensure a clean powder. Fragments were powdered in a TEMA agate puck mill for between 2 and 10 minutes. Agate mills were cleaned between samples by milling silica sand for around 5 minutes, rinsed with tap–water, then washed with milli–Q water, and cleaned with ethanol.

X–Ray Fluoresence Spectroscopy & Loss on Ignition

Fused disc XRF was undertaken using a lithum metaborate: lithium tetraborate (LiM:LiT) flux in a 12:22 ratio. Sample powders were weighed into clean Pt crucibles in 1 g aliquots recorded to four decimal places and combined with 10 g of pre–dried LiT:LiM flux (sample:flux=1:10). Homogenised sample-flux mixtures were then melted at 1050 °C for 20 minutes in a rocking furnace at the Macquarie GeoAnalytical (MQGA) Facility within the School of Natural Sciences, Macquarie University. NH_4I tablets, reacted for 3 minutes, were used as a releasing agent to increase surface tension before the mixture was poured into a Pt mould and cooled under air to room temperature. Analyses were carried out using a PANalytical Axios 1kW WDXRF, with the U.S.G.S. Hawaiian Basalt BHVO-2, BCR-2, and OKUM reference materials, along with an in-house standard PB-SS (alkaline basalt from Prospect, NSW) used to monitor accuracy and precision. Multiple analyses of BHVO-2 or BCR-2 from each measurement batch returned values ranging from 0.05–8% from the GeoReM preferred values (Jochum et al., 2005), with only Al_2O_3 (1.19%) and P_2O_5 (8.01%) deviating by more than 1% for BHVO-2. Uncertainties on BHVO-2 measurements were also calculated with only P_2O_5 and Cr_2O_3 exceeding 1% standard error (2.23 and 2.33%, respectively). Values for all other reference materials showed similar accuracy and precision to those reported above for BHVO-2. Loss on Ignition (LOI) was undertaken by weighing ∼1.4 g of sample (recorded to four decimal places) into pre–dried alumina crucibles. Samples were then fired in an 1100 °C furnace overnight (minimum 10 hours), and reweighed with absolute loss determined numerically before conversion to percent loss.

Trace Element Geochemistry

Trace elements were determined using solution ICP–MS at MQGA. Digestions were undertaken on a sub–set of sample powders selected after XRF analyses were complete to reduce the total number of digestions and limit replicates on sub–samples from the same localities. A 100mg aliquot of sample powder (recorded to four decimal places) was added to clean savillex Teflon 15mL beakers and digested via sequential fluxing under concentrated HF (Merck, Suprapur grade), concentrated HNO_3 (Merck, Analar grade), perchloric ($HClO_4$; Merck Suprapur), and HCl acids. Care was taken to ensure residual fluorides and chlorides from acids were not present following each step and additional method steps were undertaken to digest spinels present in the sample *see Supplement for method steps*. Final sample solutions were diluted to 100mL with 2% HNO_3 and 0.25% HF in a 1:1000 sample solution. A 5mL aliquot of the diluted sample solution was separated and prepared for ICP–MS analysis with the addition of 0.02mL of a multi–element internal standard spike containing ^{6}Li, As, Rh, In, Tm and Bi to correct for instrument drift. Spiked samples were run on an Agilent 7700cs quadrupole ICP–MS for the masses of ^{7}Li, ^{9}Be, ^{45}Sc, ^{47}Ti, ^{51}V, ^{53}Cr, ^{55}Mn, ^{59}Co, ^{60}Ni, ^{65}Cu, ^{66}Zn, ^{71}Ga, ^{85}Rb, ^{88}Sr, ^{89}Y, ^{91}Zr, ^{93}Nb, ^{95}Mo, ^{114}Cd,^{121}Sb ^{133}Cs, ^{137}Ba, ^{139}La, ^{140}Ce, ^{141}Pr, ^{146}Nd, ^{147}Sm, ^{153}Eu, ^{157}Gd, ^{159}Tb, ^{160}Gd, ^{163}Dy, ^{165}Ho, ^{167}Er, ^{169}Tm, ^{173}Yb, ^{175}Lu, ^{178}Hf, ^{181}Ta, ^{184}W, ^{208}Pb, ^{232}Th, ^{238}U. Method and acid blanks were carried out at the beginning and end of each run, as well as after 10 analyses in each run. Internationally recognised standards BCR-2, BHVO-2, and BIR-1 in 1:1000, 1:2000 and 1:5000 spiked solutions were analysed throughout the run to monitor accuracy

and precision. The calibration standard used was BCR-2 and additional analyses of BCR-2 were used as a secondary standard. Measurements of BHVO-2 fell within 1.03–30.66% of the GeoReM preferred values, with the majority of elements within 10% of the reference value. Only Li, Be, Cr, Cu and Cd were above 15% (17.18, 30.66, 26.28, 28.23 and 65.38%). However all of these elements were within 15% of either BCR-2 or BIR-1, both of which are closer to the average concentration of the unknown samples analysed. All measurements of BHVO-2 fell within a 3% standard error for all elements except Mo, which had a standard error of 8.06%.

Volatile Element Analysis

Carbon, Hydrogen, Nitrogen, and Sulfur were determined using a Elementar vario EL cube elemental analyser (Elementar, Langenselbold, Germany) at MQGA following the methods of Alard et al. (2022) and Ananuer and Alard (in prep.). Whole rock sample powders were weighed into pre-formed Sn-foils in either 50 or 100mg aliquots added to a flux of WO_3 (tungsten oxide, Elementar Langenselbold, Germany) in a ratio of 1:1.1 (i.e. sample / $WO_3 \approx 1.1$) prior to drying in a vacuum oven (ca. 0.1 bar) for around 24 hours at 105 °C flushed with Ar-gas. Sample filled Sn-foil packets were then compressed by hand into pellets. Pellets were weighed pre- and post-packing to ensure no ruptures or loss of sample from packets. Sample pellets were then loaded into the analyser and ignited in an oxygen-He gas atmosphere furnace at a temperature of 1150 °C. Prior to ignition the system was purged with He to wash out atmospheric nitrogen. A blank was run before each sample to reduce possible contamination from previous sample(s). Ignition under O_2 atmosphere causes the complete decomposition of the sample powder releasing H_2O and CO_2 as well as NO_x and SO_x which are reduced through reaction with Cu-chips in the reduction chamber to NO_2 and SO_2 respectively. Halogens are removed prior to reduction in order to prevent reaction with the Cu-chips by a silver wool trap placed at the top of the combustion chamber.

Volatile gases emitted after ignition were isolated by gas chromatographic separation and measured using a thermal conductivity detector (TCD), or infrared detector (IR; S-only). The TCD has an intrinsic LLD of roughly 40 ppm for all elements, while IR has a theoretical LLD ca. 1 ppm. However, long-term (≈5 years) blank measurements indicate that LLD is ca. 100 ppm for N, 32 ppm for C, 150 ppm for H, and 40 and 5 ppm for S by TCD and IR, respectively (Alard et al., 2022). Measurements obtained on 7 procedural blanks (Sn foils + 100 mg of WO_3) obtained during this study are in-line with the long-term performances of the elemental analyser. Precision and accuracy were assessed by repeated analyses of the Geo-Reference Materials BCR-2, BE-N, DR-N, OKUM, PM-S, and WS-E. Measured values were within 15% of the reported value for all elements; procedural blanks and standard analyses are provided in the supplementary materials (Supplementary Table 1). A major limitation of this technique is the lack of reliable reference values for the standard reference materials, especially for the elements N and C, but also H; this is remedied in part by the work of Ananuer and Alard (in prep.).

Results

Petrography

Geographically the extent of the samples makes it most logical to discuss the petrography in the context of each sample relative to those within the same geographic region. The clusters are defined as *Tindarey* (north; Figure 1c), *Tullibigeal* (central; Figure 1d) and *Griffith and Shepparton* (south; Figure 1d–e).

The term ”xenocryst” is used here to describe an olivine or clinopyroxene for which a primary magmatic origin is unlikely. The primary first order characteristic we use to demarcate xenocrystic olivine from phenocrystic olivine is the strong size contrast between these grains and the overall texture of the rock, and the strongly anhedral form of xenocrysts. This is due to the time that is required for an olivine to increase in size by roughly an order of magnitude (i.e. from 100 μm to ∼1 mm). Where size is not a clear indicator additional textures were used to highlight potentially xenocrystic grains. These textures include undulose extinction; any evidence of resorption or disequilibrium

Table 1. Petrography summary with estimated proportions: ⊗ = Major (>20%); • = Minor (<20%); ○ = rare (<5%); † = Analcime dominant; All samples with groundmass Phl may be termed 'madupitic'.

			Phenocrysts (>100 µm)							Groundmass (<100 µm)							Other		
#	Locality	Rock Type	Lct	Phl	Ol	Cpx	Sa	Rct	Ox	Lct	Phl	Ol	Cpx	Sa	Rct	Ox	MC[a]	Melt	Notes:
09[s]	Byrock	Leucite-diopside-phlogopite lamproite	⊗	⊗[b]	○	⊗	○	•		⊗		•	⊗	○	○	⊗	L[c]	•	Highly heterogeneous; veins; rare pegmatite nodules; Carb. glass present
08[t]	El Capitan	Leucite-phlogopite-olivine lamproite			⊗	•				⊗	⊗			•	•	⊗	LC[c]	○	Carbonated (Carb.) glass present
15[u]	Koorangie	Diopside-leucite-olivine lamproite	○		⊗	⊗				⊗	•[d]		•			•	C[c]		
07[v]	Weebar Hill	Phlogopite-olivine-diopside lamproite	•	⊗	⊗	⊗			•	⊗			⊗		○	•	C[c]	•	Primary groundmass
										⊗	⊗[e]		•	•					Second groundmass in lenses/ pockets
14[w]	Wallaroy Hill	Diopside-olivine-leucite lamproite	•	⊗[b]	⊗	⊗				⊗	•		⊗	○		⊗	LC	○	Carbonated glass present
22[w]	Lake Cargelligo	Diopside-olivine-leucite lamproite	○	•	⊗	⊗		•	○	⊗	⊗	•	⊗			•	C[c]		
02[w]	Lake Cargelligo	Olivine-diopside-leucite lamproite	○		⊗	⊗			•	⊗	⊗	○	•			•	C	•	
03[w]	Lake Cargelligo	Olivine-leucite-phlogopite lamproite	⊗	⊗	⊗	•		•	○	⊗	•	○	⊗	○	○	•	C[c]	○	Carbonated glass present
01[w]	Lake Cargelligo	Olivine-diopside-leucite lamproite	⊗	⊗	⊗	⊗	•	•	•	⊗	⊗	•	⊗	•	•	•	C[c]	•	Occasional melt veins; Carbonated glass present
16[w]	Tullibigeal	Olivine-phlogopite-diopside-leucite lamproite		⊗[b]	⊗[f]	•			•	⊗	○	•	⊗	○	○	•	C[c]	○	Carbonated glass present
23[w]	Tullibigeal	Olivine-leucite-diopside lamproite			⊗	⊗	•		•	⊗	•		⊗			•	LC[c]	○	
04[v]	Tullibigeal	Olivine-diopside-leucite lamproite	•	•	⊗	⊗				⊗	•	•	⊗			•	C		Primary groundmass
										⊗	•	•	⊗	•		•			Second groundmass in lenses/ pockets
25[w]	Bygalorie	Olivine-leucite-diopside lamproite	○	○	⊗	•			•	⊗	•	•	•			•	C	•	Melt veins present
26[w]	Bygalorie	Olivine-phlogopite-leucite Lamproite	○		⊗	•			•	⊗	⊗	•	•			⊗	C	•	Carbonated glass present
05[w]	Bygalorie	Leucite-olivine lamproite	⊗		⊗[e]	•			•	⊗	⊗		•			•	C	•	Carbonated glass present
19[x]	Begargo Hill	Olivine-leucite-diopside lamproite	•	⊗[b]	⊗	⊗			○	⊗	•	•	⊗	•		•	LC[c]	•	Melt surrounding xenolith crystallizing Phl and Sa; Carb. glass present
17[w]	Flagstaff Hill	Leucite-diopside-olivine-phlogopite lamproite	• †		⊗[f]	⊗				⊗	•		⊗			•	LC[c]	•	Carbonated glass present
18[y]	Griffith	Analcimite [1]	†		•[g]	⊗			•			•	⊗			⊗	C[g]		Heavily altered; Major element chemistry affected
20[z]	Pine Lodge	Olivine leucitite [2]	†		⊗[g]	•			•		•		⊗			⊗	C[g]		Heavily altered; Major element chemistry affected
21[y]	Violet Town	Alkali basalt [3]	†		⊗[g]	•	⊗[h]		⊗			•[f]				•	C[c,g]	•	Heavily altered; Major element chemistry affected

[a]: MC = Mantle Cargo; L = xenolith; C = xenocryst. Xenocryst criteria: olivine or pyroxene >500 µm, higher interference colours, undulous extinction, evidence of transport or deformation. [b]: Poikolitic phlogopite with apatite, carbonate, leucite, or clinopyroxene; madupitic texture. [c]: Occasionally altered or melt mediated to some degree, including skeletal grains and embayments. [d]: Occurring as anhedral inclusion-free grains with no relation to olivine. [e]: Phl mantling Olivine; Potentially incongruent melt reaction. [f]: Iddingsite present but not dominant. [g]: Iddingsite dominant; rare remnant olivine cores. [h]: Clear sanidine twins present with occasional tartan twins suggesting microcline. **Textures:** [s]: Porphyritic; occasional megacrystic grain size. [t]: Porphyritic; inequigranular to aphanitic groundmass. [u]: Equigranular groundmass; sparse phenocrysts. [v]: Porphyritic; two inequigranular groundmasses. [w]: Porphyritic; inequigranular groundmass. [x]: Porphyritic; multimodal phenocrysts; inequigranular groundmass. [y]: Altered porphyritic; inequigranular groundmass. [z]: Altered porphyritic; aphanitic groundmass. **Key:** Cpx = Clinopyroxene; Lct = Leucite; Melt = Glass *(Silicate or Carbonated)*; Ol = Olivine; Ox = Oxide (Fe–Ti); Phl = Phlogopite; Rct = Richterite; Sa = Sanidine. **References:** [1]: Barron et al. (1996), after Cundari (1973); [2]: Birch (1978); [3]: Paul et al. (2005).

such as melt infiltration *(or reaction i.e. incongruent phlogopite production)*; those that show signs of turbid/violent movement/transport such as cracking, fracturing and rounding of euhedral faces. Another key feature of phenocrystic and groundmass olivine is the strong affinity to host opaque mineral inclusions, whereas xenocrystic olivine in most of the samples are often inclusion-free. Xenocrystic pyroxene is more obvious with anhedral forms and cracks or fractures, while magmatic clinopyroxene exhibits a clearly euhedral form absent of any evidence of transport. Small xenoliths that exhibit relatively depleted mineralogy between dunitic and harzburgitic are observed in both the Tindarey and Tullibigeal areas (Table 1; Figure 2c).

In the interest of simplifying the assemblage across localities and limiting unnecessary repetition we first note that all samples in this investigation display magmatic olivine (as olivine or the alteration mineral iddingsite), and opaque oxide minerals belonging primarily to the hematite and rutile groups (Figure 2). Additionally with the exception of the southern exposures, leucite and phlogopite mica of a magmatic origin are present in all samples as is clinopyroxene. Sulfur bearing minerals, as sulphides, phosphates (as apatite), and carbonates are also present in all sample sites, excluding the southern grouping. Sulphides are less abundant and smaller than phosphates and carbonates which are common intergrowths in phlogopite. In addition to crystalline carbonates that are present in phlogopite plates (usually in the order of 10 μm), carbonated melts are preserved as glasses in samples along the entire northern and central sections of the lamproite chain (Figure 2c–d). Silicate glasses are also present in some samples, and are most common in the central Tullibigeal group. The comparative mineralogy and the corresponding rock name for each sample site is given in Table 1.

Tindarey (Northern sample sites): Byrock and El Capitan are the two most northern exposures and are located north of the town of Cobar (Figure 1b–c and 2a–b). These two localities are extremely heteromorphic despite exhibiting similar whole rock chemistry *(Heteromorphism: chemically similar but mineralogically distinct)*. Byrock presents with a strong porphyritic texture and megacrystic phlogopite plates exceeding 6mm, which are heavily intergrown but continuous crystals (Figure 2a). These phlogopites are also clearly titanian from the strong reds in cross-polarised light which is common feature among lamproites (Mitchell, 2020, 2021). Olivine is scarce at Byrock as a phenocryst, and this outcrop is the only exposure to display (rare) phenocrysts of richterite in the northern area (Table 1). Leucite and clinopyroxene are abundant within sections from Byrock which is in strong contrast to El Capitan where leucite is absent from the phenocrysts and clinopyroxene is a minor phenocrystic phase (Figure 2a–b). El Capitan hosts an aphanitic groundmass with abundant olivine phenocrysts, where the groundmass hosts the majority of the potassic minerals (Lct > Phl > Rct > Sa). Sanidine is present in both localities as groundmass but only rarely as phenocrysts in Byrock. The crystallisation sequence for Byrock suggests phlogopite is the liquidus phase, either co-crystallising with or followed by olivine, then clinopyroxene with leucite, sanidine, and richterite being co-crystallising phases. The lack of clear phlogopite groundmass further suggests that the available water in the magma was locked up within the abundant phlogopite phenocrysts during initial crystallisation. Thus, resulting in a lack of available water to allow the formation of further richterite, and facilitating the growth of large leucite phenocrysts as the magma ascended. The texture of El Capitan on the other hand, suggests a more rapid ascent and extrusion with only olivine and minor clinopyroxene forming phenocrysts with the remaining magma freezing quickly at the surface (Figure 2a–b).

Tullibegeal (central sample sites): The vast majority of samples in this study come from the central area with 15 sample sites (Table 1; Figure 1c–d). All sites contain olivine and clinopyroxene phenocrysts, while most also contain phenocrystic leucite. Only two sites contain phenocrystic sanidine (Figure 2d), while nine contain phlogopite as a phenocrystic phase (Table 1). Phlogopite phenocrysts are more diverse in this group with the abundance and style differing between a rare (sample 25) through major (sample 03) phase, and from clearly defined euhedral plates (sample 03) through to poikilitic plates (sample 14). Minor alteration of olivine to iddingsite was observed at two sites in the central area, and all central samples host xenocrystic olivine. Leucite, phlogopite and clinopyroxene are present in the groundmass of every central outcrop, while olivine is present in most sites. Sanidine is uncommon as a phenocrystic phase (Table 1), usually occurring as

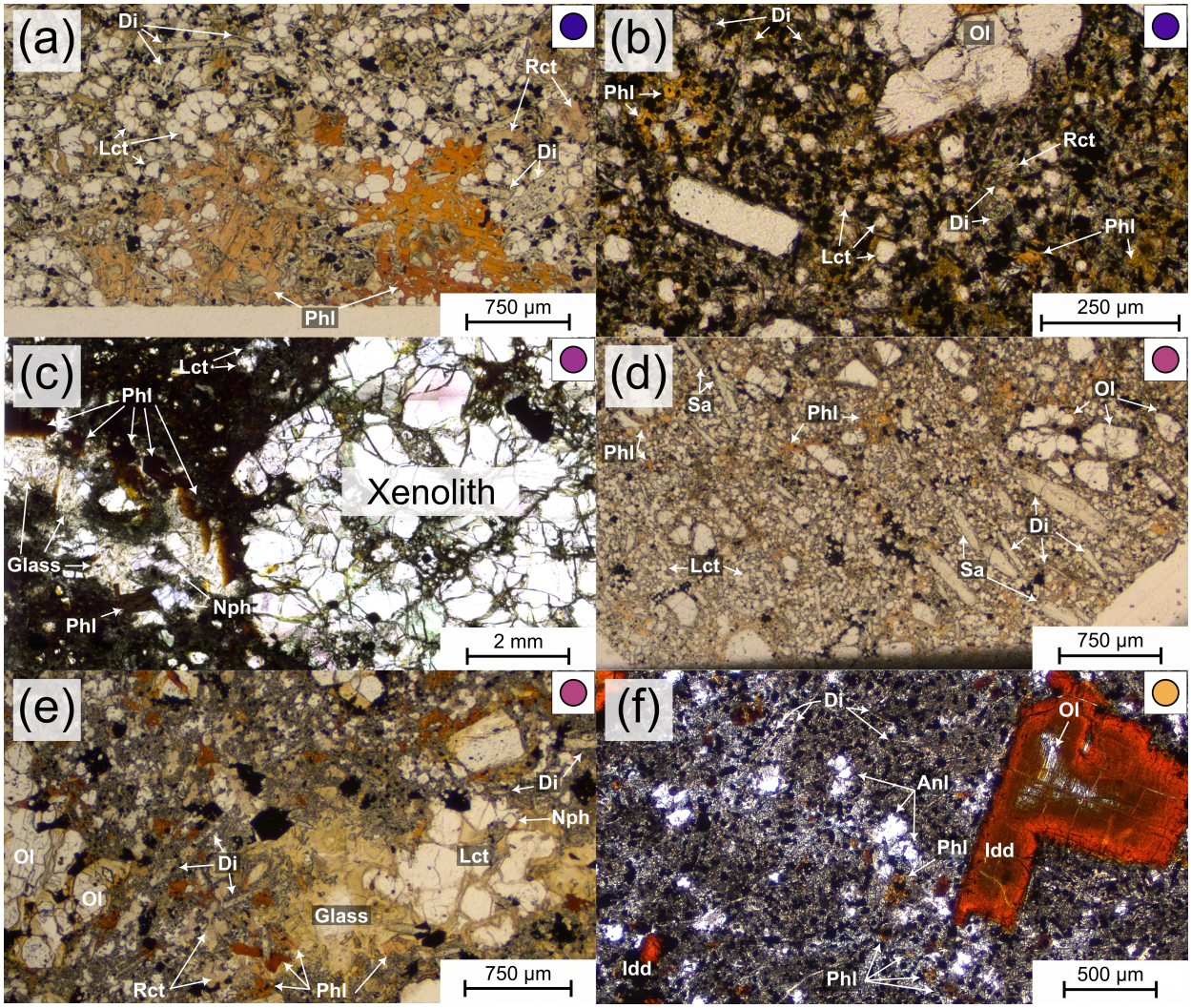

Fig. 2. Summary of petrographic textures and phases of the EAPS. Selected samples arranged north to south starting with (a) 0901 – Byrock, (b) 0801 – El Capitan, (c) 1402x4 – Wallaroy Hill, (d) 2202 – Lake Cargelligo, (e) 0102 – Lake Cargelligo, and (f) 2001 – Pine Lodge (Cosgrove). Coloured circles in top right of each panel correspond to the colour scale used for the EAPS samples in all geochemical plots; see Figure 3. Key features include porphyritic texture of (a) compared to a more equigranular texture in (b); (a) including small ($< 20\ \mu$m) apatite and carbonate grains entrained in poikilitic phlogopite. (d) shows prevalence of sanidine in some samples, also contrasting the porphyritic texture of (a). (c) and (e) show examples of where nepheline is present, highlighting the restricted formation in melt pools (glass). (f) displays highly altered texture of Pine Lodge (Cosgrove), with most olivine converted to iddingsite and only rare olivine cores preserved. Diopside and phlogopite are also present at Pine Lodge (f); diopside appears fluid mediated with spindly, wavy forms and all leucite at least partly transformed to analcime. Multiple labels for the same mineral present in (a) – (f) highlight varying forms, textures, and sizes within the sample. All images are plane polarised light on thin sections ($\approx$30 μm) except (c) which is a thick section ($> 100\ \mu$m). Large anhedral olivine are xenocrysts e.g. (b), (d), and (e). Mineral abbreviations used are the IMA-CNMNC approved symbols (Miyawaki et al., 2021), taken from the compilation of (Warr, 2021). Anl = Analcime; Di = Diopside; Idd = Iddingsite; Lct = Leucite; Nph = Nepheline; Ol = Olivine; Phl = Phlogopite; Rct = Richterite; Sa = Sanidine.

euhedral to subhedral crystals (Figure 2d), but occurs as a groundmass phase in about half of the sites while (K–)richterite occurs only in four samples (samples 07, 03, 05, and 16; Table 1). Richterite is potentially present as a minor or trace phase in additional localities given the heteromorphic nature of the samples and that it forms in this grouping primarily as small (in the order of 20μm), anhedral, and heavily overgrown groundmass crystals. Nepheline was observed in four sub-samples of this group (0102, 0103, 1402x4, and 1903), but was not observed in the remaining samples from these sites. In each of these samples, nepheline occurs exclusively within veins or glassy melt pools (Figure 2c and e) which we interpret to be secondary or late-stage crystallisation. This is partially reinforced by the proximity of these melt features to xenocrysts and xenoliths suggesting the crystallisation of nepheline may represent a reaction product between the final melt and mantle cargo (Figure 2c). These observations are addressed further in the classification section of the discussion. Crystallisation sequence is

interpreted to vary between sites, but, in general olivine appears to be the first phase to form, with either clinopyroxene or phlogopite next likely. Leucite is always euhedral but is certainly one of the later forming phases given it is usually less abundant than the other phenocrystic phases, while dominating the groundmass. Groundmass leucite is commonly completely surrounded by euhedral clinopyroxenes, usually 10μm or less wide, that define the boundary between crystals.

Griffith and Shepparton (Southern sample sites): The southern sample sites are distinct from all other samples described here and necessitate caution in their interpretation (Table 1; Figure 2e). Characterised by olivine and clinopyroxene phenocrysts across all sites, these samples all display clear evidence of alteration by fluids suggesting the original texture and petrological character of the rocks have been lost (Figure 2e). Oxide minerals are present as both groundmass and phenocrysts, and the groundmass for all sites is dominated by pseudoleucite or analcime. Griffith (sample 18; Table 1) was previously reported to host primary analcime (Cundari, 1973). However, we found no textural evidence of this being the case and instead the broader fabric of our samples appear heavily fluid mediated (Table 1). Pine Lodge (sample 20; Figure 2e), which is commonly known as Cosgrove, exhibits minor polysynthetic twinning characteristic of leucite but can also be preserved in pseudoleucite that has not undergone full transformation to analcime (Figure 2e). Violet Town (sample 21; Table 1) largely matches the petrology and mineralogy of Pine Lodge by exhibiting both altered olivine (iddingsite; Figure 2e), minor pyroxene, and altered leucite, however Violet Town also includes nepheline. Both samples 20 and 21 include feldspar group minerals, which in the case of Pine Lodge (sample 20) is sanidine but ranges between sanidine and anorthoclase at Violet Town. All sites in this group exhibit severe alteration of olivine to iddingsite, however occasional cores of olivine are preserved (Figure 2e). The extent of alteration is also visible in the whole rock chemistry, that will be discussed further below.

Major and Minor Element Geochemistry

The samples presented here are silica-undersaturated and for the most part enriched in potassium (Table 2; Lanati and Shea, 2025). All but one plot within the foidite field of the TAS diagram and contain SiO_2 40–45 wt% (Figure 3a and c), with the vast majority of samples containing >4 wt% K_2O, placing them within the leucititic and potassic to ultrapotassic fields (Figure 3b–c). Coupled with all samples having MgO > 3wt% and most displaying $K_2O/Na_2O > 2$ the suite (K_2O = 1.18–7.37 wt%; MgO = 6.97–16.98 wt%; K_2O/Na_2O = 0.34–7.83), meets the ultrapotassic screens used by Foley et al. (1987) ($K_2O > 3$ wt%; MgO > 3 wt%; $K_2O/Na_2O > 2$) for 38 of 49 analyses. On a molar basis they have K/Na of 0.22–5.15, are on average moderately peralkaline (Av: 1.01) and trend toward perpotassic (Table 2; [(K+Na)/Al = 0.54–1.28] and [K/Al = 0.13–0.93]; Supplementary Figure 1). When plotted against MgO, which along with K_2O is the only element to vary significantly, all other elements show minor variations but represent some of the most enriched compositions for TiO_2, P_2O_5, Cr, Ni, and Cu globally when compared with other basaltic melts (Figure 4b and e, and 5d–f). The EAPS samples also exhibit lower Al_2O_3 and FeO_T than the primitive basalts of the EAVP (*plotted as EAVP Prim*; Shea et al., 2022), while CaO, MnO, and Na_2O overlap with the basalts (Figure 4f and 5b–c). EAPS samples can be geographically discriminated in terms of K_2O versus Na_2O with more potassic compositions in the northern volcanoes at Byrock and El Capitan than in the central exposures centred around Tullibigeal and Lake Cargelligo (Figure 3b). The southern exposures have consistently lower K_2O/Na_2O at $\leq$0.5. In order to compare the new analyses with primitive melts globally, published data was filtered for Mg number $\geq$ 55, $FeO_T \geq 6$ wt%, MgO $\geq$ 4 wt%, and SiO_2 <60 wt% to remove fractionated and evolved melts based on filters similar to Prelević et al. (2008b) and Shea et al. (2022). A complete summary of the filtering process and datasets is provided in the supplement. When compared with leucitites from the Sierra Nevada volcanics (Farmer et al., 2002) and the Roman province (compiled from GEOROC database (**https://georoc.eu/**; version 2023-12-01) the EAPS lavas are enriched in TiO_2 and FeO_T, while SiO_2 is generally lower (Figure 4a, b, and d). In Figures 3, 4, and 5 the EAPS lavas are also compared to lamproites using the compilations from Casalini et al. (2022) and Sarkar et al. (2025) indicating a considerable overlap with anorogenic lamproites in most chemical spaces. In

Table 2. Major element analyses of EAPS samples arranged N–S. Longitude and Latitude in decimal degrees; Elevation in meters; Age in Ma $\pm 2\sigma$. All other values in wt% unless stated otherwise except N, C, H, and S (all ppm).

ID	Location	Province	Latitude	Longitude	Elev.	Age	SiO_2	TiO_2	Al_2O_3	Fe_2O_3t	MnO	MgO	CaO	Na_2O	K_2O	P_2O_5	LOI	Sum
0901.1	Byrock	Tindarey	-30.709733	146.316817	260	17.1 ± 0.2†	43.74	4.84	9.20	10.63	0.12	10.79	7.97	0.99	6.94	1.01	2.87	99.10
0901.2	Byrock	Tindarey	-30.709733	146.316817	260	17.1 ± 0.2†	43.36	5.02	8.56	10.72	0.12	11.02	8.07	1.03	6.39	0.98	3.14	98.41
0901a.1	Byrock	Tindarey	-30.709733	146.316817	260	17.1 ± 0.2†	45.01	5.33	8.55	11.73	0.14	8.31	8.44	1.10	7.37	0.65	2.93	99.56
0901a.2	Byrock	Tindarey	-30.709733	146.316817	260	17.1 ± 0.2†	43.61	5.06	8.36	11.36	0.13	10.60	8.44	0.80	6.23	0.92	3.44	98.96
0801	El Capitan	Tindarey	-31.184200	146.141217	278	17.9 ± 0.3†	41.21	4.99	7.30	11.21	0.15	13.02	8.91	0.71	5.35	1.22	4.44	98.50
0802	El Capitan	Tindarey	-31.184700	146.141533	278	17.9 ± 0.3†	41.08	5.28	7.39	11.13	0.13	12.94	9.32	0.79	6.17	1.33	3.36	98.91
0803	El Capitan	Tindarey	-31.184950	146.141333	277	17.9 ± 0.3†	40.66	4.99	7.25	10.92	0.14	12.95	8.96	0.87	5.66	1.44	4.27	98.10
1501	Koorangie	Tullibigeal	-32.973633	146.941717	192		42.99	4.09	8.66	11.41	0.16	13.03	9.07	1.76	3.85	1.14	2.99	99.14
0701	Weebar Hill	Tullibigeal	-33.168317	147.033033	189	17.9 ± 0.4	42.75	4.59	8.71	11.96	0.16	11.69	8.63	2.85	4.57	1.10	2.15	99.15
1402	Wallaroy Hill	Tullibigeal	-33.199467	147.029217	307		44.53	3.93	9.22	11.11	0.14	10.11	9.24	2.85	1.96	1.21	4.82	99.11
1403	Wallaroy Hill	Tullibigeal	-33.200183	147.011567	199		43.80	4.16	8.03	11.34	0.15	13.93	8.14	1.94	5.16	1.23	1.25	99.12
1401	Wallaroy Hill	Tullibigeal	-33.201150	147.020667	215		45.45	3.99	8.33	10.50	0.14	12.86	7.23	1.91	6.00	1.03	1.49	98.92
2201	Lake Cargelligo	Tullibigeal	-33.283700	146.305167	181	11.6 ± 0.2	43.25	3.67	7.53	9.97	0.14	13.50	9.15	0.78	5.24	0.68	3.83	97.74
2202	Lake Cargelligo	Tullibigeal	-33.283800	146.306150	173	11.6 ± 0.2	43.52	3.68	7.66	9.92	0.13	13.30	8.84	0.86	5.23	0.93	4.48	98.54
0203	Lake Cargelligo	Tullibigeal	-33.285521	146.349984	193	13.0 ± 0.2	43.03	3.96	9.12	11.79	0.16	12.51	9.73	3.51	4.37	1.16	1.92	101.26
0202	Lake Cargelligo	Tullibigeal	-33.285701	146.349864	193	13.0 ± 0.2	43.21	3.94	9.02	11.76	0.16	12.67	9.53	2.01	4.27	1.16	1.82	99.55
0201	Lake Cargelligo	Tullibigeal	-33.285737	146.349778	193	13.0 ± 0.2	43.08	3.95	9.12	11.70	0.16	12.34	9.62	1.94	4.52	1.13	2.28	99.84
0302	Lake Cargelligo	Tullibigeal	-33.286946	146.344807	208	13.0 ± 0.2	43.55	4.46	8.59	11.24	0.15	12.82	8.16	1.97	5.33	1.27	1.52	99.06
0301	Lake Cargelligo	Tullibigeal	-33.286998	146.344463	212	13.0 ± 0.2	44.36	4.05	8.68	10.98	0.14	12.62	8.47	1.44	6.15	1.42	1.55	99.86
0105	Lake Cargelligo	Tullibigeal	-33.288800	146.349756	182	13.0 ± 0.2	42.58	4.05	9.13	11.78	0.16	12.61	9.73	2.24	4.13	1.16	1.61	99.18
0101	Lake Cargelligo	Tullibigeal	-33.289139	146.369331	180	13.0 ± 0.2	43.29	3.95	9.15	11.77	0.16	12.65	9.47	2.09	4.16	1.21	1.97	99.87
0102	Lake Cargelligo	Tullibigeal	-33.289246	146.369180	181	13.0 ± 0.2	43.32	4.00	9.12	11.71	0.16	12.37	9.56	1.97	4.32	1.19	2.24	99.96
0103	Lake Cargelligo	Tullibigeal	-33.289261	146.368525	183	13.0 ± 0.2	42.68	4.04	9.15	11.76	0.16	12.79	9.53	2.23	4.14	1.19	1.63	99.30
0104	Lake Cargelligo	Tullibigeal	-33.289702	146.368457	182	13.0 ± 0.2	43.00	4.06	9.28	11.82	0.16	12.42	9.62	2.33	4.20	1.17	1.30	99.36
1602	Tullibigeal	Tullibigeal	-33.378767	146.769000	322	12.8 ± 0.3	43.36	3.85	7.79	10.73	0.15	12.73	8.62	1.51	6.12	1.32	1.23	97.39
1604	Tullibigeal	Tullibigeal	-33.380617	146.774750	304	12.8 ± 0.3	44.00	4.06	8.08	10.80	0.14	12.65	8.77	1.62	6.21	1.60	1.13	99.05
1603	Tullibigeal	Tullibigeal	-33.381383	146.766433	295	12.8 ± 0.3	44.60	4.38	8.19	10.83	0.13	10.06	7.94	1.79	6.72	1.58	2.35	98.57
1601	Tullibigeal	Tullibigeal	-33.382433	146.766200	292	12.8 ± 0.3	43.76	3.98	7.96	10.81	0.15	12.55	9.13	1.57	5.95	1.47	1.97	99.29
2301	Tullibigeal	Tullibigeal	-33.440783	146.685150	272	10.4 ± 0.3	43.92	3.28	8.32	10.85	0.15	14.84	8.43	1.84	4.45	1.22	1.98	99.28
0402	Tullibigeal	Tullibigeal	-33.442580	146.672985	266	10.4 ± 0.3	45.65	3.64	8.39	10.46	0.14	12.09	7.86	1.92	6.06	1.62	1.79	99.62
0401	Tullibigeal	Tullibigeal	-33.442671	146.673082	267	10.4 ± 0.3	45.80	3.62	8.28	10.45	0.15	12.87	8.04	1.49	5.56	1.33	2.18	99.77
2501	Bygalorie	Tullibigeal	-33.501317	146.737417	392	15.1 ± 0.3†	44.17	4.27	9.24	11.45	0.15	11.72	8.50	2.41	4.97	1.30	1.28	99.46
2502	Bygalorie	Tullibigeal	-33.502050	146.737417	385	15.1 ± 0.3†	44.07	4.27	9.08	11.51	0.15	11.65	8.59	2.40	5.24	1.34	1.06	99.36
2601	Bygalorie	Tullibigeal	-33.502117	146.745383	365	15.1 ± 0.3†	43.07	4.47	8.27	11.89	0.16	10.81	9.65	2.38	5.78	1.24	1.73	99.45
0502	Bygalorie	Tullibigeal	-33.514867	146.756734	413	12.6 ± 0.3	43.39	4.35	8.32	11.60	0.15	11.75	8.25	2.06	6.45	1.72	1.23	99.26
0501	Bygalorie	Tullibigeal	-33.515155	146.756507	391	12.6 ± 0.3	44.56	4.23	8.53	11.19	0.14	11.33	7.84	2.10	6.90	1.80	1.00	99.63
0503	Bygalorie	Tullibigeal	-33.515203	146.757853	371	12.6 ± 0.3	44.32	3.91	8.63	11.15	0.15	11.42	9.26	2.20	6.04	1.37	1.62	100.06
1904	Begargo Hill	Tullibigeal	-33.526250	146.362300	215	15.5 ± 0.5†	43.46	3.93	8.38	11.05	0.15	12.97	9.39	1.92	4.97	1.42	1.42	99.05
1903	Begargo Hill	Tullibigeal	-33.526283	146.363250	217	15.5 ± 0.5†	43.12	4.04	8.55	11.39	0.16	13.82	8.90	2.12	4.79	1.44	0.58	98.89
1902	Begargo Hill	Tullibigeal	-33.528067	146.366233	183	15.5 ± 0.5†	44.28	3.89	8.96	10.97	0.15	12.28	8.90	2.26	5.35	1.19	0.91	99.13
1701	Flagstaff Hill	Tullibigeal	-33.795067	146.085167	306	15.3 ± 0.4†	44.31	3.30	8.46	10.53	0.15	14.55	7.90	1.92	4.87	1.30	1.57	98.87
1702	Flagstaff Hill	Tullibigeal	-33.795383	146.084600	307	15.3 ± 0.4†	44.30	3.28	8.38	10.64	0.14	14.65	7.89	1.89	5.06	1.29	1.46	98.98
1704	Flagstaff Hill	Tullibigeal	-33.795717	146.084367	311	15.3 ± 0.4†	44.13	3.44	8.49	10.71	0.15	14.40	7.95	1.95	4.96	1.32	1.56	99.05
1703	Flagstaff Hill	Tullibigeal	-33.796500	146.084117	310	15.3 ± 0.4†	50.92	3.58	9.55	10.00	0.12	6.97	7.30	2.18	5.29	1.25	2.11	99.26
1801	Griffith	Tullibigeal	-34.232467	145.914017	122	14.9 ± 1.0†	41.03	3.72	7.66	11.78	0.17	16.98	9.27	2.97	1.89	1.12	1.75	98.34
2001	Cosgrove	Shepparton	-36.350102	145.597711	128	8.9 ± 0.2†	42.30	4.66	10.07	13.19	0.17	7.56	11.62	2.54	1.18	1.37	4.17	98.80
2101	Violet Town	Shepparton	-36.683945	145.691123	250	6.8 ± 0.2‡	42.84	4.06	9.46	12.83	0.16	9.14	10.27	3.95	1.34	1.22	3.14	98.42
2102	Violet Town	Shepparton	-36.683945	145.691123	250	6.8 ± 0.2‡	44.85	3.52	10.50	12.63	0.17	9.01	9.98	3.25	1.41	1.02	2.66	99.00

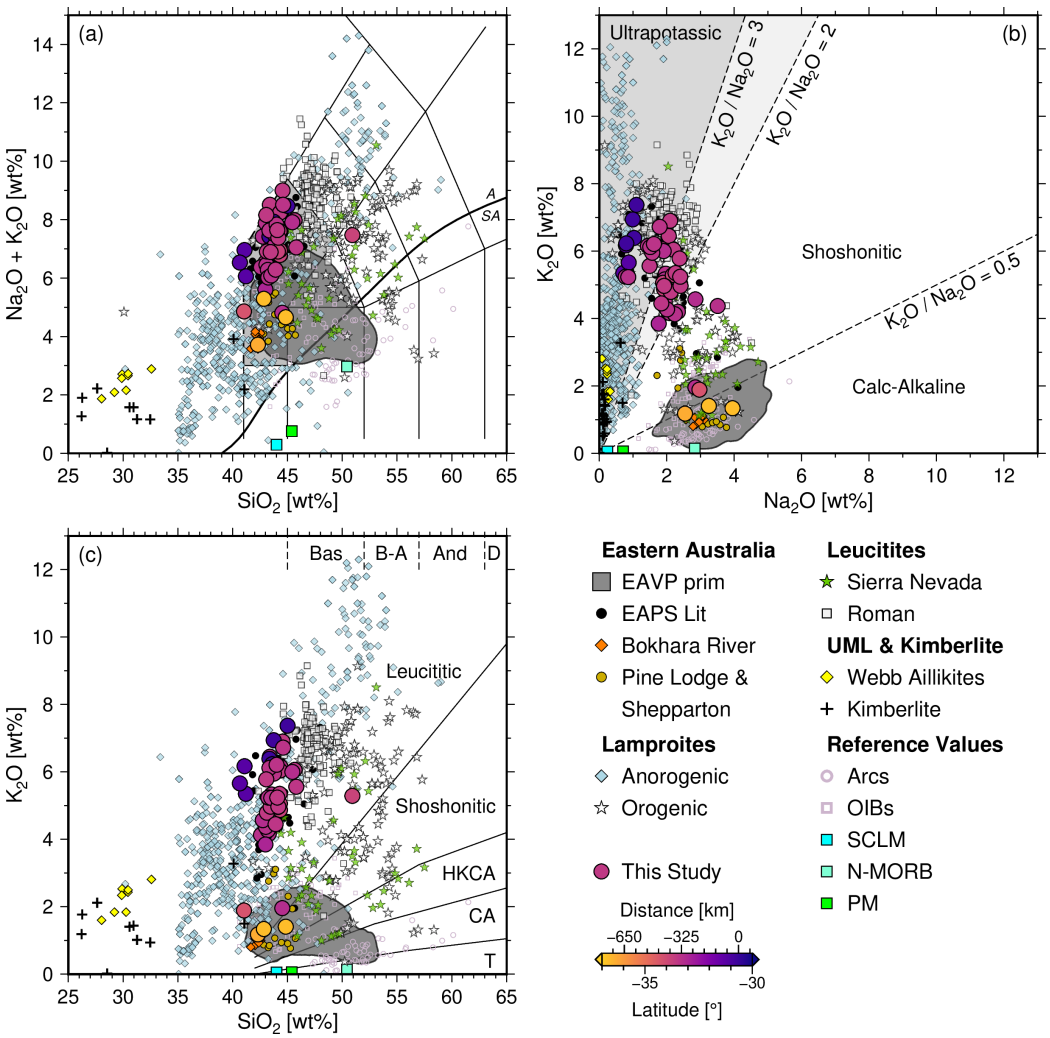

Fig. 3. Major element discrimination diagrams showing data from this study in (a) unnormalised total–alkali versus silica (TAS), (b) K_2O vs. Na_2O, and (c) K_2O vs. Si_2O space. Note: that for volatile–rich (i.e. $H_2O^+ \geq 2$wt% and $CO_2 \geq 0.5$ wt%, or LOI ≥ 2.5 wt% (Le Maitre et al., 2002)) samples like ours the TAS cannot be used for classification purposes, but is provided for general information purposes. TAS (a) after Tilley (1950) with volcanic rock classification fields (Le Bas et al., 1986), and alkalinity divide (label: *A–SA;* Irvine and Baragar, 1971). Potassium–sodium diagram (b) after Middlemost (1975); ultrapotassic field divide follows Foley et al. (1987). Potassium–silica diagram (c) after Middlemost (1975) and Peccerillo and Taylor (1976); dividing lines and field names of Wheller et al. (1987). Range of published EAVP data that passes chemical screens *(see text for specifics)* represented by polygons (darkest grey); i.e. highest density of points usually > 80% of all analyses. EAPS symbols (large circles) coloured by latitude in (a)–(c). Data sources: Shea et al. (2022)(EAVP and EAPS Lit); Shea et al. (2024) (Bokhara River); Sudholz et al. (2023) (Webb Aillikites); Paul et al. (2005) (Pine Lodge and Shepparton); Sarkar et al. (2025) (anorogenic lamproites only); Casalini et al. (2022) (orogenic and anorogenic lamproites); Farmer et al. (2002) (Sierra Nevada leucitites); Plank (2005) (Arcs); Willbold and Stracke (2006) (OIBs); Palme and O'Neill (2013) (primitive mantle (PM)); McDonough (1990) (sub–continental lithospheric mantle (SCLM)); Gale et al. (2013) (N-MORB). Roman province and selected kimberlites compiled from GEOROC database (**https://georoc.eu/**; version 2023-12-01). Full list of data references in the Supplement.

order to remove orangeite samples (also described as *"carbonate-rich-olivine-lamproites"*) which have been the subject of some recent debate (Pearson et al., 2019; Tappe et al., 2022), we further filtered the data compilation from Sarkar et al. (2025). The filters used, based on the statistical analysis of Pearson et al. (2019), were: $SiO_2 \geq 35$ wt%; $K_2O/Na_2O \geq 1$; $CO_2 \leq 3$wt%; and CaO wt% < group 1 bound defined by Foley et al. (1987) [i.e. $CaO = 0.7 \times Al_2O_3 + 6$]. Note, of the anorogenic lamproites that pass our filters roughly 272 are West Kimberley lamproites (Figure 1a), the only other Cenozoic potassic magmatism in Australia (Jaques and Foley, 2018; Jaques et al., 1984; Phillips et al., 2022). Orogenic lamproites are more enriched in Al_2O_3 and, marginally, Na_2O, but with lower TiO_2 and FeO than the anorogenic lamproites and EAPS lavas (Figures 3b, 4b–d, and 5b). However, anorogenic lamproites are clearly delineated by lower CaO than the EAPS, which overlap with orogenic lamproites and Sierra Nevada leucitites as well as intraplate basalts from the broader EAVP (Figures 5c and 6a,b,d).

Table 2. Continued.

ID	TA[x]	Mg#[y]	K_2O/Na_2O	K/Na^z	$(Na+K)/Al^z$	K/Al^z	N	C	H	S (IR)	S (TCD)	CO_2	H_2O (wt%)
0901.1	7.93	69.09	7.03	4.62	0.99	0.82	206	1237	2675	330	306	4532	4.78
0901.2	7.42	69.36	6.19	4.07	1.01	0.81	162	1153	2041	306	281	4223	3.65
0901a.1	8.48	60.93	6.69	4.40	1.15	0.93	169	942	1573	7	13	3451	2.81
0901a.2	7.03	67.27	7.75	5.10	0.96	0.81	189	839	2693	220	200	3076	4.81
0801	6.07	71.88	7.50	4.93	0.95	0.79	213	1319	3559	279	255	4833	6.36
0802	6.96	71.90	7.83	5.15	1.08	0.90	204	2459	2495	17	18	9010	4.46
0803	6.53	72.30	6.47	4.26	1.04	0.84	186	2584	2966	258	240	9468	5.30
1501	5.61	71.54	2.19	1.44	0.82	0.48	133	518	3456	31	23	1898	6.18
0701	7.42	68.26	1.60	1.05	1.11	0.57	139	480	2458	66	59	1759	4.39
1402	4.81	66.70	0.69	0.45	0.74	0.23	140	1133	2396	30	21	4151	4.28
1403	7.09	73.00	2.67	1.75	1.09	0.70	108	605	2755	28	20	2217	4.92
1401	7.91	72.94	3.14	2.07	1.16	0.78	143	654	541	47	11	2396	0.97
2201	6.02	74.87	6.75	4.44	0.92	0.75	261	1363	2157	285	273	4994	3.86
2202	6.08	74.70	6.12	4.02	0.92	0.74							
0203	7.88	70.02	1.25	0.82	1.15	0.52	124	874	2146	9	5	3202	3.84
0202	6.28	70.34	2.12	1.40	0.88	0.51	132	700	2039	13	3	2565	3.64
0201	6.46	69.89	2.33	1.53	0.89	0.54	91	972	1797	15	8	3561	3.21
0302	7.30	71.51	2.71	1.78	1.05	0.67	105	611	1829	17	12	2239	3.27
0301	7.59	71.67	4.27	2.81	1.04	0.77	205	924	1809	13	6	3386	3.23
0105	6.37	70.20	1.84	1.21	0.89	0.49	164	987	1416	29	20	3616	2.53
0101	6.25	70.29	1.99	1.31	0.87	0.49	206	360	2112	166	147	1319	3.77
0102	6.29	69.93	2.19	1.44	0.87	0.51	175	428	2206	94	77	1568	3.94
0103	6.37	70.54	1.86	1.22	0.89	0.49	162	477	2371	71	53	1748	4.24
0104	6.53	69.81	1.80	1.19	0.90	0.49	210	665	1618	46	38	2437	2.89
1602	7.63	72.31	4.05	2.66	1.17	0.85	147	972	1339	14	6	3561	2.39
1604	7.83	72.04	3.84	2.53	1.16	0.83	88	761	1405	14	3	2788	2.51
1603	8.51	67.15	3.75	2.47	1.25	0.89	100	1171	1347	21	18	4291	2.41
1601	7.52	71.87	3.80	2.50	1.13	0.81	105	1826	2174	8	4	6691	3.89
2301	6.29	75.06	2.42	1.59	0.94	0.58	246	1012	1383	45	45	3708	2.47
0402	7.98	71.78	3.16	2.08	1.16	0.78	161	643	1916	29	26	2356	3.42
0401	7.05	73.05	3.73	2.46	1.02	0.73	350	703	1694	26	23	2576	3.03
2501	7.39	69.26	2.06	1.36	1.01	0.58	241	461	603	44	49	1689	1.08
2502	7.65	69.02	2.18	1.43	1.06	0.63	224	523	410	48	75	1916	0.73
2601	8.16	66.68	2.43	1.60	1.23	0.76	295	2804	491	60	89	10274	0.88
0502	8.51	69.04	3.13	2.06	1.25	0.84	84	535	712	239	236	1960	1.27
0501	9.00	69.03	3.29	2.16	1.28	0.88	112	308	1091	43	35	1129	1.95
0503	8.24	69.27	2.74	1.80	1.18	0.76	121	2598	637	20	30	9519	1.14
1904	6.89	72.09	2.60	1.71	1.02	0.64		951	1113	27	42	3485	1.99
1903	6.91	72.76	2.26	1.48	1.01	0.61		830	654	32	41	3041	1.17
1902	7.62	71.13	2.37	1.56	1.06	0.65	55	1227	1635	21	20	4496	2.92
1701	6.79	75.25	2.54	1.67	1.00	0.62	108	1279	1938	35	26	4686	3.46
1702	6.95	75.19	2.68	1.76	1.03	0.65	247	1089	1931	22	17	3990	3.45
1704	6.91	74.75	2.55	1.67	1.01	0.63	57	1110	2238	19	16	4067	4.00
1703	7.46	60.54	2.43	1.60	0.97	0.60	86	1414	2016	19	14	5181	3.60
1801	4.86	76.04	0.64	0.42	0.91	0.27	44	484	2799	52	40	1773	5.00
2001	3.71	55.78	0.46	0.30	0.54	0.13	324	1562	3185	55	62	5723	5.69
2101	5.30	61.07	0.34	0.22	0.84	0.15	249	1186	2431	92	85	4346	4.34
2102	4.67	61.08	0.43	0.29	0.66	0.15	257	984	2006	57	60	3605	3.59

Age References= † : Cohen et al. (2008); ‡ : *"Woodend"* field age from Wellman and McDougall (1974); All other ages from Wellman et al. (1970).

[x]= K_2O+Na_2O (wt%)

[y]= Mg# = 100 × [Mg/(Mg+Fe^{2+})]

[z]= molar

Orogenic lamproites also show significant spread in K_2O versus SiO_2 and K_2O versus Na_2O space traversing the calc–alkaline to leucititic fields, and shoshonitic to ultrapotassic fields in Figure 3b, c. In contrast, anorogenic lamproites are much more restricted in both K_2O versus SiO_2 and K_2O versus Na_2O space, exclusively plotting within the leucititic and ultrapotassic fields (Figure 3b, c). Other Australian alkaline rocks are included for comparison, specifically the Mount Webb aillikites that erupt through thick lithosphere in Central Australia (Sudholz et al., 2023) and the basanitic Bokhara River diatremes (Shea et al., 2024, Figure 1a, b). The Bokhara River locality was inferred to be part of the same volcanic event as the EAPS (Cohen et al., 2008; Jaques, 2002) until a recent investigation showed these diatremes to be

Jurassic in age (Shea et al., 2024). The Webb Aillikites show greatest affinity to kimberlites from Tikiusaaq in western Greenland and less frequently with the anorogenic lamproites, but share almost no major or minor element characteristics with the EAPS (Figures 3a–c, 4, and 5a–d). Bokhara River, however, does share some chemical similarity with the less enriched expressions of the EAPS, most notably Wallaroi Hill and the southern localities at Pine Lodge, Shepparton, and Griffith (Figures 1b, d, e and 3a–c).

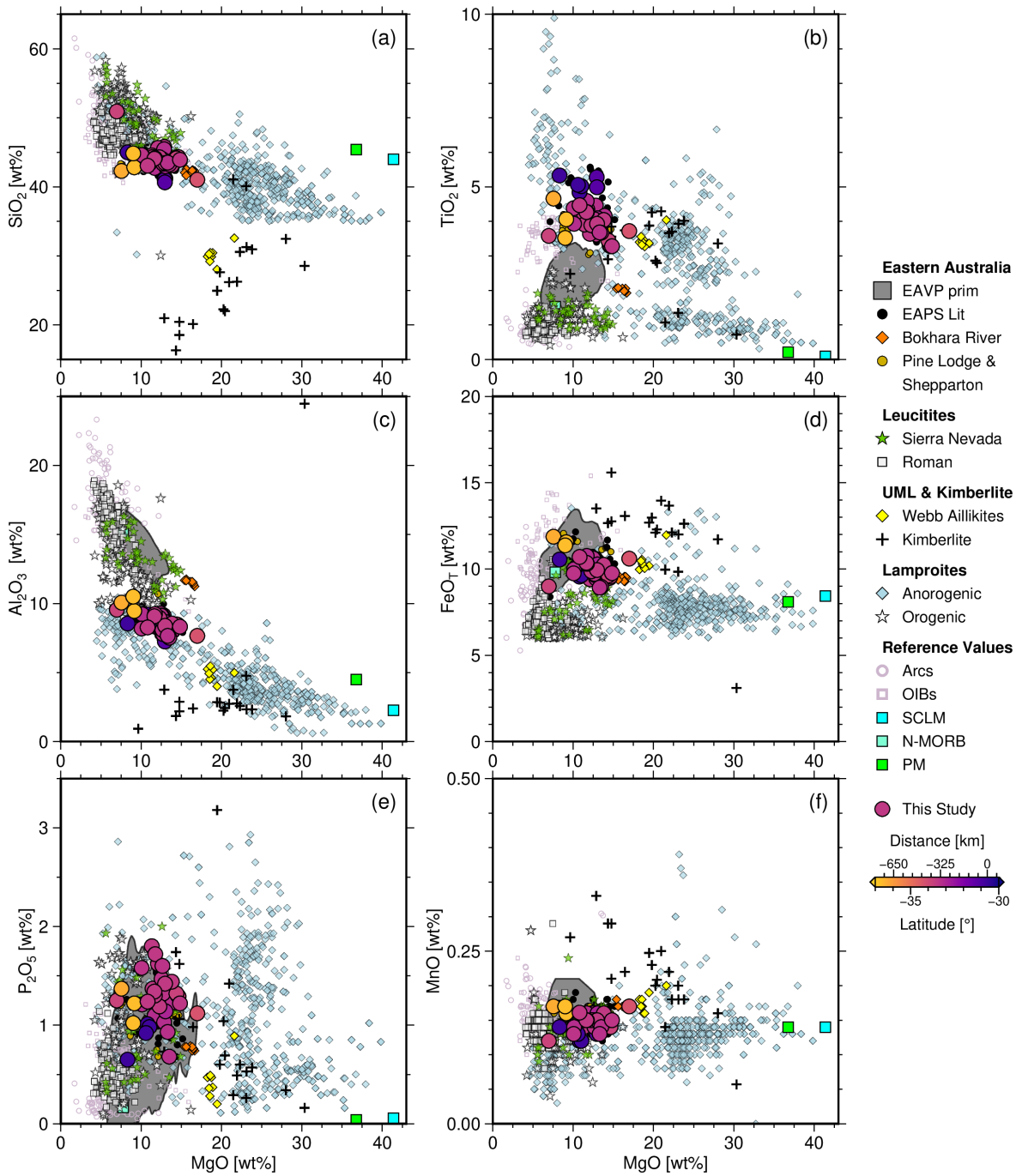

Fig. 4. Major element 'Harker' variation diagrams displaying all major and selected minor elements against MgO wt% with EAPS lavas plotted together with published data. EAVP prim point density polygon covers > 80% of all analyses in most cases. Data sources for published literature as in Figure 3; full references in the Supplement.

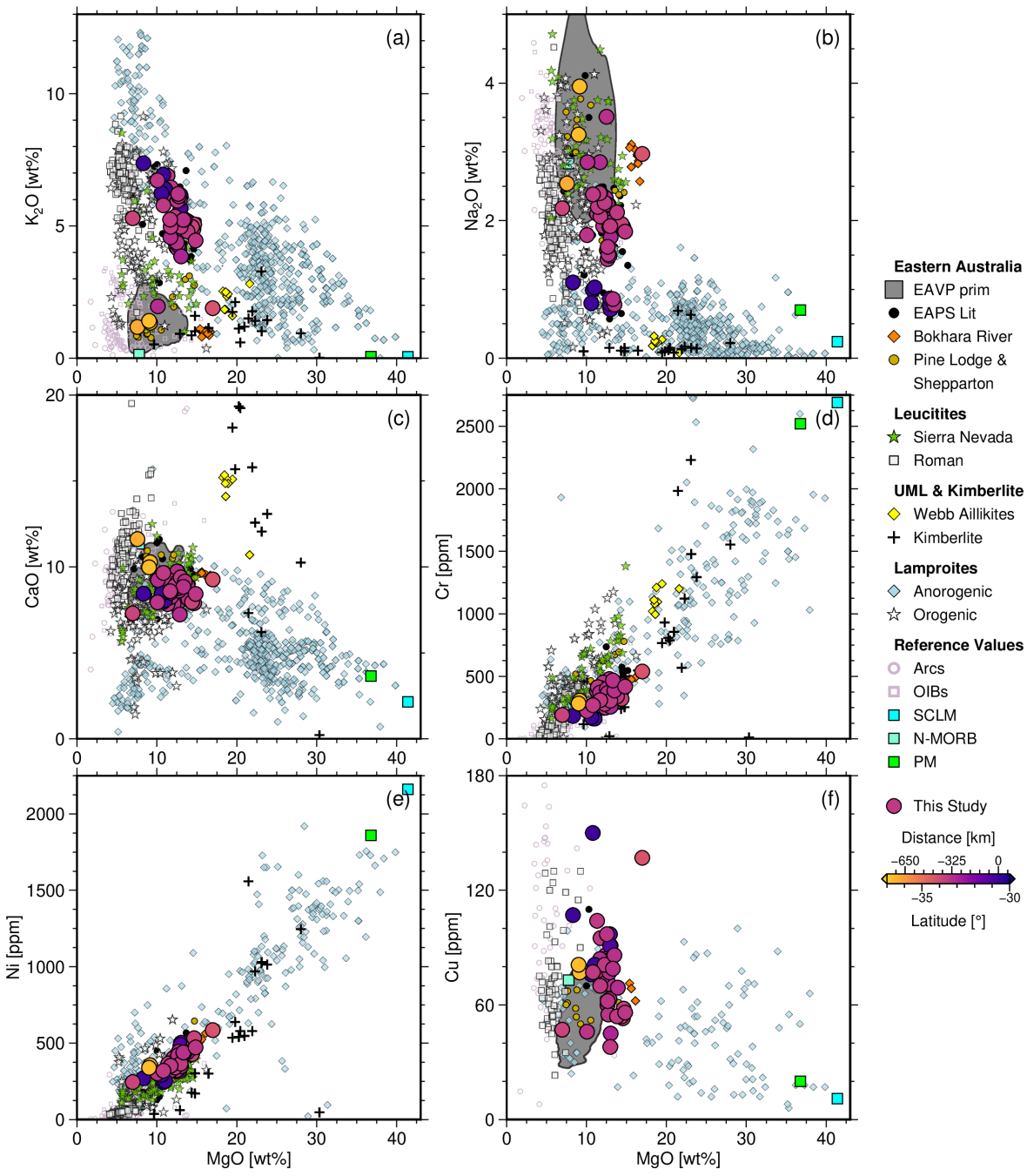

Fig. 5. Alkaline major element variation diagrams and select trace elements against MgO wt% for EAPS lavas and published data. EAVP prim point density polygon covers > 80% of all analyses in most cases. Data sources for published literature as in Figure 3; full references in the Supplement.

Trace Element Geochemistry

The EAPS rocks display a flat enrichment in the HFSE and LILE's, when compared with the average concentration of leucitites and lamproites, with approximately 100× N–MORB and up to 1000× primitive mantle (PM) values for Ba (Figure 7a and e–h). Regardless of the normalising system chosen, Ti exhibits a slight negative anomaly and Eu is unaffected by feldspar fractionation, whereas a minor negative PM–normalised Pb signature is observed for the central and southern EAPS outcrops. In contrast, the northernmost outcrops, Byrock and El Capitan (Figure 1a–c), exhibit no Pb anomaly (Figure 7a). The lack of negative Nb–Ta anomaly and Ce/Pb values largely within the mantle array do not support evidence of subduction input, while the strong convex upward up shape of the pattern results in high

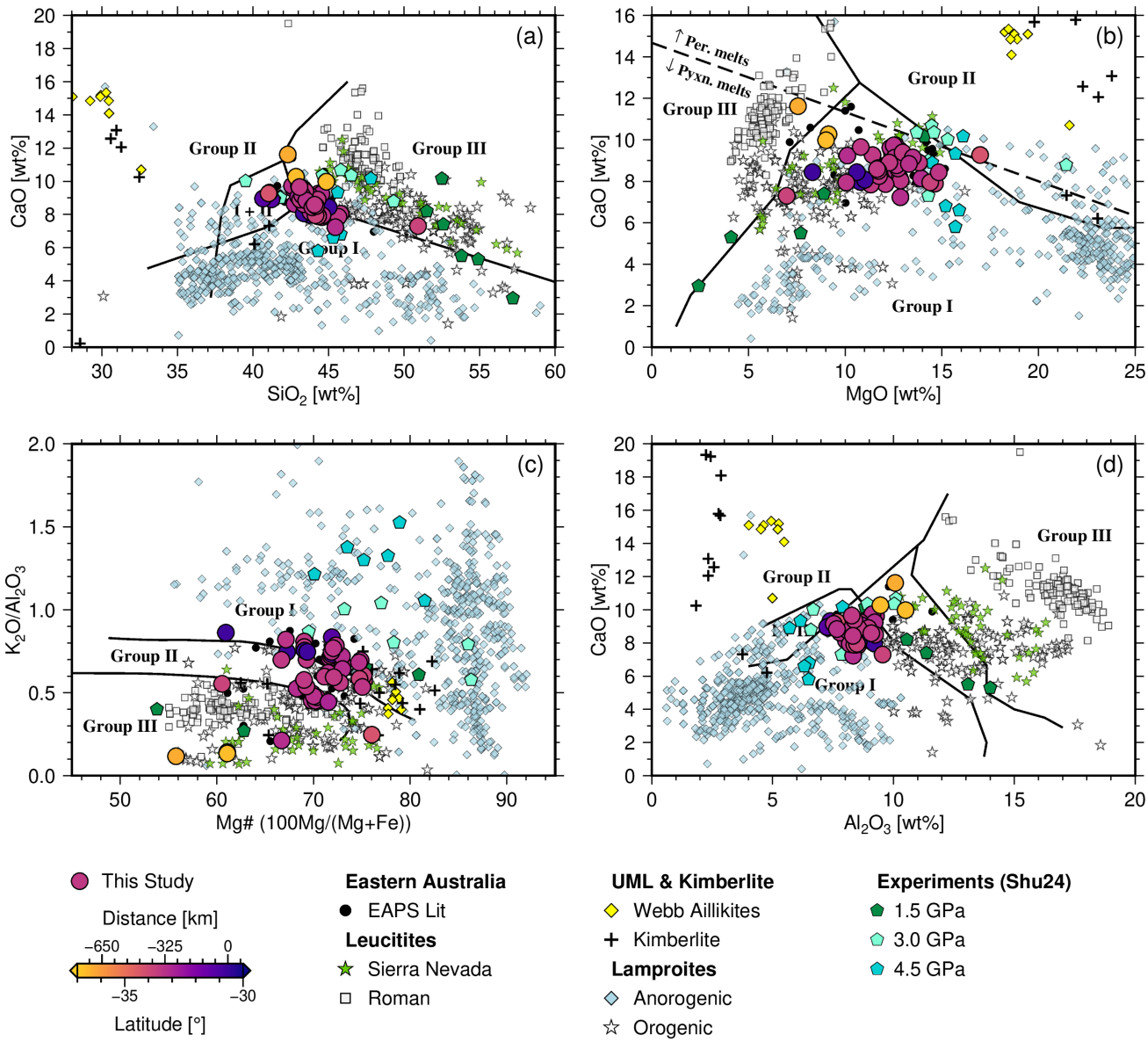

Fig. 6. Lamproite discrimination diagrams as defined by Foley et al. (1987), showing the EAPS lavas analysed in this study compared to values for other alkaline lavas. Group I, II, and III refer to I – lamproites, II – kamafugites, III – leucitites (Foley et al., 1987). Coloured pentagons correspond to high-pressure hydrous pyroxenite experiments from Shu et al. (2024) and Shu et al. (in revision). Note the EAPS lavas south of Griffith (34°S; yellow and orange circles) are not ultrapotassic. Pyroxenite and peridotite partial melt divide is plotted in (b) as shown in Herzberg (2011) and Herzberg and Asimow (2008). Data sources for published literature as in Figure 3; full references in the Supplement.

La/Yb and Sm/Yb values that suggest significant garnet in the mantle source (Figure 7a). Patterns are steep among the EAPS samples, yet illustrate decreasing enrichment from north to south with the southern volcanoes often exhibiting the lowest PM–normalised values of the suite (Figure 7a). Values for Ba vary the most dramatically, from 6940 ppm for the El Capitan volcano (sample 0803) to 573 ppm for sample 1603 within the Tullibigeal fields (Table 3). Rb and Sr are also most enriched within the El Capitan volcano, with Rb = 366 ppm and Sr = 2824 ppm for samples 0803 and 0801 respectively. The Griffith sample (1801) exhibits the lowest concentrations of both Rb and Sr (41 and 940 ppm), while also having Cs contents of 0.97 ppm which is significantly below the average of all samples (1.44 ppm) and only higher than the southernmost samples from Violet Town (Table 3; Figure 1e), which also exhibits a strong negative K anomaly (*yellow lines*; Figure 7a). Due to the apparent alteration (Figure 2e), the Pine Lodge outcrop near Cosgrove (sample 2001) was not analysed for trace elements in this study but was previously analysed by Paul et al. (2005) whose data also show lower–than–average concentrations of fluid–mobile

elements such as Cs, Rb, Ba, Th, U, K, and Sr (*gold circles*; Figure 7b). Interestingly, HREEs heavier than Dy cross the N–MORB values which is a common feature of melts from the EAPS, EAVP, lamproites, and Sierra Nevada leucitites, but is absent in the Roman Province leucitites (Figure 7a–g). The most similarity is shared between our samples and both kimberlites and anorogenic lamproites (Figure 7d and f). It should be noted that among the potassic rocks plotted (Figure 7e–h), both lamproite groups display a much larger range of values (grey band in Figure 7e–f) than those of the leucitites (Figure 7g–h). Comparing the EAPS to orogenic lamproites there is a clear lack of strong positive Pb, and strong negative Nb, Ta, and Ti anomalies associated with the orogenic lamproite group. Barium and Th are on average more enriched in the published orogenic lamproite samples than samples presented here, as are Yb and Lu (Figure 7e). Anorogenic lamproites, on the other hand, show relatively good agreement with the EAPS samples and share both Pb and Sr anomalies (Figure 7f). The primary deviation of the EAPS from the average anorogenic lamproite occurs for Rb, Ba, La, and Ce, however these are minor except for Ba (Figure 7f). Both of the published leucitites fields included for comparison show overall less enriched patterns (Figure 7g–h). The leucitites of the Roman province lavas deviate from the EAPS with strongly positive Ce, Th, U, and Pb anomalies, moderately negative Zr and Hf, and strongly negative Nb, Ta, P, and Ti (Figure 7g). The EAPS sit above the average Sierra Nevada leucitites from Nb – Pr, and again from Nd – Er (Figure 7h). Interestingly for the heaviest rare earth elements (i.e Yb and Lu) both of the sub-groups associated with subduction, the orogenic lamproites and Roman province leucitites (Figure 7e and g) are more enriched than the EAPS while the intraplate magmas, the anorogenic lamproites and Sierra Nevada leucitites, are similarly depleted to the EAPS (Figure 7f and h).

Volatile Element Geochemistry

CHNS analyses reveal that the northern exposures of Byrock and El Capitan are the most sulfur–enriched of all the EAPS lavas with up to 330 ppm S, which is a roughly six times higher than the remainder of the localities included here that contain in the order of 50 ppm or less (Table 2; Figure 8c). Carbon contents range between 839 and 2459 ppm for the northern localities, and over a similarly large range for the the central exposures (308–2804 ppm; as CO_2 = 1129–10274 ppm; Table 2; Figure 8d). Nitrogen is the only element where measurements fall below the long–term detection limits established by Ananuer and Alard (in prep.), but all values are above the intrinsic detection limits of the technique. Given the scarcity of published measurements for N we report all values measured for this study, however analyses below 150 ppm should be treated with caution (Figure 8b). N concentrations are highest in the central area but also exhibit the most variation (44–350 ppm), while the northern lavas cluster around 162–213 ppm N (Table 2; Figure 8b). Hydrogen varies between 410–3559 ppm, which is equivalent to 0.73–6.36 wt% H_2O, across the entire EAPS and displays no clear trend or clustering between eruptive centres (Table 2; Figure 8a). The southern centres of Shepparton and Pine Lodge show moderate variation and are generally more enriched in H and N, and slightly enriched in C compared to the remaining localities measured in the central and northern areas, while S contents are within error of the average. Shepparton is more enriched in C, H, and N (1562, 3185, and 324 ppm respectively), but slightly depleted in S (55 ppm) in comparison to Pine Lodge (C= 1186, H= 2431, N= 249, S= 92 ppm; Table 2).

Compared to published values the EAPS analyses show similarity with lamproites, lamprophyres and leucitites with respect to H_2O and S contents, but are most similar to lamproite CO_2 contents (Figure 8a, c, and d). H_2O contents also overlap with some kimberlites, specifically those from west Greenland (Tappe et al., 2017). However, kimberlites as a group span a large range of values for H_2O, S, and CO_2 (Figure 8a, c and d). Sulfur contents of the EAPS also resemble those of the Roman leucitites and other leucitites globally, but the EAPS are more magnesian overall (Figure 8c). Published literature that combines analysis of both trace elements and volatile elements is scarce (e.g. Tappe et al., 2017), although new compilations are becoming more common (Giuliani et al., 2024). Further, volatile elements are rarely measured by dedicated methods like we have employed here. Nitrogen is perhaps the best example of this with the available published data being severely limited (Figure 8b), however the reliability of published S analyses is also questionable given most data are determined

Table 3. Trace element concentrations, in ppm, of the EAPS samples (arranged by increasing degrees of latitude south).

ID	0901.1	0901.2	0901a.1	0901a.2	0801	0802	0803	1501	0701	1403	1401	2201	2202	0203	0202	0201	0302	0301	0105	0101	0102	0103
Li	7.83	8.30	9.48	8.68	9.03	7.70	9.07	5.61	7.70	5.97	8.08	8.10	8.19	7.88	7.66	7.92	7.09	6.78	7.51	7.46	7.80	7.61
Be	5.45	5.52	6.38	5.71	6.16	5.75	6.81	3.45	4.57	3.57	5.63	6.77	8.26	3.84	3.62	3.75	4.65	3.98	3.95	3.95	4.13	3.95
Sc	19.8	19.1	21.9	20.2	20.2	21.4	19.2	16.3	22.4	17.7	19.0	21.8	21.4	24.4	23.3	24.0	21.0	22.2	25.4	24.3	23.5	24.6
Ti	28761	29886	32861	30685	31479	34015	30345	20401	28956	22599	24904	22488	22108	25108	22538	24492	26016	25348	22514	23984	22794	24707
V	187	188	217	194	201	204	184	136	237	182	184	168	163	229	221	229	196	174	233	226	228	236
Cr	164	162	183	175	369	356	261	258	370	315	341	387	467	415	420	440	419	451	348	317	249	343
Mn	863	897	1033	985	1142	1055	996	905	1249	1022	1064	1076	1008	1256	1221	1255	1135	1115	1256	1205	1214	1224
Co	51	52	53	54	63	62	60	43	57	53	52	55	53	56	56	56	55	55	56	54	55	55
Ni	244	251	270	292	502	476	488	348	319	432	434	440	439	323	325	324	409	403	329	319	316	316
Cu	150	81	107	76	91	97	91	45	84	69	77	86	79	83	80	84	71	60	80	76	81	83
Zn	119	122	134	126	145	135	134	99	131	103	115	110	114	119	114	117	122	118	117	118	117	118
Ga	21.0	20.0	22.5	21.0	21.0	21.0	20.0	15.0	19.8	17.0	20.0	18.6	18.7	19.0	18.0	19.0	19.0	18.0	20.0	19.0	19.0	19.0
Rb	188	172	214	168	258	305	366	117	121	167	134	282	230	101	108	129	101	139	112	100	115	95
Sr	1939	1959	1514	1972	2824	2323	2405	1110	1416	1017	1314	2090	2416	1274	1213	1302	1192	1311	1255	1230	1282	1287
Y	31.0	31.0	35.0	31.0	37.0	35.0	36.0	28.0	31.5	26.0	28.0	29.7	32.3	30.0	28.0	29.0	29.0	28.0	29.0	29.0	29.0	29.0
Zr	650	651	810	691	804	798	778	567	713	655	806	905	1011	576	530	554	667	588	571	546	553	572
Nb	152	153	186	158	169	178	165	101	116	114	126	164	160	114	103	108	103	88	99	106	78	108
Mo	0.39	0.39	0.67	0.38	0.34	0.63	0.63	1.01	0.81	1.04	0.85	0.45	0.67	1.72	1.63	1.82	1.00	0.70	1.52	1.83	1.56	1.67
Cd	0.09	0.08	0.09	0.07	0.14	0.08	0.09	0.05	0.10	0.08	0.07	0.12	0.12	0.09	0.09	0.09	0.08	0.08	0.08	0.09	0.10	0.09
Sb	0.20	0.18	0.18	0.17	0.20	0.20	0.27		0.15		2.51		0.22	0.12	0.11	0.13	0.13	0.12	0.09	0.17	0.11	0.12
Cs	1.92	1.92	2.10	1.84	1.80	1.75	2.90	1.04	1.58	1.54	1.64	2.13	2.79	1.34	1.29	1.34	1.16	1.33	1.31	1.30	1.32	1.30
Ba	2133	2196	1739	4536	3106	2819	6940	913	1506	1318	1339	5014	2981	1221	1144	1221	1134	1027	1044	1173	1210	1087
La	159	162	195	165	213	196	212	110	96	102	105	130	138	88	84	85	94	95	83	84	87	82
Ce	306	312	374	318	413	385	411	233	207	216	222	268	294	188	176	182	204	206	174	175	183	174
Pr	35.6	36.1	41.5	36.8	46.3	43.3	46.8	29.7	26.5	27.6	27.2	33.3	35.5	23.4	21.8	22.6	25.7	26.3	21.4	21.6	22.8	21.3
Nd	128	131	150	133	165	155	168	113	102	104	104	122	134	89	85	87	99	103	83	84	89	83
Sm	18.1	18.4	21.4	18.8	22.8	21.6	23.6	17.8	16.4	17.0	16.0	18.5	19.9	14.5	13.7	14.2	16.1	16.3	13.6	13.8	14.3	13.6
Eu	5.30	5.40	6.17	6.20	6.70	6.30	8.10	5.00	4.82	5.00	4.60	6.06	5.99	4.30	4.10	4.20	4.70	4.80	4.00	4.10	4.30	4.00
Gd	15.4	15.8	14.9	16.1	19.4	18.2	20.2	12.6	11.7	12.4	13.1	12.5	13.2	12.3	11.7	12.0	13.2	13.4	11.4	11.5	12.0	11.4
Tb	1.62	1.65	1.89	1.66	1.95	1.84	2.04	1.57	1.53	1.58	1.43	1.58	1.70	1.43	1.36	1.40	1.50	1.48	1.30	1.33	1.40	1.30
Dy	6.58	6.70	7.58	6.67	7.56	7.17	8.04	6.43	6.46	6.78	6.01	6.33	6.94	6.21	5.89	6.04	6.28	6.12	5.65	5.81	6.07	5.63
Ho	1.09	1.11	1.24	1.09	1.21	1.14	1.29	1.02	1.05	1.11	0.99	1.03	1.13	1.05	0.99	1.02	1.03	0.99	0.93	0.97	1.02	0.94
Er	2.75	2.80	3.10	2.73	3.02	2.82	3.23	2.45	2.58	2.74	2.38	2.52	2.76	2.61	2.45	2.53	2.52	2.40	2.31	2.41	2.52	2.34
Yb	1.72	1.71	1.88	1.66	1.66	1.54	1.83	1.42	1.59	1.74	1.52	1.52	1.73	1.68	1.58	1.64	1.52	1.43	1.50	1.58	1.64	1.51
Lu	0.23	0.23	0.24	0.22	0.22	0.20	0.24	0.18	0.21	0.23	0.20	0.19	0.23	0.23	0.22	0.22	0.20	0.19	0.20	0.21	0.22	0.20
Hf	14.5	14.8	18.0	15.4	15.7	15.7	17.2	12.8	14.0	17.4	17.2	19.9	22.7	12.3	11.3	12.0	13.5	12.3	10.8	11.3	11.6	11.3
Ta	8.75	8.93	10.34	8.78	7.43	8.43	8.24	5.45	5.62	7.48	6.56	7.78	8.22	6.05	5.41	5.78	6.32	4.44	4.37	5.71	3.13	5.61
W	0.95	1.02	1.11	0.72	1.87	2.38	3.36		0.53		1.71		0.84	3.73	3.19	2.64	2.73	1.77	2.82	2.02	1.99	1.73
Pb	17.20	17.70	19.91	15.60	16.30	14.30	20.20	8.20	8.21	11.10	11.20	14.14	16.13	8.10	7.90	7.70	8.20	7.60	6.90	7.60	8.00	6.60
Th	17.60	17.60	22.13	17.40	19.10	16.30	21.10	9.70	7.80	13.30	11.40	12.46	14.38	9.20	8.70	8.90	7.80	6.70	8.00	8.80	9.20	8.20
U	3.44	3.44	3.71	3.43	3.49	3.21	4.38	2.45	2.01	3.06	2.65	3.14	3.50	2.16	1.98	2.52	1.96	1.74	1.82	1.95	1.98	2.05

Table 3. Continued.

ID	0104	1602	1604	1603	1601	2301	0402	0401	2501	2601	0502	0501	0503	1904	1903	1902	1701	1702	1704	1703	1801	2101	2102
Li	7.62	7.59	7.32	6.79	7.17	6.59	8.95	9.00	7.86	5.91	7.18	7.45	6.79	6.32	6.52	7.42	6.06	6.60	5.49	5.81	5.38	5.74	6.33
Be	4.02	4.64	5.15	5.26	3.85	3.04	5.58	4.98	4.51	4.43	5.02	5.32	4.77	3.72	3.54	4.49	3.48	3.88	3.21	3.06	2.51	3.84	2.74
Sc	25.2	20.1	19.8	16.7	21.5	19.8	20.3	20.8	19.1	20.8	21.6	19.9	21.3	21.8	21.9	21.1	17.9	19.8	16.4	15.0	21.8	22.0	24.2
Ti	25531	24521	24949	25557	26014	19131	22815	22577	25999	26008	28038	24535	24494	23520	23662	23334	16177	20519	16982	18437	21550	24363	22165
V	241	164	170	140	223	166	169	160	197	191	202	176	195	179	205	190	142	167	141	144	209	236	251
Cr	350	314	367	223	400	418	450	478	309	269	407	381	413	306	339	279	398	429	320	191	539	306	283
Mn	1246	1117	1086	950	1189	1071	1057	1120	1127	1137	1179	1104	1148	1121	1132	1119	1019	1105	929	773	1156	1199	1301
Co	56	53	50	43	57	56	49	52	52	50	51	49	52	54	56	52	52	56	47	36	63	57	60
Ni	324	444	421	302	404	472	405	429	352	319	343	343	367	366	441	340	487	532	428	245	585	355	339
Cu	86	55	62	46	97	56	75	63	70	77	95	104	78	38	54	81	53	58	54	47	137	77	81
Zn	119	122	128	128	118	100	120	120	121	121	135	132	123	109	107	111	99	110	91	100	99	120	121
Ga	20.0	19.0	18.0	19.0	19.0	15.3	20.0	19.0	18.6	19.1	21.0	20.0	19.0	17.0	17.0	19.0	16.0	17.0	15.0	16.0	14.0	19.7	19.4
Rb	110	138	126	119	108	95	129	145	108	112	112	115	123	119	94	103	100	110	87	86	41	245	86
Sr	1220	1547	1494	1397	1462	1121	1381	1285	1444	1196	1898	2134	1574	1478	1340	1484	1138	1204	1239	1006	940	1116	958
Y	29.0	33.0	34.0	34.0	27.0	24.0	32.0	32.0	28.6	32.6	35.0	34.0	32.0	27.0	27.0	28.0	27.0	29.0	25.0	25.0	23.0	30.3	28.0
Zr	582	681	709	776	579	487	761	690	574	731	758	736	667	573	555	654	505	584	486	459	432	480	374
Nb	111	126	120	105	134	87	102	92	106	119	110	95	106	99	102	117	72	93	76	74	104	99	85
Mo	1.55	0.87	1.26	0.83	1.39	1.16	1.59	0.87	2.08	1.60	3.48	1.19	1.79	1.58	1.79	1.39	1.24	1.27	1.39	1.59	2.06	2.95	2.72
Cd	0.08	0.08	0.11	0.09	0.11	0.12	0.07	0.08	0.11	0.10	0.06	0.06	0.05	0.06	0.03	0.07	0.12	0.11	0.11	0.13	0.06	0.09	0.08
Sb	0.10		0.17	0.13	0.17	0.15	0.16	0.11	0.14	0.12	0.11	0.12	0.10				0.10	0.10			0.13	0.13	0.00
Cs	1.33	1.24	1.26	1.21	1.30	1.35	1.70	1.86	1.36	1.07	1.06	1.08	1.04	1.29	1.19	1.22	1.31	1.38	1.15	1.54	0.97	0.78	0.62
Ba	1051	1157	1299	573	1339	1087	1659	1500	1311	816	1403	1534	1087	1062	1024	1410	1235	1300	1251	998	831	829	726
La	83	128	129	130	88	78	106	108	97	104	115	118	105	90	87	93	85	92	82	70	74	74	57
Ce	176.0	267.0	282.0	277.0	180.0	164.8	226.0	230.0	201.7	222	249.0	254.0	226.0	192.0	186.0	195.0	184.0	196.0	173.0	145.0	157.0	155.8	115.8
Pr	21.8	34.5	34.9	34.5	22.3	20.6	27.9	28.5	25.5	28.6	31.6	31.9	27.9	24.8	24.3	24.7	22.8	24.5	22.3	19.1	19.4	19.6	14.5
Nd	84	131	133	133	84	80	108	111	98	112	124	124	107	92	90	92	90	94	84	71	74	76	56
Sm	13.9	20.3	20.7	20.7	13.6	12.9	16.9	17.5	15.3	17.7	19.5	19.3	16.7	15.2	15.0	15.3	14.3	15.2	13.8	12.2	12.1	13.2	10.7
Eu	4.10	5.80	5.90	5.90	4.00	3.85	5.00	5.10	4.62	5.10	5.70	5.80	4.90	4.50	4.40	4.70	4.30	4.50	4.10	3.60	3.40	3.98	3.29
Gd	11.6	14.3	16.6	16.6	11.4	9.2	14.1	14.5	11.0	12.6	15.9	15.7	13.8	10.9	10.9	11.1	12.0	12.3	9.9	9.1	10.0	10.3	8.7
Tb	1.33	1.80	1.82	1.80	1.29	1.19	1.58	1.62	1.41	1.60	1.77	1.73	1.53	1.40	1.40	1.45	1.33	1.37	1.27	1.20	1.12	1.39	1.19
Dy	5.74	7.45	7.49	7.62	5.64	5.14	6.61	6.74	5.98	6.91	7.30	7.10	6.35	5.86	5.90	6.12	5.80	6.00	5.44	5.28	4.85	6.30	5.58
Ho	0.96	1.19	1.21	1.23	0.94	0.85	1.09	1.11	0.98	1.15	1.20	1.15	1.05	0.95	0.96	1.01	0.97	0.98	0.90	0.88	0.80	1.07	0.97
Er	2.37	2.86	2.87	2.92	2.28	2.04	2.71	2.72	2.35	2.72	2.91	2.83	2.56	2.31	2.33	2.45	2.32	2.37	2.22	2.22	1.94	2.57	2.37
Yb	1.54	1.67	1.67	1.72	1.50	1.31	1.66	1.62	1.41	1.72	1.73	1.62	1.51	1.39	1.44	1.54	1.51	1.54	1.41	1.46	1.23	1.66	1.61
Lu	0.20	0.22	0.22	0.22	0.20	0.17	0.23	0.22	0.18	0.22	0.23	0.21	0.20	0.18	0.19	0.20	0.20	0.20	0.19	0.19	0.16	0.22	0.22
Hf	11.4	14.7	15.1	16.5	12.0	10.4	15.7	14.6	12.0	15.3	15.1	14.4	12.8	12.3	11.9	14.0	10.4	11.9	10.1	10.1	9.3	10.3	7.8
Ta	10.07	6.37	6.37	5.32	7.36	4.70	4.73	5.26	5.85	6.08	5.18	4.16	4.88	5.16	5.46	6.04	3.65	4.60	3.81	4.20	5.94	5.76	4.50
W	2.05		1.83	1.47	1.22	1.66	2.99	2.73	2.10	1.76	2.66	1.41	1.40				1.41	1.74			0.93	1.96	0.00
Pb	7.00	10.60	9.40	11.80	8.50	7.18	10.90	9.80	8.19	8.80	1.80	6.80	6.20	6.90	6.80	9.00	7.80	7.80	7.60	7.70	4.90	4.60	4.80
Th	8.20	11.20	10.80	9.50	10.00	7.36	9.60	8.90	8.70	9.15	7.90	7.90	8.10	7.70	8.00	10.20	8.00	8.10	7.80	7.90	7.70	8.56	6.45
U	1.90	2.91	2.71	2.49	3.53	1.79	2.38	2.22	2.09	2.01	2.01	1.97	1.97	1.99	1.90	2.42	1.76	2.00	1.84	1.81	1.68	1.78	1.52

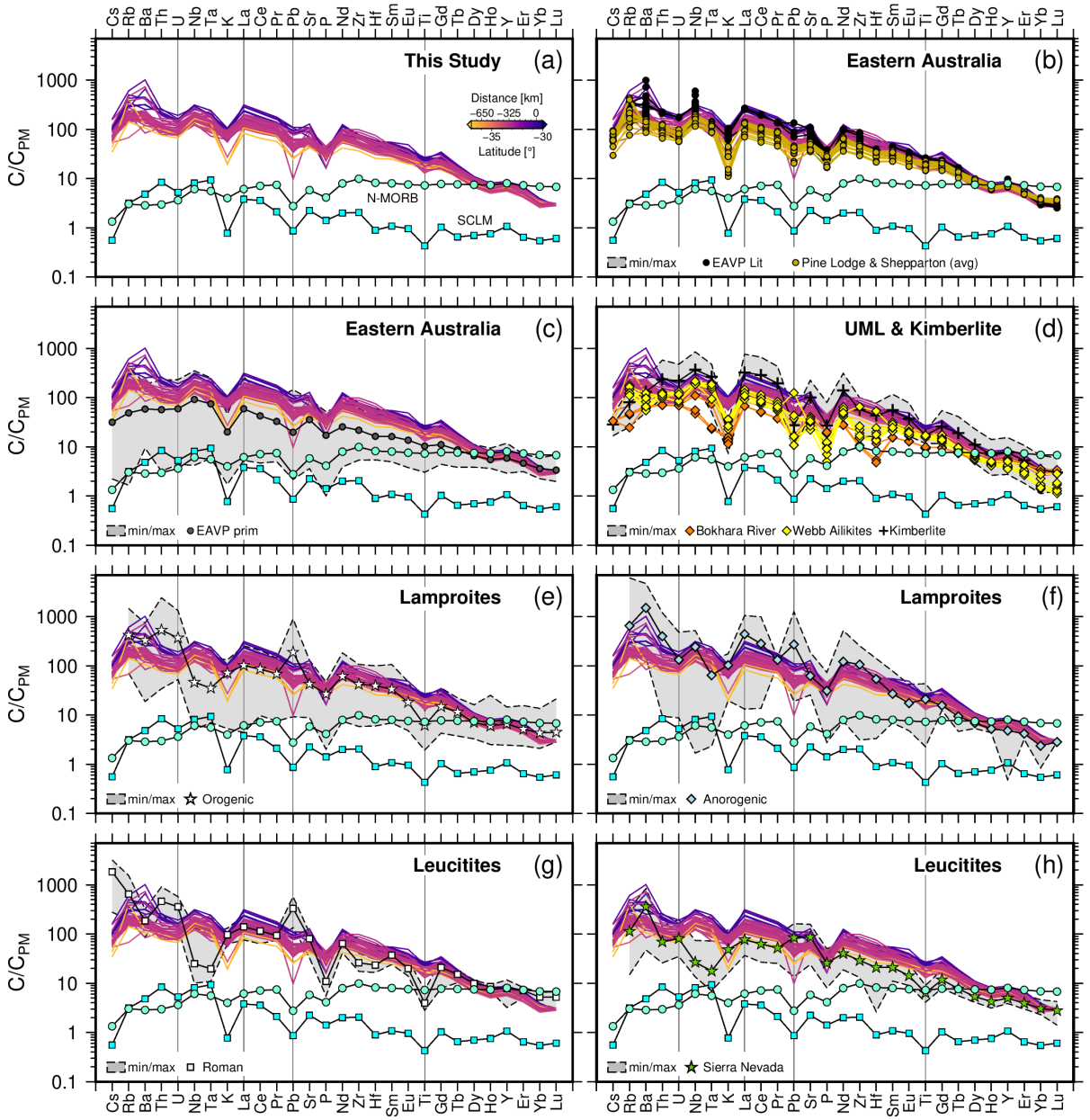

Fig. 7. Trace element variation diagrams with measured trace elements normalised to primitive mantle (PM) values from Palme and O'Neill (2013). All panels show new analyses from this study coloured by latitude with N–MORB values from Gale et al. (2013) and SCLM values from McDonough (1990) included for reference. Panels (b) – (d) shows EAPS comparison with published values for other Australian lavas; (b) published EAPS (note variability in the number of points per element) and the Shepparton lavas analysed by Paul et al. (2005); (c) EAVP primitive lavas; and (d) Bokhara River basanite and Mount Webb ailikite (orange and yellow diamonds, respectively). (d) also includes West Greenland kimberlites (black crosses and grey band; Tappe et al., 2017). The grey bands in panels (c)–(h) represent the absolute range for the dataset plotted within the band; the average pattern for each dataset shown as line with symbol. (a) EAPS (this study); (b) EAPS published values; (c) EAVP primitive lavas; (d) Bokhara, UML & Kimberlite; (e) Anorogenic lamproites (Casalini et al. (2022) only; comparison between Sarkar et al. (2025) and Casalini et al. (2022) in Supplementary Figure 2); (f) Orogenic lamproites; (g) Roman Province leucitites; (h) Sierra Nevada leucitites. Data sources for published literature as in Figure 3; full references in the Supplement.

via XRF. While there are occasional instances where the EAPS samples exhibit elevated volatile element concentrations that are replicated in whole rock trace element ratios or non-volatile elements (i.e. S vs. Cu; S vs. Ni; S vs. Pb; H_2O vs. La/Yb; C vs. $(La/Yb)_N$) these are not consistent across the dataset (Figure 8d; Supplementary Figures 3 and 4). Therefore, unlike the general enrichment trends in major and trace elements (Figures 3–7, and 9), we observe no systematic spatial trend in volatile element geochemistry, nor do we see any clear correlation when plotted against any of the common whole rock trace element ratios for volatile–bearing or influenced sources. This suggests the volatile

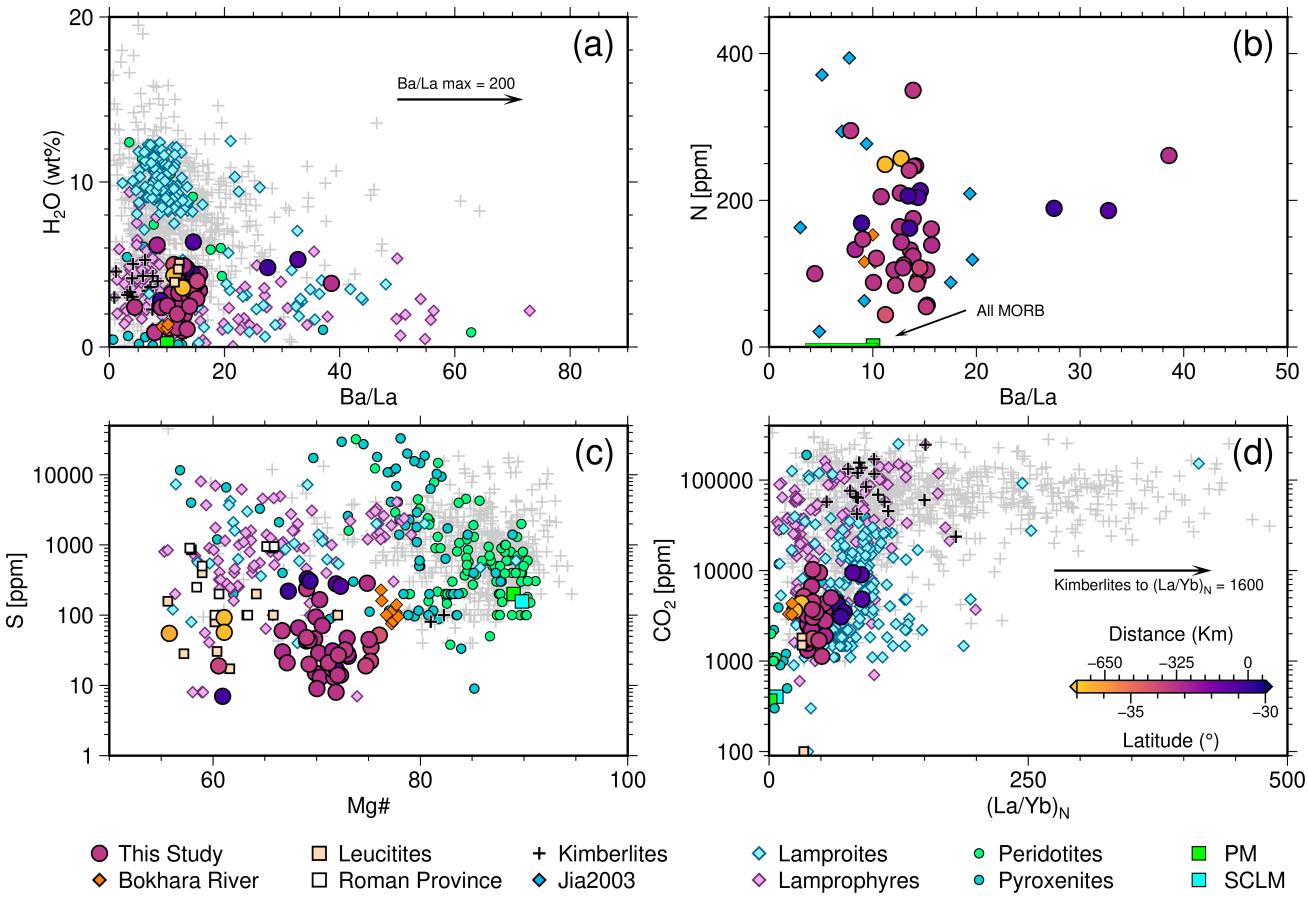

Fig. 8. Volatile element results plotted against relevant trace element ratios or Mg#. H_2O (a) and N (b) are plotted against Ba/La based on similar behaviour and likely source (sediments). Sulfur (c) shows a degree of degassing with samples from the same outcrops showing both high and low-S for similar Mg#. CO_2 (d) also exhibits degassing, but still overlaps with global lamproites, lamprophyres, and some kimberlites. Colours for EAPS (this study) follow the scale plotted on panel (d). Published values are screened for Mg# $\geq$ 55 and represent converted total abundances for all species of that element reported. Data sources:"All MORB" in (b) from Johnson and Goldblatt (2015) and Gale et al. (2013); GEOROC precompiled files (kimberlites, peridotites, pyroxenites, lamproites, lamprophyres, and leucitites); kimberlites from Tappe et al. (2017) highlighted in black; Jia2003 (N-only; lamproites and lamprophyres; Jia et al. (2003)). Full reference list for GEOROC files in the Supplement.

analyses are likely modified by degassing upon ascent and eruption which is not unexpected for potassic and ultrapotassic melts that are considered relatively volatile-laden (Prelević et al., 2004). We tested CO_2/Ba for our samples to investigate if degassing has occurred and, if so, to what degree. Observed ratios between 0.5–13 suggest significant degassing has taken place compared to ratios of around 140 exhibited in undegassed basalts and melt inclusions (Supplementary Figures 3 and 4; Hauri et al., 2018; Matthews et al., 2017, 2021). Degassing, in the case of the EAPS, is most obviously exemplified by the clear separation of values for S from the same outcrops (i.e. Byrock) in Figure 8c, where degassed samples exhibit S $\sim\leq$100 ppm. Given the majority of samples sit at or below this threshold, we suggest that the values reported here represent minimum values and are probably decoupled from the source volatile contents.

Discussion

Classification of the EAPS Rocks

Lamproites as a group of rocks have been considered enigmatic for much of the time since they were first described, and the same can be said for leucitites and leucite–bearing rocks that have been variably described and named around the world. In most cases the name assigned to a rock or outcrop is inconsequential except to give the reader a general idea of the mineralogy or approximate chemical range within which it

sits. Lamproites and leucitites are not easily identified in hand specimen with few obvious markers to isolate what the rock is, perhaps with the exception of phenocrystic phlogopite or leucite in lamproites and leucitites respectively. All naming schemes for highly-alkaline rocks require modal mineralogy and mineral chemistry analyses or microbeam imaging techniques, making reclassification time– and resource intensive (Le Bas, 1989; Le Bas and Streckeisen, 1991; Le Maitre et al., 2002; Mitchell and Bergman, 1991; Mitchell, 2020, 2021; Pearson et al., 2019; Tappe et al., 2005, 2022; Woolley et al., 1996). This is further complicated by the wide range of textures present in this type of rock and the prevalence of heteromorphism. Recent contributions have worked to identify chemical and mineralogical markers of tectonic or geodynamic setting for both of these melt types, leading to the general *(yet imperfect)* association of leucitites with subduction–related melts (Innocenzi et al., 2024; Lustrino and Wilson, 2007; Lustrino et al., 2019), and lamproites with orogenic or anorogenic (i.e. intraplate/cratonic) melting processes (Prelević et al., 2008a, 2010, 2012, 2013). This paper seeks to re-evaluate the EAPS in light of this more general association of melts with specific melting and mass transfer processes in well understood geodynamic settings.

The primary distinguishing feature between leucitites and lamproites is the presence of phlogopite mica in lamproites and its absence in leucitites (Table 4; Bergman, 1987; Mitchell and Bergman, 1991; Mitchell, 2020, 2021; Rock, 1991; Woolley et al., 1996). While the presence of other minerals such as leucite, olivine, and sanidine are shared between both rock types, the diversity and modal abundance of other mineral species occurring in lamproites is in itself characteristic (Table 4). The EAPS exhibits a similar diversity of minerals present in the rock to the range of minerals expected in lamproites, as well as poikolitic and phenocrystic phlogopite mica which are also expected in lamproites and not in leucitites (Figures 2a, b, and d–e; Tables 1 and 4). There are two major barriers to the entire EAPS being reclassified as lamproites. Firstly, as stated clearly in Woolley et al. (1996) several minerals preclude a rock from being included in the lamproite group. Specific feldspars (Na-rich alkali feldspar; plagioclase), foids (nepheline; kalsilite; sodalite; nosean; hauyne), and garnets (melanite; schorlomite; kimzsyite) as well as melilite and monticellite, should not occur as primary phases in lamproites but may occur in leucitites (Mitchell, 2020; Woolley et al., 1996). Nepheline occurs in both the samples reported on here and those of previous studies (*see petrography results section;* Figures 2c and e; Birch, 1976, 1978; Cundari, 1973). Nepheline is problematic being both silica saturated and sodic, however, this issue can be addressed in two ways. Lamproites are known to be highly heteromorphic, which in itself suggests that as the magma cools and crystallises it should be possible in rare cases, and the last stages of crystallisation, for nepheline to form. In the EAPS, nepheline appears rarely in only five of the 48 samples presented here. The second, and most important, consideration needed for the samples presented here is that nepheline is not primary to the mineralogy. It forms only in veins or melt pools interpreted to be last stages of crystallisation, and in melt veins directly in contact with xenoliths or other mantle cargo suggesting it is a reaction product; therefore not primary to the bulk magma. The second barrier, are the outcrops including and south from Griffith, i.e. from 34°S and southward (Figure 1d). These outcrops have all undergone some degree of alteration. In these samples analcime is more common than leucite and only olivine cores are preserved, with the remainder of the olivine having partially or fully transformed to iddingsite (Figures 2e). This includes the outcrop at Pine Lodge, in which no leucite is preserved (Figures 1b, e, and 2e; previously known as Cosgrove, for which the hotspot track is named). The observation of pseudoleucite or analcime should be treated with caution especially given the work of Prelević et al. (2004) who undertook analyses on a similar set of rocks to those analysed in this paper. Their work showed that transformation of leucite to analcime in a natural geological setting leads to falsification of K_2O/Na_2O and enrichment in some LILE and HFSE's during the transformation (e.g. Cs, Th, U), while also exhibiting depletion in others (e.g. K and Rb) (Prelević et al., 2004).

On a geochemical basis the EAPS rocks meet most of the discriminators to be lamproites as described by several studies (Table 4; Bergman, 1987; Foley et al., 1987; Prelević et al., 2008b; Woolley et al., 1996). The whole rock geochemistry (Figures 3–6) displays significant overlap with other lamproites globally (Figures 3a, c, 4b, c, e, f, 5a, d,e, and 6). Unlike other lamproites in Figure 6, there are no whole–rock end-member compositions in the EAPS in that our samples occasionally overlap the groups defined by Foley et al. (1987), although it should

Table 4. Summary of the mineralogical and geochemical criteria for leucitites and lamproites with comparison to the Eastern Australian Potassic Suite.

	Mineralogical Criteria [1,2]		Observed in
	Leucitite	Lamproite[a]	this study [6]
Plagioclase	○	⊗	⊗
Nepheline	○	⊗	⊗[b]
Leucite	●[c]	○	●
Diopside	●	○	●
Sanidine	○	○	○
Olivine	○[d]	○	●
Ti–Phlogopite	⊗	●[e]	●
Richterite	⊗	○	○
Enstatite	⊗	○	⊕
Apatite	⊗	○	○
Ilmenite	⊗	○	○
Perovskite	⊗	○	⊕
Mg–chromite(± Ti)	⊗	○	⊕
Mg–Ti–magnetite	⊗	○	⊕
Wadeite	⊗	○	⊕
Priderite	⊗	○	⊕
Carbonates	⊗	○[f]	○
Jeppite [g]	⊗	○	⊕
Armalcolite [g]	⊗	○	⊕
Scherbakovite [g]	⊗	○	⊕

	Geochemical Criteria [2,3,4,5]		Observed in
	Cratonic / Anorogenic [3,4]	Orogenic [2,3,5]	this study
Ultrapotassic [h]	>3	>3	0.22 – 5.15
Perpotassic [i]	>0.8 (commonly >1)		0.13 –0.93
Peralkaline [j]	>0.8 (commonly >1)		0.54 – 1.28
Mg# [k]	>70		55 – 76
FeO_T (wt%)	>10		8.92 – 11.87
CaO (Wt%)	>10	3 – 4	7.23 – 11.62
TiO_2 (Wt%)	1 – 7	<3	3.28 – 5.33
SiO_2 (Wt%)		48 – 60	40.66 – 50.92
K_2O (Wt%)		3 – 11	1.18 – 7.37
Al_2O_3 (Wt%)		8 – 14	7.25 – 10.50
Na_2O (Wt%)		0.5 – 4	0.71 – 3.95
	Trace elements:		
	Ba = >2000 – >5000		573 – 6940
	Sr = >1000 ppm		940 – 2824
	La = >200 ppm		57.24 – 213
	Zr = >500ppm		374 – 1010
		LREE enriched	LREE enriched
		Pb (∼55–150 ppm)	1.80 – 20.20

References: [1] Woolley et al. (1996); [2] Mitchell (2021); [3] Foley et al. (1987); [4] Mitchell and Bergman (1991); [5] Prelević et al. (2008a); [6] Lanati et al. (in prep.)

Key: ● = Always; ○ = Occasionally; ⊗ = Absent; ⊕ = Not observed

[a]: Several minerals detailed in the main text exclude a rock from the lamproite group when present as primary mineralogy (Mitchell, 2020, 2021; Woolley et al., 1996).

[b]: Nepheline is present in the EAPS, but only as a melt reaction product and therefore not primary. See main text for details.

[c]: In cases where leucite is greater than 90% of the rock the term Italite is used by Mitchell (2021).

[d]: Olivine is only noted as present when sanidine is absent from the rock

[e]: Includes madupitic phlogopites which are occasionally termed 'madupites' or will state 'madupitic' instead of denoting phlogopite in the name

[f]: Occurrence of carbonates was diagnostic of kimberlites and orangeites, but have also been observed in Kaapvaal lamproites (Pearson et al., 2019).

[g]: Generally not identifiable without microbeam techniques

[h]: Defined as molar K/Na ≥ 3

[i]: Defined as molar K/Al ≥ 1

[j]: Defined as molar (K+Na)/Al ≥ 1

[k]: Mg# = $100 \times [Mg/(Mg+Fe^{2+})]$

be stated that potassic magmas more likely span a continuum of melts rather than true 'end-members'. An example of this are samples 1402 (Wallaroy Hill), 1703 (Flagstaff Hill), and 0901a from the Byrock outcrop (Figure 1b–d) that are less lamproitic (i.e. variable MgO <9 wt% or >15 wt%; Mg# <65; or SiO_2 >46) compared to the other sub–samples from these outcrops despite being petrographically similar (Figures 3–6, and 9). This can be explained by the tendency for these samples to include significant olivine cargo, assumed to be xenocrystic, or by inclusion of altered xenoliths where olivine appears to have been replaced by near pure SiO_2 *(sample 17 only; potentially a result of interaction with a low–T CO_2–rich aqueous fluid (Austrheim et al., 2021))*. Similar to the mineralogical criteria, the outcrops south of 34°S that include Griffith, Pine Lodge, and Violet Town (Figure 1) deviate significantly from the broader grouping in most major element spaces (Figures 3–6). Most notably, the K contents of these samples (Figure 3b, c, and 5a) range from 1.18–1.41 wt% which is significantly lower than almost all of the other samples presented here. These samples also exhibit K_2O/Na_2O <0.5 while containing Na_2O of 2.54–3.95 wt% (Figure 3b and 5b), meaning they are not ultrapotassic. This is another hallmark of analcimitisation as described by Prelević et al. (2004). Ngwenya and Tappe (2021) elegantly dealt with the problem of analcimitisation by back correcting the K_2O and Na_2O contents of their rocks using concentration of these oxides in leucite and analcime. Using this methodology we can estimate the original character of the rock using our observations with the previously reported mineral modes and chemistry (Birch, 1978; Cundari, 1973), which returns K_2O: 3.33–4.04; Na_2O: 0.83–2.24; K_2O/Na_2O: 1.56–4.02. These recalculated values are heavily dependent on the accuracy of the modes and mineral chemistry previously reported but remain a reasonable maximum estimate (Ngwenya and Tappe, 2021). Critically, even with the full reconversion of analcime to leucite only Griffith and Pine Lodge would be considered ultrapotassic (K_2O/Na_2O: 3.21 and 4.02, respectively). However, even after recalculation the samples from the southern most volcano at Violet Town remain distinct with significantly higher Na_2O (1.54–2.24), and thus lower K_2O/Na_2O (1.56–2.31). These calculations were carried out for information purposes only and are not a valid counter argument for these samples to be included within the broader EAPS lamproite grouping.

Taken together, these characteristics show that the majority of the EAPS lavas are best characterised as lamproites both mineralogically and geochemically (Tables 1–4; Figures 2–6). The whole–rock chemistry shows an overlap between the EAPS and both orogenic and anorogenic lamproites, but there appears to be a stronger affinity towards the anorogenic grouping in the global lamproite dataset (Figures 3a, c, 4b, c, e, f, 5a, d,e, and 6; Casalini et al., 2022; Sarkar et al., 2025). Globally, lamproites occur alongside a range of magmatic compositions within the same broader field area (Mitchell, 2020), which means that the presence of analcime in the southern exposures should not impact viewing the EAPS as a suite of mostly lamproites. Furthermore, given their high–K affinity, these rocks are particularly susceptible to weathering and alteration by hydrous fluids (Gupta and Fyfe, 1975; Prelević et al., 2004; Roux and Hamilton, 1976). This does mean, however, that the outcrops south of 34°S included in this study cannot be classified on a petrographic or primary geochemical basis. Chemically they exhibit depletion in K and enrichment in Na (Figure 3b, c, and 5a, b), reflecting the analcimitisation of leucite. From the major elements, they cannot be definitively reclassified as lamproitic magmas, although the more incompatible whole–rock trace elements from Eu–Lu give some suggestion that they are chemically similar to the remainder of the EAPS (Figure 7). Previous Nd, Pb, and Sr isotopic work on the Pine Lodge sample provides evidence that this outcrop is more chemically linked to the Victorian Newer Volcanic Province (NVP) basalts than the lamproites, in agreement with previous petrological studies (Birch, 1978; Nelson et al., 1986). Our recommendation is that samples from Griffith (1801), Pine Lodge (2001), and Shepparton (Violet Town Quarry; 2101 – 2102) should not be considered lamproites or leucitites and that they should be treated with caution as they no longer possess the magmatic composition at the time of eruption. This is particularly relevant for Pine Lodge that sits between the EAPS and the NVP in chemical and petrological space. However, further work that includes modern isotopic analyses is needed to understand the genesis of the southern samples.

The holistic view of the EAPS data presented here reveals, based on trace element patterns and ratios, a clear demarcation between the northernmost outcrops at Byrock and El Capitan, and the fields further south at Tullibigeal, Lake Cargelligo, and Begargo Hill (Figures

1b–d, 7a, 12a–d, and 13a, b, and d). The separation between the trace element ratios of these samples (Figures 7a, 12b, d, and 13a, b, and d) suggests that a more extreme enrichment process was at play beneath the northernmost volcanoes. Furthermore, the northernmost samples consistently overlap with anorogenic lamproites more frequently than any other group of lavas (Figure 12a, b and 13a, b, and d). Therefore, we suggest that Byrock and El Capitan be considered as a separate volcanic field to the remainder of the EAPS. In the grouping proposed here, we term the northern outcrops the *Tindarey lamproites*, the central outcrops the *Tullibigeal lamproites*, both after the local geographic centre of the fields, while the southern outcrops of Griffith, Pine Lodge, and Violet Town remain unchanged.

Magma Sources and Geodynamic Environments of Eastern Australia

The generally accepted model for the formation, stabilisation and growth of the Australian continent begins with the formation of three Precambrian cratonic blocks in the Archean and Proterozoic, the West Australian Craton, South Australian Craton, and North Australian Craton (Fergusson and Henderson, 2015). Progressive accretion of orogenic belts then followed to form part of the Gondwana supercontinent through the Phanerozoic, which extended the continent eastward beginning with the accretion of the Delamarian and Thomson orogens in the Middle Cambrian to Ordovician (Figure 1a and b; Fergusson and Henderson, 2015; Glen, 2005). The accretion of the Delamarian and Thomson orogens overlaps with the formation of Lachlan orogen in the southeast which began in the Cambrian before accretion in the Middle Ordovician. The final stages of orogeny resulted in the accretion of the Mossman orogen on the northeast tip of Australia, on to modern day cratonic Australia (Figure 1a) during the Silurian and Devonian which occurred roughly syngenetically with the collision of the New England orogen in the Late Devonian to Early Carboniferous with the Thomson and Lachlan orogens in the central to southeast (Fergusson and Henderson, 2015; Glen, 2005). These five orogenic blocks are referred to collectively as the Tasmanides and make up modern–day eastern Australia (Figure 1a and b). They are all characterised by large-scale deformation and plutonic intrusion events as well as arc volcanism, which is best characterised by the heavily mineralised Macquarie Arc within the Lachlan Orogen (Fergusson and Henderson, 2015; Glen, 2005). Parts of the Tasmanides are also known to have undergone various rifting events most notably during the Cambrian (back–arc rifting) and then through the Mesozoic including the Permian and Triassic Sydney–Gunnedah–Bowen Basin system (Glen, 2005).

Once the consolidation of orogenic eastern Australia was complete intraplate volcanism became widespread, especially during the Cenozoic with some Oligocene but more commonly Neogene volcanism continuing into the Holocene making up the EAVP and the EAPS (Figure 1a–e; Blackburn et al., 1982; Cohen et al., 2008, 2013, 2017; Smith and Prescott, 1987; Wellman and McDougall, 1974). The source and mechanism that induced melting to generate these intraplate volcanics have been linked to several processes including mantle plumes (Cohen et al., 2008; Cundari et al., 1978; Davies et al., 2015; Johnson, 1989; McDougall and Wellman, 1976; Sutherland, 1983; Wellman and McDougall, 1974), edge–drive convection (EDC; Davies et al., 2015; Rawlinson et al., 2016, 2017), and more recently shear–driven upwelling (SDU; Duvernay et al., 2022; Manassero et al., 2024). The major difference between these processes is that for both EDC and SDU the primary control on melting and subsequent magmatism is the changing architecture of the lithospheric base where stress is focused (King and Anderson, 1995, 1998; O'Neill et al., 2005). In contrast, for a hypothesis invoking plumes melting and magmatism are assumed to be controlled by a large temperature difference between the plume and surrounding mantle, with the plume producing large volumes of melt below the LAB. Plate motion plays a significant role in all scenarios but the contribution to melt generation is inversely proportional. In the case of SDU and EDC, faster plate motions would result in greater volumes of mantle material being moved to higher levels and therefore induces larger degrees of melting. On the other hand, faster plate movement would reduce the time during which the plume head is in contact with the base of the lithosphere, making it more likely that melt production will be lower in any one place, hindering melt extraction.

Temperatures Under Eastern Australia

Some of the primary lines of evidence for plume–derived origins of age–progressive volcanism in Eastern Australia include elevated temperatures calculated by various methods. Most recently, Ball et al. (2021) used REE inverse modelling techniques to calculate temperatures of 1350 °C and melting depths of 50 km, or about 1.5 GPa, for the more abundant basalts of the EAVP. This model, however, explicitly excluded the EAPS lavas due to their enriched potassic composition. The temperatures modelled are elevated compared to the ambient mantle (∼1250 °C) and cannot be explained by normal adiabatic melting from the South Eastern Australian Geotherm (SEAG) as defined from xenoliths by O'Reilly and Griffin (1985) and reproduced by Griffin et al. (1987)(Figure 11b). All currently available whole–rock thermometers and barometers, regardless of the calculation method, are based on experiments on four–phase peridotites, or on basaltic glasses such as those erupted from shield volcanoes like Mauna Loa and Mauna Kea (Putirka, 2008). These compositions represent the bulk composition of the modern day mantle and include variations of four–phase peridotite to encompass compositions ranging from enriched to heavily depleted. Hydrous and non-peridotitic sources, as well as primitive heterogeneous mantle sources, present a significant challenge for these approaches in calculating an accurate melting temperature and depth. Anhydrous peridotites, for example, underpin the assumptions and model calibration used for thermometry by inverse REE modelling (Ball et al., 2021). In contrast to hydrous or metasomatised sources, anhydrous peridotites have significantly higher solidi (Figure 11b; Green, 2015) meaning the comparatively lower solidus of hydrous sources may result in overestimates of melting temperatures (e.g. Katz et al., 2003).

This is significant given that all of the samples in this study, despite having compositions within the calibrated chemical ranges for many thermometers and barometers, are most likely derived from heavily metasomatised and heterogeneous mantle sources known to persist beneath much of Eastern Australia (Frey and Green, 1974; Frey et al., 1978; Shea and Foley, 2019; Shea et al., 2022), making it difficult to determine the precise temperatures and pressure for the EAPS lavas.

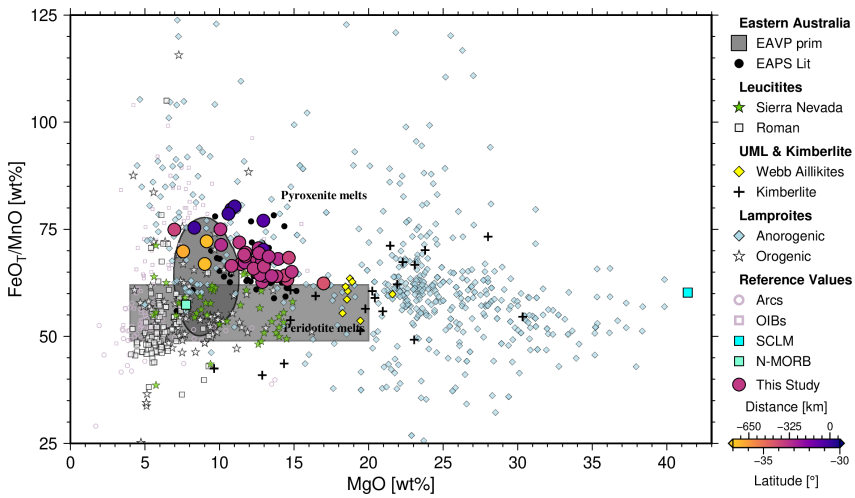

Fig. 9. FeO$_T$/MnO vs. MgO source component discrimination diagram with grey box showing the range of values for partial melts from an anhydrous peridotite source defined by Herzberg (2011). Melts outside this range are inferred to be generated by pyroxenite partial melts. EAVP prim point density polygon covers > 80% of all analyses. Data sources for published literature as in Figure 3; full references in the Supplement.

While many geothermobarometers exist, the most applicable of the available whole–rock thermometers and barometers for the EAPS are those calibrated on natural basaltic glass compositions or peridotite compositions from high–pressure and temperature experiments (Lee et al., 2009; Putirka, 2008). Putirka (2008) used Hawaiian basaltic glasses to derive both pressure–independent and pressure–dependent (Eq. 14 and 15 in Putirka (2008), respectively) thermometers. In contrast, Lee et al. (2009) used an approach including hydrous and anhydrous experimentally determined basaltic compositions, from mostly peridotite-like starting assemblages, to calibrate a combined thermometer and

barometer for volcanic compositions. Of these two options, the experimentally calibrated thermometer is believed to be the most robust, however use on metasomatised sources like those expected for alkali-rich melts is explicitly discouraged by the authors (Lee et al., 2009). In light of this, we apply the equations of Putirka (2008) to our samples, as it has the broadest compositional range of the available options. However, we first tested equations 14 and 15 by comparing calculated to experimental temperatures using the experimental melt compositions collated in Figure 10. Using both the pressure–independent and pressure–dependent thermometers there is good correlation between the calculated and experimental temperatures for melts derived from anhydrous peridotite, anhydrous pyroxenite, as well as carbonated peridotites, and mixed peridotite and pyroxenite sources which fall within the margin of error of the thermometer. However, for hydrous pyroxenite, anhydrous eclogites, and MARID sources the thermometer either over- or underestimates the calculated temperatures compared to the experimental temperatures. In the case of melts from experiments on anhydrous eclogite assemblages temperature estimates are lower by 200 °C due to low–MgO contents and low–Mg#, while for hydrous pyroxenites the range of calculated temperatures is larger and usually results in an overestimation of around +120 °C compared to the experimental temperature. Based on the closeness of our samples to hydrous pyroxenites (Figure 10), and the poor likelihood of volatile rich rocks being formed from the melting of an anhydrous eclogite with low–Mg#, we apply the predicted temperature offset for hydrous pyroxenites to the pressure–independent glass thermometer (*Eq. 14;* Putirka, 2008).

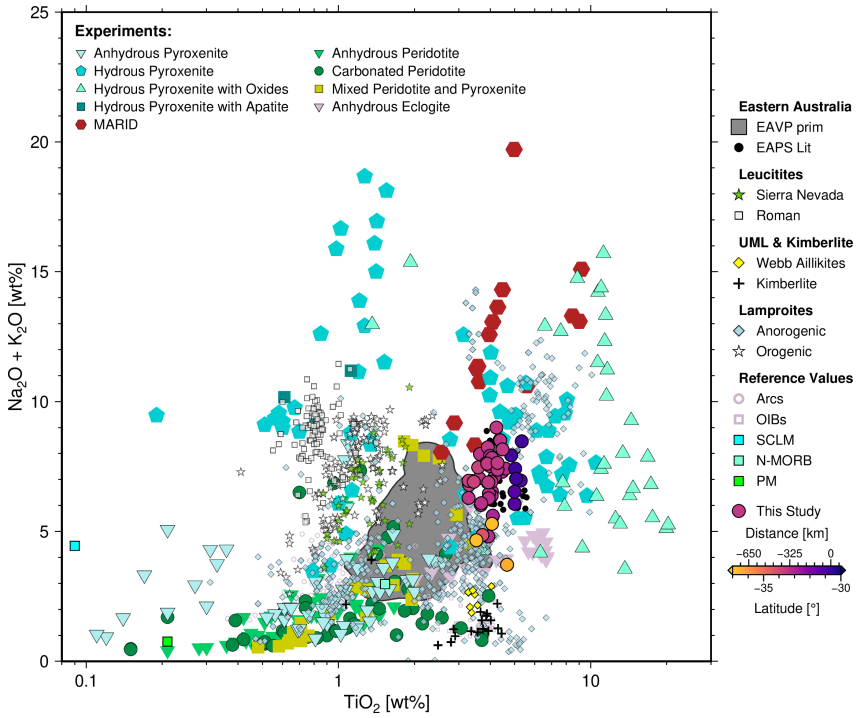

Fig. 10. Mantle source lithologies in (log-scale) TiO_2 versus total alkali (Na_2O + K_2O) from experimentally derived partial melt (inset legend); compilation after Shea et al. (2022). EAPS and comparison datasets included for context. EAVP prim point density polygon covers > 80% of all analyses. Data sources for published literature as in Figure 3; full references in the Supplement.

Applying this predicted temperature offset for hydrous pyroxenite melting to the EAPS samples the range of temperatures reduces from 1217–1490 °C to 1097–1370 °C with an average of 1244 °C (all ±50 °C; Figure 11a), which is roughly equivalent to the ambient mantle value (Ball et al., 2021; O'Reilly and Griffin, 1985). This suggests that even a small thermal perturbation would be sufficient to initiate melting. The EAPS could have been generated by normal adiabatic melting of a metasomatised source and, as a consequence, the invocation of a plume or hotspot is not necessary.

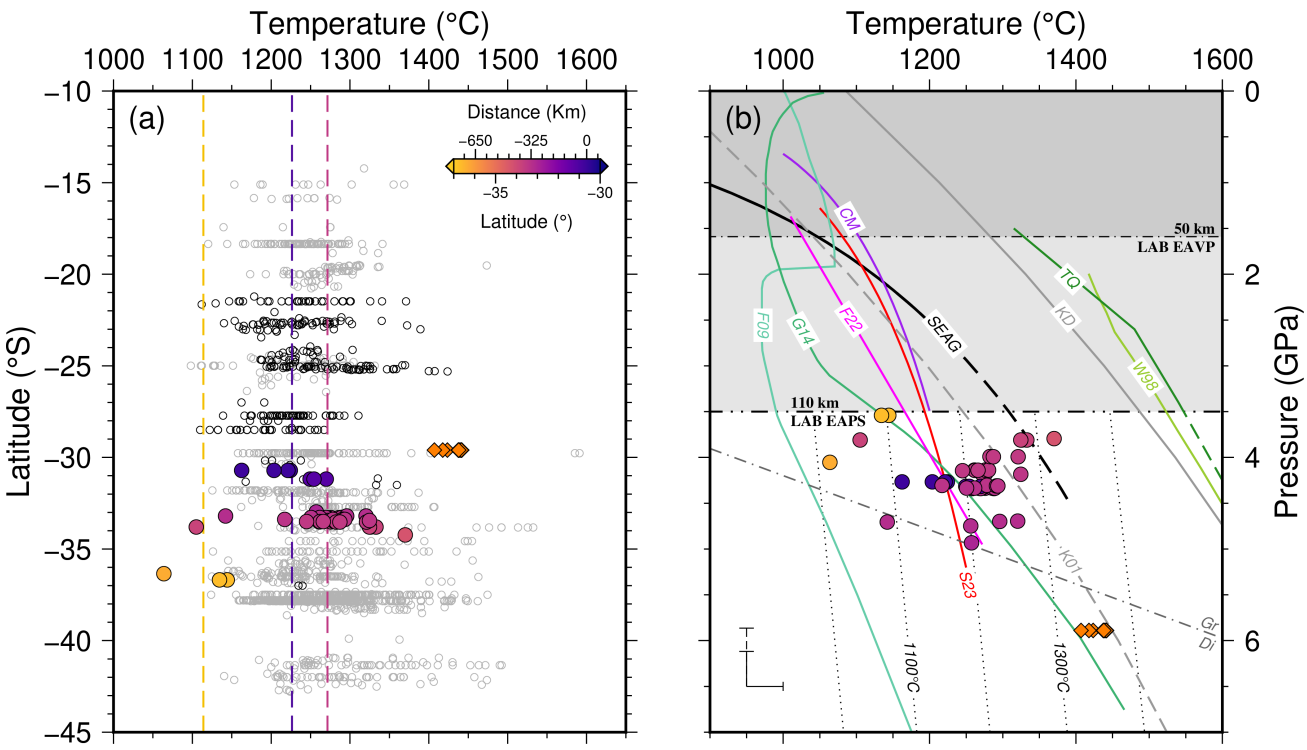

Fig. 11. Calculated temperatures vs latitude south (a) and depth (b) for the EAPS Lavas (colour scale in (a); orange diamonds = Bokhara River basanites). Dashed coloured lines in (a) show averages for north, central, and south EAPS; open black and grey circles represent age-progressive (plume related) and non-age-progressive EAVP basalts, respectively (full references in the Supplement; Shea et al., 2022). Pressure in (b) was converted from the LAB depths (Rawlinson et al., 2017) using a conversion factor of 32 km/GPa; a full description of conversion factor calculation can be found in the Supplement. Grey fields in (b) are the LAB depths beneath eastern Australia, while coloured lines are experimentally determined solidi for mantle assemblages compared with the SEAG (black solid and dashed line) and mantle adiabats (dotted lines below 3.5 GPa). Dark grey dot-dash line intercepting 6 GPa = graphite (Gr) to diamond (Di) stability line (Day, 2012). Reduced peridotite solidus below 2 GPa and dry pyroxenite (MIX1G) solidus roughly follow K01 and KD, respectively (Foley et al., 2009; Pintér et al., 2021; Kogiso et al., 2003). Dashed pressure error bar = EAPS, solid = EAVP (Rawlinson et al., 2017). Data sources: F09 = Foley et al. (2009) oxidised peridotite; G14 = Green et al. (2014) pyrolite +0.4 wt% H_2O; F22 = Foley et al. (2022) hydrous pyroxenite; S23 = Shu et al. (2024) phlogopite-websterite; CM = phlogopite lherzolite (Condamine and Médard, 2014; Condamine et al., 2016); K01 and KD = 0.1 wt% H_2O and dry lherzolite (Katz et al., 2003); TQ = Tinaquillo (depleted) lherzolite (Robinson et al., 1998; Robinson and Wood, 1998); W98 = KR43004 fertile lherzolite (Walter, 1998).

Metasomatism and Magma Generation

Anhydrous peridotite that makes up the bulk of the Earth's mantle cannot produce highly alkaline primary magmas (e.g Falloon and Green, 1988; Green, 2015; Hirose and Kushiro, 1993; Novella and Frost, 2014; Robinson et al., 1998; Robinson and Wood, 1998; Takahashi, 1986). Fertile lherzolites produce basanitic melt compositions when melting occurs at high–pressure or low melt fractions, which, compared to the overall EAPS, are still depleted (i.e. Falloon et al., 1997; Walter, 1998). Even when volatile components such as water and carbon, usually as H_2O and CO_2, are added these mantle assemblages still cannot replicate the range of primary magmas with elevated alkali element contents (Foley and Pintér, 2018; Green, 2015; Hirose, 1997; Novella and Frost, 2014; Pintér et al., 2021). Only melting of olivine–poor *(or free)* mantle rocks, such as pyroxenites, generates partial melts that are within the major element range of alkaline magmas (Foley et al., 2025; Hirschmann et al., 2003; Kogiso et al., 2003; Lambart et al., 2009, 2012, 2013; Pertermann and Hirschmann, 2003). The main challenges in producing alkaline melts from peridotite sources centre around generating sufficiently high K_2O, FeO_T, TiO_2, and Na_2O. Alkali deficiencies in experimental partial melts can only be addressed by increasing the alkali contents, usually K_2O, of the starting mixtures to represent metasomatised mantle assemblages that reflect natural xenoliths, sediment input, or be based on inferred compositions (Conceiçao and Green, 2004; Pintér et al., 2021, 2022; Wang and Foley, 2018). Subduction–related metasomes and fluids are the most common process investigated in experimental studies as sediments are a suitable source of alkalis and volatiles (Chen et al., 2021, 2023; Förster et al., 2019, 2021; Wang

et al., 2017, 2021, 2024). However, the source processes and exact type of metasomatic agents that can produce alkaline and potassic magmas in intraplate settings are not well constrained from experimental evidence.

Mantle metasomatism was proposed based on the observation of clear replacement textures in lherzolite nodules entrained in lavas of the West Eifel and South West Uganda (Hough, 1972; Lloyd and Bailey, 1975). These textures showed the "dissolution" of olivine, orthopyroxene and clinopyroxene within a spinel lherzolite that were replaced by mica and clinopyroxene (Lloyd and Bailey, 1975). Modern mantle metasomatism (hereafter 'metasomatism') represents a continuum of processes from fluid-rock through partial melting and melt-solid reactions (i.e. Dawson, 1984; Harte, 1983; O'Reilly and Griffin, 2013). Applying this to the EAPS lamproites it is, therefore, completely likely that the mantle beneath the EAPS has undergone several styles and generations of metasomatism to create a distinct mantle domain (metasome) that can produce such alkali enriched melts. This notion is supported by multiple xenolith and xenocryst studies from across the EAVP that have observed evidence of metasomatism across major, minor and trace element, and multiple radiogenic isotope systems (Alard et al., 2000, 2002; Andersen et al., 1984; Barron et al., 1996; Berkesi et al., 2019; Gaul et al., 2000, 2003; Griffin et al., 1984; Irving, 1974; Irving and Frey, 1984; Menzies and Wass, 1983; O'Reilly and Griffin, 1984; O'Reilly, 1987; O'Reilly and Griffin, 2000; O'Reilly et al., 2008; Pearson et al., 2006; Powell et al., 2004; Powell and O'Reilly, 2007; Robertson et al., 1985; Wass, 1979b,a; Wass and Rogers, 1980; Wass et al., 1980; Wilkinson, 1975; Wilkinson and Hensel, 1991; Yaxley et al., 1991, 1997; Zhang and O'Reilly, 1997; Zhang et al., 1999, 2001).

It has been argued that alkaline melts could be products of either magmatic fractionation or that their composition has been altered due to crustal assimilation. This implies that while these melts can be primary relative to their source, they would not be considered as parental or primitive (Foley and Pintér, 2018). We outline below that the EAPS melts are primitive in nature, match mantle values across many element systems, and thus are primary mantle melts (Figure 12a, b, d, and 13c). On a whole rock major element basis our samples pass the filters we applied to all published data used for comparison which we defined from previous studies that calibrated them on experimental melt compositions covering assemblages including anhydrous, hydrous, carbonated and mixed volatile sources as well as peridotite and fertile metasomatised mineralogies (*primary melt filter used: Mg number* $\geq$ *55,* $FeO_T \geq 6$ *wt%,* $MgO \geq 4$ *wt%, and* $SiO_2 < 60$ *wt%;* Prelević et al., 2008b; Shea et al., 2022). The Mg# of our samples, in particular, sits well above the *"primitive basalts"* of the EAVP defined by a recent large statistical analysis of East Australian volcanism (Figure 6c and 8c; Shea et al., 2022). Nb/U shows clearly that the EAPS plots completely within the mantle array and as Nb/U is especially sensitive to crustal inputs compared to other systems like Ce/Pb (EAPS = 17–35 $\approx$ mantle array; Hofmann et al., 1986), arguing strongly against the presence of any crustal component in the EAPS melts. Coupled P_2O_5/TiO_2 values ranging from 0.12–0.45, and Ti/Eu of roughly 4000–6500 (Figure 13a) trending toward primitive mantle values of 0.19 and 7600 respectively, also support a mantle origin. Furthermore, subduction-related processes such as arc-type melting, including contribution to the melt by slab–derived fluids, the melting of pelagic sediments, and fractionation can be ruled out using Th/Yb, La/Nb, Ba/La, Ba/Nb, and La concentrations (Figures 12b and 13b–d). This contrasts with some other lamproites globally; especially the orogenic lamproites that are the most likely to have elements added by interaction with slab fluids or melting of pelagic sediments (Figures 12b, 13b and c). Among the published data included for comparison, arc style melting is observed almost exclusively in the Sierra Nevada alkaline rocks and the Roman Province (Figures 12b, d and 13c). However, as observed from La–enrichment and Th/Yb against Nb/Yb, fractionation via fractional crystallisation is very important in the Roman Province (Figures 12b and 13d). While orogenic lamproites and the Sierra Nevada alkaline rocks also display enrichments in Th/Yb and Nb/Yb as well as La, the La contents show a less dramatic enrichment and are thus less conclusively impacted by fractional crystallisation (Figures 12b and 13d).

Another objective is to isolate the style and type of metasomatism that could create the EAPS melts. While the EAPS rocks exhibit primitive signatures and are mantle–derived they also exhibit a significant degree of enrichment characteristic for intraplate settings (Figure 12b). This enrichment is assumed to reflect the mantle assemblage from which these rocks melted (Figure 13b and d), and has been

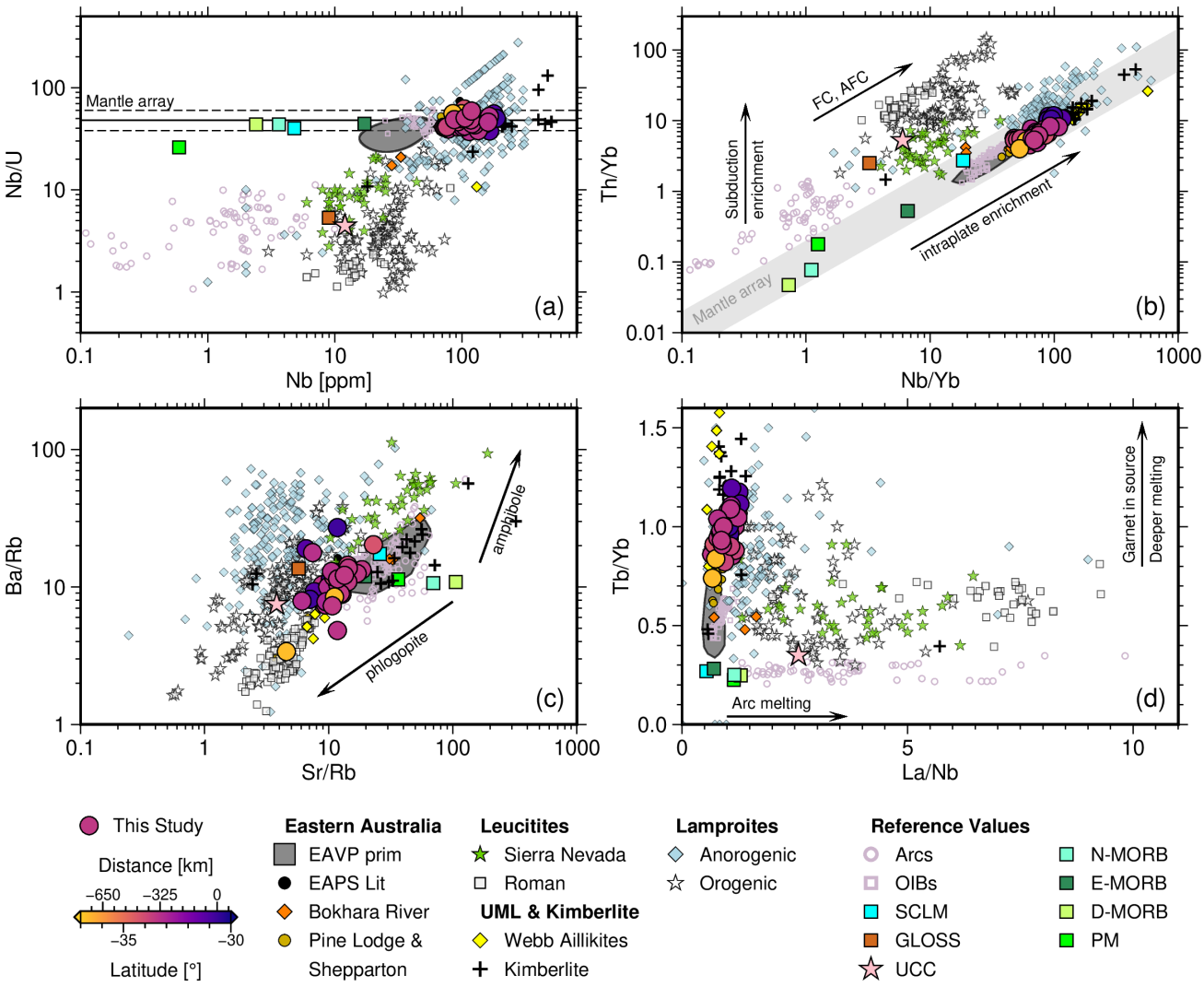

Fig. 12. Dominant mantle source trace element ratio discrimination plots of the EAPS showing **(a)** Nb vs. Nb/U indicating primitive-mantle derived magmas; Nb/U is sensitive to crustal contamination; mantle array from Hofmann et al. (1986). **(b)** Nb/Yb vs. Th/Yb showing mantle array and arrows illustrating subduction enrichment, assimilation and fractional crystallisation (FC, AFC), and intraplate enrichment after Ersoy et al. (2014) and Pearce (1983). **(c)** Sr/Rb vs. Ba/Rb with phlogopite- and amphibole-bearing source compositional vectors (arrows) after Furman and Graham (1999). **(d)** La/Nb vs. Tb/Yb with garnet and inferred source melt depth arrows, after Wang et al. (2002). Reference values: PM (Palme and O'Neill, 2013); MORBs (Gale et al., 2013); SCLM (McDonough, 1990); UCC (Rudnick and Gao, 2013); Arcs (Plank, 2005); OIBs (Willbold and Stracke, 2006); and GLOSS (Plank and Langmuir, 1998). EAVP prim point density polygon covers > 80% of all analyses. Data sources for published literature as in Figure 3; full references in the Supplement.

both conceptually and numerically modelled in early works on the EAVP (Frey and Green, 1974; Frey et al., 1978). In opposition to this, however, are the xenoliths sampled within Eastern Australia, including in rocks of the EAPS, that are relatively depleted assemblages such as lherzolites, harzburgites, and dunites. This stark contrast between the melts and xenoliths being erupted indicates that metasomatism, either via fluids or melt, must be widespread with a subset of these xenoliths providing clues to determine mechanisms of enrichment. Hydrous silicate minerals, as well as apatite and occasional sulfide minerals, are uncommon in the xenoliths of the EAVP; carbonates are never directly observed except as inclusions, although geochemical evidence of their presence in the mantle beneath eastern Australia has been extensively studied (Alard et al., 2000, 2002; Andersen et al., 1984; Barron et al., 1996; Berkesi et al., 2019; Irving, 1974; Irving and Frey, 1984; Menzies and Wass, 1983; O'Reilly and Griffin, 1984, 2000; Powell et al., 2004; Powell and O'Reilly, 2007; Robertson et al., 1985; Wass, 1979b,a; Wass and Rogers, 1980; Wass et al., 1980; Wilkinson, 1975; Wilkinson and Hensel, 1991; Yaxley et al., 1991, 1997). Carbonated peridotites have been shown experimentally to melt at lower temperatures than anhydrous peridotites (Figure 11b). At pressures equivalent

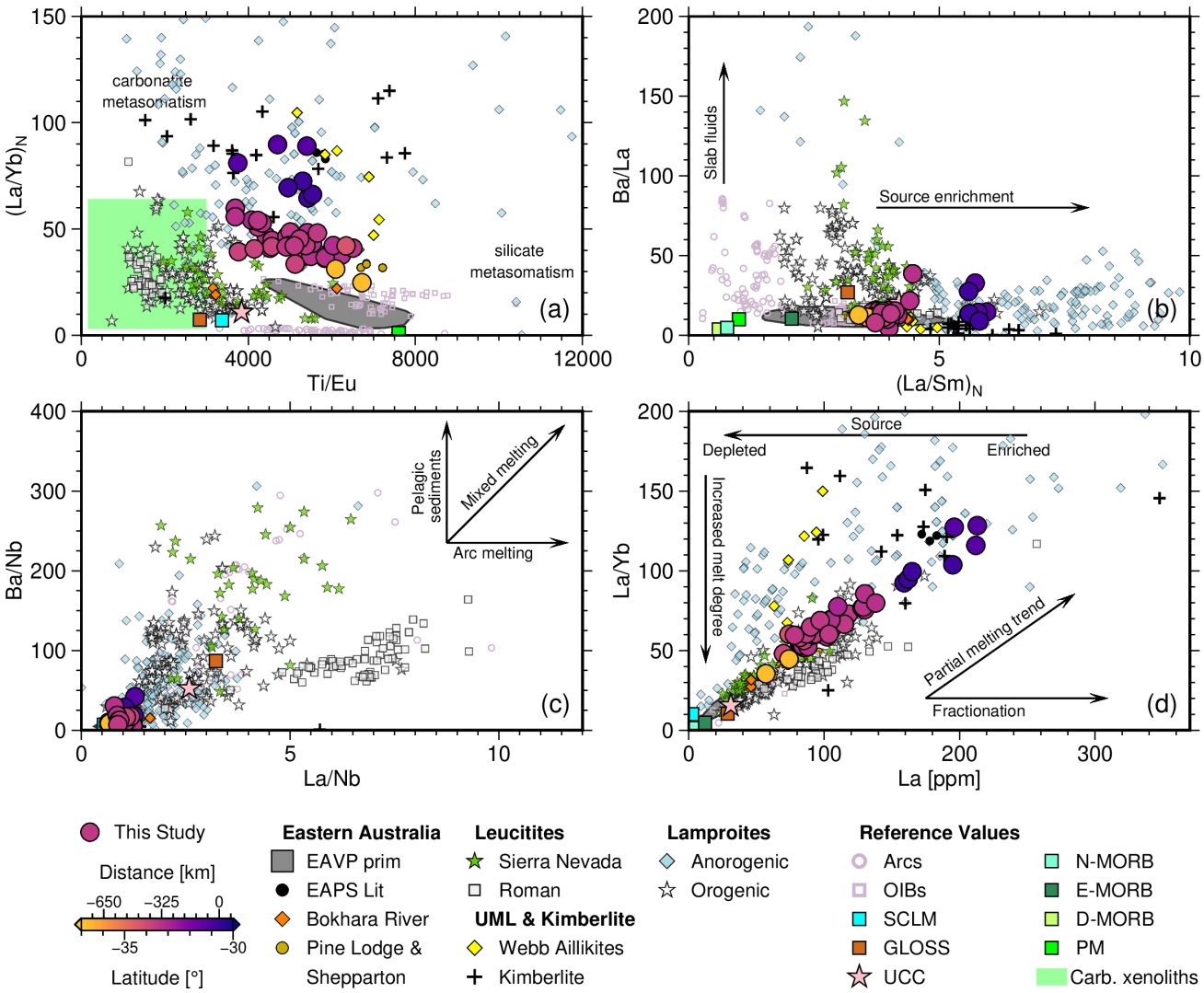

Fig. 13. Trace element ratio demarcation plots of the EAPS showing **(a)** Primitive mantle-normalised La/Yb vs. Ti/Eu displaying carbonatite and silicate metasomatism end-members compared to carbonatite metasomatised xenoliths (shaded green rectangle) from Yaxley et al. (1991); after Coltorti et al. (1999); Klemme et al. (1995); Rudnick et al. (1993). **(b)** Primitive mantle-normalised La/Sm, as an indicator of mantle source enrichment, versus Ba/La for identifying melts associated with subduction related slab fluids, after Aldanmaz et al. (2000) and Elliott et al. (1997). **(c)** La/Nb vs. Ba/Nb plotted with arrows showing general trends expected for melting with pelagic sediments, melts derived from mixed source, and arc-style melting. **(d)** La vs. La/Yb showing source enrichment, partial melt/ melt degree, and fractionation trends. Reference values: PM (Palme and O'Neill, 2013); MORBs (Gale et al., 2013); SCLM (McDonough, 1990); UCC (Rudnick and Gao, 2013); Arcs (Plank, 2005); OIBs (Willbold and Stracke, 2006); and GLOSS (Plank and Langmuir, 1998). EAVP prim point density polygon covers > 80% of all analyses. Data sources for published literature as in Figure 3; full references in the Supplement.

to the LAB of the EAPS incipient melting in this system can begin at around 1270 °C and persist for over 300 °C before major melting occurs regardless of if the assemblage is enriched or not, especially if water is also present (Dasgupta et al., 2007; Pintér et al., 2021). This makes melts derived from carbonated peridotites viable and potentially potent metasomatic agents that could contribute to geochemical and mineralogical changes in the mantle source, especially with melting temperatures at roughly ambient mantle. However, these are unlikely to be responsible for the enrichment in K (Figure 10), and reaction experiments between lamproite melts and peridotites have demonstrated that the lamproitic character of the primary melt is quickly lost on contact with the peridotite (Foley and Pertermann, 2021).

Similar to carbonates, hydrous phases such as phlogopite and amphibole can significantly reduce the solidus of peridotites even if the modal abundance of these phases is low. If amphibole is the dominant hydrous phase in the peridotite instead, melt compositions more closely resemble basanites and nephelinites (Condamine et al., 2022; Dasgupta et al., 2007; Dasgupta and Hirschmann, 2006; Green, 2015;

Pintér et al., 2021, 2022). Although the melting of peridotites enriched with either carbonates or hydrous silicate phases acting as a transient silicate–metasomatic agent could impart an enriched signature on an otherwise depleted lithospheric mantle, they alone are not capable of producing lamproitic melts like the EAPS (Figure 10). Instead the melts from this type of peridotite show a spectrum of compositions that range from highly silica undersaturated to more silicic melts and illustrate the enrichment of SiO_2 from carbonatite to basaltic magmatism (Condamine et al., 2022; Dasgupta and Hirschmann, 2006; Dasgupta et al., 2007; Foley and Pintér, 2018; Green, 2015; Pintér et al., 2021, 2022). Recent work on the Roman province using olivine hosted melt inclusions suggests multi-stage melt metasomatism could be a viable mechanism for K–enrichment in both leucitites and the less common orogenic lamproites of the province (Bracco Gartner et al., 2023, 2025). In the models presented by those authors to generate leucititic magmas the metasome, which is an olivine–free mica pyroxenite and not a peridotite, is first created by slab–derived fluids before being emplaced in veins within the crust and then remelted to generate the final heavily metasomatised magma (Bracco Gartner et al., 2023). The other study from these authors focuses on the generation of orogenic lamproites via melt–mixing of two magmas, both from likely melt metasomatised sources (Bracco Gartner et al., 2025). The first being a shoshonitic magma, proposed to be generated from the melting on a phlogopite–lherzolite, with an exceptionally enriched potassic magma (14 wt% K_2O) generated by the melting of an olivine–free mica pyroxenite ($Phl_{40}K$–$Rct_{25}Cpx_{35}$ ± Ap ±Ti-oxide), potentially created by melange melting, in an approximate 80:20 split (Bracco Gartner et al., 2025). As illustrated by these elegant yet complex models, single step melt metasomatism of peridotite fails to produce sufficient potassic sources and require additional ingredients usually from subduction processes. In contrast to melt metasomatism, fluid metasomatism is another possibility. This is likely to result in a highly transient geochemical signature due to the extremely reactive nature of immiscible fluids where only minor, if any, precipitates may remain as witness to any solid–liquid interaction (O'Reilly, 1987; O'Reilly and Griffin, 2013). Evidence for both fluid and melt–derived metasomatism has been reported in Eastern Australia (Andersen et al., 1984; Berkesi et al., 2019; Frey and Green, 1974; Frey et al., 1978; O'Reilly and Griffin, 1984; O'Reilly, 1987; O'Reilly and Griffin, 2000; Shea et al., 2022), as has carbonatite metasomatism (Frey and Green, 1974; Liu et al., 2021; Shea and Foley, 2019; Shea et al., 2022; Yaxley et al., 1997, 1998). Various geochemical indicators may be applied on the whole–rock basis to interrogate this including high Zr/Hf, where only carbonatites were shown to be able to elevate the ratio in basalts substantially above primitive mantle (EAPS = 37.64 – 52.87, Av. = 47.46; PM = 34.2; Dupuy et al., 1992; Furman and Graham, 1999; Palme and O'Neill, 2013; Rudnick et al., 1993). Primitive mantle normalised La/Yb coupled with Ti/Eu is used as a discriminator of silicate versus carbonatite metasomatism (Figure 13a), the EAPS and in particular the northern Tindarey lamproites plot above the broader EAVP including the fields shown to have carbonatite signatures (Coltorti et al., 1999; Klemme et al., 1995; Liu et al., 2021; Rudnick et al., 1993; Shea and Foley, 2019; Shea et al., 2022; Zinngrebe and Foley, 1995). They show similar enrichment in $(La/Yb)_N$ to other highly alkaline rocks like some anorogenic lamproites, including the West Kimberley lamproites, and aillikites (ultramafic lamprophyres) with silica contents 28–33 wt% (Sudholz et al., 2023). Compared to carbonated xenoliths from the southern portion of the EAVP, the EAPS lamproites span a similarly wide range of values but are more enriched in $(La/Yb)_N$ (Figure 13a). The Ti/Eu for the EAPS is not as low as in the carbonated xenoliths, or lavas from the Roman province, Sierra Nevada, and orogenic lamproites, which may be explained by the variability of Ti/Eu fractionation in carbonatites (Figure 13a; Foley et al., 2009). Low Ti/Eu has also been observed, coupled with high Ca/Sc, in eclogite xenoliths from the Kimberley region where the metasomatic agent was determined to be an alkali–rich silicate melt (Jacob et al., 2009; Rehfeldt et al., 2008). Experimental work on clinopyroxene partitioning between peridotite and carbonatite melt has shown that, assuming the residue of melting includes clinopyroxene, a low Ti/Eu signature is a valid indicator for carbonatite metasomatism (Klemme et al., 1995). Importantly, in systems where clinopyroxene is the dominant anhydrous phase, clinopyroxene both enters the melt and occurs in the residue (Edgar and Mitchell, 1997; Foley et al., 2022; Foley and Ezad, 2024; Foley et al., 2025; Funk and Luth, 2013; Konzett, 1997; Konzett et al., 1997; Lloyd et al., 1985; Luth, 1997; Shu et al., 2024, in revision; Sweeney et al., 1993). This would mean that when an assemblage with abundant clinopyroxene melts, and Ti is no

longer held back, it would still initially enter the melt and result in higher Ti/Eu giving a signature similar to silicate metasomatism even if a carbonatite was involved in the melt reaction.

The final open question to determine the source of the EAPS lamproites is, if not a four–phase peridotite then what could generate these melts and what components are needed? As stated above, olivine–poor assemblages have been shown to be capable of generating alkaline melts (Figure 9b). However many of these assemblages fail to impart sufficiently high K contents on the melt to explain lamproite genesis. The primary K–bearing minerals within the upper mantle are micas and amphiboles. Phlogopite and phengite micas will both persist at pressures up to ∼10 GPa, but more commonly 7–8 GPa (Domanik and Holloway, 2000; Foley, 1991; Harlow, 2003; Harlow and Davies, 2004; Luth, 1997; Schmidt, 1996; Sudo and Tatsumi, 1990). Amphibole occurring at shallower depths is calcic amphibole, and peridotitic xenoliths contain only pargasite. Calcic amphiboles do not contain significant K ($K_2O/Na_2O < 1$) and are not stable above 2.5–4 GPa (Aoki and Shiba, 1973; Berkesi et al., 2019; Dawson and Smith, 1973; Ghent et al., 2019; Ishimaru and Arai, 2008; Ito, 1986; Winterburn et al., 1990). Deeper in the mantle, K–richterite is the primary amphibole and its stability in the deep mantle has been recorded by xenolith occurrences in kimberlites and lamproites, and through experiments, which suggests K-richterite may be a viable source for some K-rich alkaline melts (Bergman, 1987; Erlank et al., 1987; Foley, 1991; Harlow and Davies, 2004; Konzett, 1997; Konzett et al., 1997; Konzett and Ulmer, 1999; Konzett and Fei, 2000; Mitchell, 1995; Mitchell and Bergman, 1991). Both K–richterite and phlogopite are stable on cold subduction geotherms, where K–richterite can outlast phlogopite well into the transition zone (up to 15 GPa) (Trønnes, 2002). Along warmer geotherms and at pressures greater than 6 GPa KK–richterite, the high–pressure variant of K–richterite with an $M4$ site containing K, Ca, or Na capable of hosting up to ∼12 wt% K_2O in its structure and almost no Na_2O, becomes stable and becomes more potassic as pressure increases (Harlow, 2003; Luth, 1997; Konzett and Fei, 2000; Konzett and Ulmer, 1999; Konzett et al., 1997; Konzett, 1997; Mandler and Grove, 2016). The enrichment of K_2O in lamproites, however, can simply be achieved through the melting of phlogopite in the source that can also explain the high modal abundance of phlogopite in these rocks (Table 1; Figure 2; Condamine and Médard, 2014; Foley, 1989, 1992a, 1993; Fritschle et al., 2013; Jaques et al., 1984; Mallik et al., 2015; Putirka et al., 2012; Wang et al., 2017).

This is best illustrated in Figure 12c where Ba/Rb and Sr/Rb are sensitive to amphibole and phlogopite given that Ba will preferentially partition into phlogopite but is extremely incompatible in amphibole (Adam et al., 1993; Adam and Green, 2006; Ezad and Foley, 2022; Foley and Ezad, 2024; LaTourrette et al., 1995). The behaviour of Rb more or less matches that of Ba in both minerals, albeit being slightly less compatible in phlogopite and slightly more compatible in amphibole (Foley and Ezad, 2024; LaTourrette et al., 1995). Conversely Sr is incompatible in phlogopite and moderately compatible to compatible in amphibole, depending on the assemblage, with calcic amphiboles exhibiting highest Sr compatibility (Adam et al., 1993; Adam and Green, 2006; Cannaò et al., 2022; Foley and Ezad, 2024; LaTourrette et al., 1995; Tiepolo et al., 2007). In instances where phlogopite is in equilibrium with the melt, Ba will be held back in residual phlogopite creating low–Ba/Rb (i.e. < 20) melts, while partial melts in equilibrium with amphibole will exhibit higher Ba contents initially, and high–Sr/Rb (i.e. > 20) as melting progresses to higher fractions (Furman and Graham, 1999). In this sense amphibole–bearing sources should plot above phlogopite–bearing sources in both Ba/Rb and Sr/Rb space (Figure 12c). Additionally given the incompatibility of both K and Na in the main peridotite minerals, with K being the more incompatible, the K_2O/Na_2O of the melt must reflect the collective K_2O/Na_2O of the alkali minerals in the source. The only amphibole observed in the EAPS is K–richterite, which commonly has a $K_2O/Na_2O \approx 1$, whereas the EAPS rocks range up to $K_2O/Na_2O \approx 8$ (Table 1; Figures 2a, b, and 3b). Integrating the geochemical evidence with geophysical interpretations of the approximate LAB depth beneath the EAPS from seismic tomography, all of the EAPS samples reported were probably generated between 113–158 km, or roughly 3.5–4.9 GPa (*depth to pressure conversion is provided in the supplement*; Figure 11b; Rawlinson et al., 2017). Both K–richterite and phlogopite would be stable, meaning all potassium and almost all water would be held by these phases but only melting of phlogopite could produce the K_2O/Na_2O observed in the EAPS.

Given the LAB depth beneath the EAPS it is almost certain that garnet, which becomes stable at pressures roughly above 2 GPa if sufficient Al_2O_3 is present, must have a place in the mantle source assemblage for the EAPS. Geochemical indicators for garnet mostly utilise the heavy rare earth elements (HREEs) like Yb, Tb, and Dy that range, in order, from strongly to marginally compatible. This behaviour, makes high $(La/Yb)_N$, Dy/Yb and Tb/Yb effective indicators of a garnet–bearing source, producing a steeply sloping trace element pattern towards the HREEs (Figure 7a), that when combined indicate the relative proportion of garnet (Figures 12d, 13a and d). Low Dy/Yb (i.e. <2; EAPS = 3.47–4.66) indicates a spinel–bearing source (Yang et al., 2007). Tb/Yb, in particular, is sensitive to garnet–bearing source assemblages because, unlike La/Yb that is influenced by degree of melting due to La incompatibility, both elements are compatible, allowing Tb/Yb to be used for both the proportion of residual garnet in the source and melting depth (Stracke and Bourdon, 2009; Turner et al., 2003; Wang et al., 2002). High Tb/Yb reflects melting at greater depths — a relationship we observe in the EAPS lavas with samples erupting through the thickest lithosphere displaying the highest Tb/Yb (Figure 12d; Wang et al., 2002).

FeO_T/MnO ratios show that the EAPS rocks have signatures consistent with a pyroxenite mantle source (Figure 9a). This is grounded in the principle that Mn is held back in the source by garnet, regardless of whether a peridotite or pyroxenite is the dominant assemblage. The lower solidus of a pyroxenite–dominated source compared to a similarly anhydrous peridotite requires significantly high melt fractions in order for garnet to actively melt (Herzberg, 2011). Iron will be readily liberated from the melting of clinopyroxene in this assemblage resulting in high FeO_T/MnO ratios (Herzberg, 2011). High CaO is a common feature of peridotite–derived melts due to the high solidus temperatures that result in clinopyroxene being the least stable phase in the assemblage (Herzberg and Asimow, 2008; Herzberg, 2011). Pyroxenite assemblages on the other hand are more likely to include clinopyroxene in the residue, leading to lower overall Ca contents in low-degree melts (Herzberg and Asimow, 2008; Herzberg, 2011). The discrimination line in CaO versus MgO space is shown in Figure 6b along with the EAPS samples, of which all but one sit within the pyroxenite–derived melts field. It should be noted there are a number of high-Ca pyroxenites that would plot above this line as detailed by Herzberg (2011), but in their system none of the peridotite partial melts will cross into the pyroxenite field, thereby making this a good discriminant for pyroxenite melting. Orthopyroxene is also likely to play a role in the source for the EAPS and is a good candidate to aid the high-MgO affinity within the suite while buffering the SiO_2 contents (Lee et al., 2009; Mallik et al., 2016). In order to generate the range of melt chemistry exhibited by the EAPS the source would need to have little or no olivine, significant pyroxene, and some garnet (Figures 6b, 9 and 10). Additionally, the high-Ti and potassic character of these melts necessitates the inclusion of phlogopite and a titanium–rich phase like rutile or ilmenite (Figure 10). As noted in Figure 4e the phosphorus content in the EAPS is elevated compared to the majority of the leucitites and EAVP basalts, which appears to be a feature of lamproites globally. Experiments on the melting of olivine–free hydrous pyroxenites with apatite support elevated P_2O_5 while further suggesting that where olivine is not formed incongruently apatite can contribute to the melt and still remain residual (Foley et al., 2022; Foley and Ezad, 2024). Applying this to our samples, the negative P anomaly in Figure 7a supports apatite playing a role in both the melting of the EAPS and being a remanent in the source. The presence of carbonate inclusions and carbonated glasses in the samples (Figure 2c and e; Lanati et al., in prep.) illustrates that the source is also carbonated, although whether this carbonation is a remnant of the metasomatic agent, inherent in the source, or acquired during ascent cannot be determined. Therefore the most likely source for the EAPS based on the chemistry presented here is a phlogopite–garnet–websterite with apatite ± Ti–oxides. While this specific lithology has not been directly sampled in the xenoliths of Eastern Australia, pyroxenites are not rare among the mantle cargo present in the alkali basalts of the EAVP and the NVP with many hosting some phlogopite, apatite, sulfides, or Ti–oxides (Andersen et al., 1984; Barron et al., 1996; Griffin et al., 1988; Irving, 1974; Irving and Frey, 1984; Menzies and Wass, 1983; O'Reilly and Griffin, 1984, 2000; Powell et al., 2004; Robertson et al., 1985; Wass, 1979b,a; Wass and Rogers, 1980; Wass et al., 1980; Wilkinson, 1975; Wilkinson and Hensel, 1991). Recent experiments by Shu et al. (2024, in revision) support our preferred source and align with the evidence from major and trace element indicators used in this study. In their work

Shu et al. (2024, in revision) show that the melting of an olivine–free phlogopite–garnet–websterite assemblage similar to the one we propose here results in a melt with increased MgO and SiO_2. However before orthopyroxene contributes to the melt both MgO and SiO_2 contents remain buffered in a range similar to the EAPS analyses, showing good agreement in the lamproite discrimination diagrams (Figure 6; Shu et al., 2024, in revision). Importantly, the experimental melts most applicable to the EAPS lavas occur at pressures of 3 and 4.5 GPa, and in the range of 1200–1300 °C for most major elements, except TiO_2 which mimics the EAPS from temperatures of 1350 °C (Shu et al., 2024, in revision). These conditions match the estimates of LAB depth as extracted from seismic tomography of roughly 3.5–4.9 GPa (113–158 km), as well as the temperature calculated here of 1244 °C (av; 1097–1370 °C) and ambient mantle beneath Eastern Australia (Figure 11).

Geodynamic Environment of Eastern Australia through time

Geochemistry and petrology alone cannot resolve the difference between hotspot volcanism and other geodynamic processes; however, they can elucidate processes of mantle source generation and magma production to reinforce arguments for a set of prevailing geodynamic conditions. Chemical and petrological discriminators can discern between processes such as various forms of partial melting, fractional crystallisation, or metasomatic processes such as fluid or melt infiltration. These processes are predominantly controlled by temperature and source composition, but may allow inferences to be drawn about the geodynamic environment.

Plume origin: The EAPS is commonly associated with the inferred Cosgrove hotspot track due to radiometric age progression data consistent with plate motion (Cohen et al., 2008, 2013; Davies et al., 2015; Sutherland, 1983; Wellman and McDougall, 1974). This association is not without controversy as the initial interpretations of age–progressive volcanism in the EAVP assigned different volcanic expressions to the plume track, creating a degree of inconsistency. The EAPS were among the fields variably included or excluded by studies tracking the motion of the Australian plate, with the evolving understanding of the Eastern Australian hotspot changing rapidly based on the authors' interpretation of age and spreading–rate vector projections (Sutherland, 1983). Further, no associated modern plume, in the form of a definitively recognisable thermal anomaly extending deeper than 110 km depth, has been observed in regional or global seismic tomographic models (Davies et al., 2015; Rawlinson et al., 2016, 2017). The Cosgrove plume head is currently believed to be situated beneath the Bass Strait between mainland Australia and Tasmania (Figure 1a and b), as determined by the projection of plate motion since the last related eruption (de Laat et al., 2023). Yet, only a small low–velocity zone beneath the Bass Strait off the south coast of Victoria is visible in global tomographic models between 80–110 km which has been suggested to be remnant melt from the now waned plume or a plume that has been captured by an existing edge-driven convection (EDC) cell (Figure 14a; Davies et al., 2015; de Laat et al., 2023; Rawlinson et al., 2016, 2017).

This is consistent with petrological evidence from magmatic flux estimates that potentially indicate a waning plume (Tapu et al., 2023). An investigation of slab-plume interactions between Australia and New Zealand using whole-mantle seismic tomography reports a "subslab hot upwelling", interpreted to be a connected whole mantle structure concentrating heat in the transition zone beneath the Bass Strait and the Newer Volcanic Province (Figure 1a and b; Toyokuni and Zhao, 2024). However, this upwelling deflects southward which is in contrast to the northward plate motion that would likely drag hot material to the north (Toyokuni and Zhao, 2024). The lack of a large-scale seismic anomaly consistent with plate motion, and therefore the inferred age-progressive volcanism, means that there is no consistent evidence for a singular deep mantle plume traversing to crustal levels and persisting today. Instead, seismic tomographic models are more consistent with smaller scale plume–like structures, or localised melts generated through another process like EDC or shear driven upwelling (SDU) which are primarily controlled by lithospheric architecture.

Importantly, even smaller scale plume–like structures (i.e. plumelets) require non-adiabatic temperature profiles and still mandate that an elevated temperature, relative to ambient mantle of 1250–1315 °C must be recorded to some degree in the final melt (Ball et al., 2021; Griffin et al., 1987; O'Reilly and Griffin, 1985). However, the average best-estimate temperature of 1244 °C (1097–1370 ± 50 °C) we have

calculated above is consistent with ambient mantle temperatures, and the generation of these melts at these temperatures therefore does not necessitate a plume or plumelet as a direct heat source.

Lateral mantle flow: An alternative geodynamic mechanism is melting induced by lateral flow of material from a plume that is offset from the volcanism. For Eastern Australia, the most likely source would be the Tasmantid plume which has been imaged as a larger scale seismic velocity anomaly in the Tasman Sea (south)east of the EAPS. However, several aspects make this scenario unlikely for melting in Eastern Australia. Firstly, the Tasmantid plume is roughly 1000 km to the east of the volcanoes sampled here yet the inferred buoyancy flux of the plume is too small to sustain lateral flow over these distances (Crossingham et al., 2017; Seton et al., 2019). Secondly, plate motion for the Australian plate is generally northward, which would cause the plume head and any associated lateral mantle flow to be pushed northward, leading to a decoupling of ages between the Tasmantid chain and the broader EAVP and EAPS, which is not the case (Cohen et al., 2013; Crossingham et al., 2017; Mather et al., 2020; McDougall and Wellman, 1976; Seton et al., 2019; Wellman and McDougall, 1974). Thirdly, the stepped nature of the east Australian LAB means that any lateral mantle flow would need to overcome a significant lithospheric keel of >50–100 km to reach the melt source region of the EAPS (Figure 14a–d). Only if the material displaced by a plume were to move significantly far enough westward and able to traverse either down and across the steps, or be caught in a channel within the lithosphere, then there would be a viable case for channelised melt flow style dynamics from the Tasmantid plume. A small remaining thermal anomaly would then be sufficient to trigger adiabatic or reactive melting of a previously metasomatised lithospheric mantle source of the EAPS, similar to EDC or SDU.

The primary lithosphere-asthenosphere boundary architecture in Eastern Australia not only steps progressively deeper east to west, but also steps progressively shallower north to south from roughly beneath the Byrock outrop of the Tindarey lamproites to the Newer Volcanic province (Figures 1 and 14). In addition, seismic tomography reveals a N–S trending lithospheric ridge coinciding with the locations of the EAPS (grey stars, Figure 14b–d). This creates a unique mantle channel of relatively shallow LAB depths bounded by the thicker lithosphere of cratonic Australia to the west and this ridge to the east. Coupled with plate motion, this LAB morphology would force the upward movement of mantle material; promoting decompression melting directly below the EAPS (Duvernay et al., 2021, 2022). The mechanisms dominating this style of channelised melt flow have been the focus of several recent geodynamic studies (Davies et al., 2015; Duvernay et al., 2021, 2022; Rawlinson et al., 2016, 2017). Through these processes the turbidity created by the deepest portions of the lithosphere passing over the underlying mantle sucks mantle material upward to fill the depressions behind these steps through shear driven upwelling (Figure 14i–ii). This then induces convecting cells at the edge of the lithospheric steps that couple with the shearing force of the material moving vertically to induce melting of the frozen metasomatised assemblages at the base of the lithosphere (Figure 14i-ii). Melts generated in this way can then either erupt directly or form chemically insulated veins within the lithosphere that aid later melt transport (Foley, 1992b). Another possibility is that these melts accumulate in pools that can fill the stepped depressions entirely or spill out and migrate further southward through the lithospheric channel to shallower steps acting as secondary metasomatic agents (Figure 14b–d). Due to the minimal temperature excess, melting would likely be most voluminous at the first establishment of this EDC-SDU system and cease in regions of thick lithosphere once enriched/refertilised lithologies have been depleted, which could lead to an apparent age progression. In this scenario, edge-driven convection and shear driven upwelling can explain both age-progressive and non-age progressive volcanism concurrently, while promoting the generation of melts at lower temperatures.

Carbon-rich metasomatic source – Subducted or Stored? It has been suggested that some of the melts within the EAVP have isotopic signatures (i.e. $^{87}Sr/^{86}Sr$, εNd, Pb) commonly associated with subduction related fluids and melts (Nelson et al., 1986; Nelson, 1992). The most recent subduction, during the accretion of the Macquarie Arc in the Lachlan fold belt, ceased ∼300 million years before the eruption of the EAPS (Fergusson and Henderson, 2015; Glen, 2005). Melting of carbonates accumulated in the transition zone has also

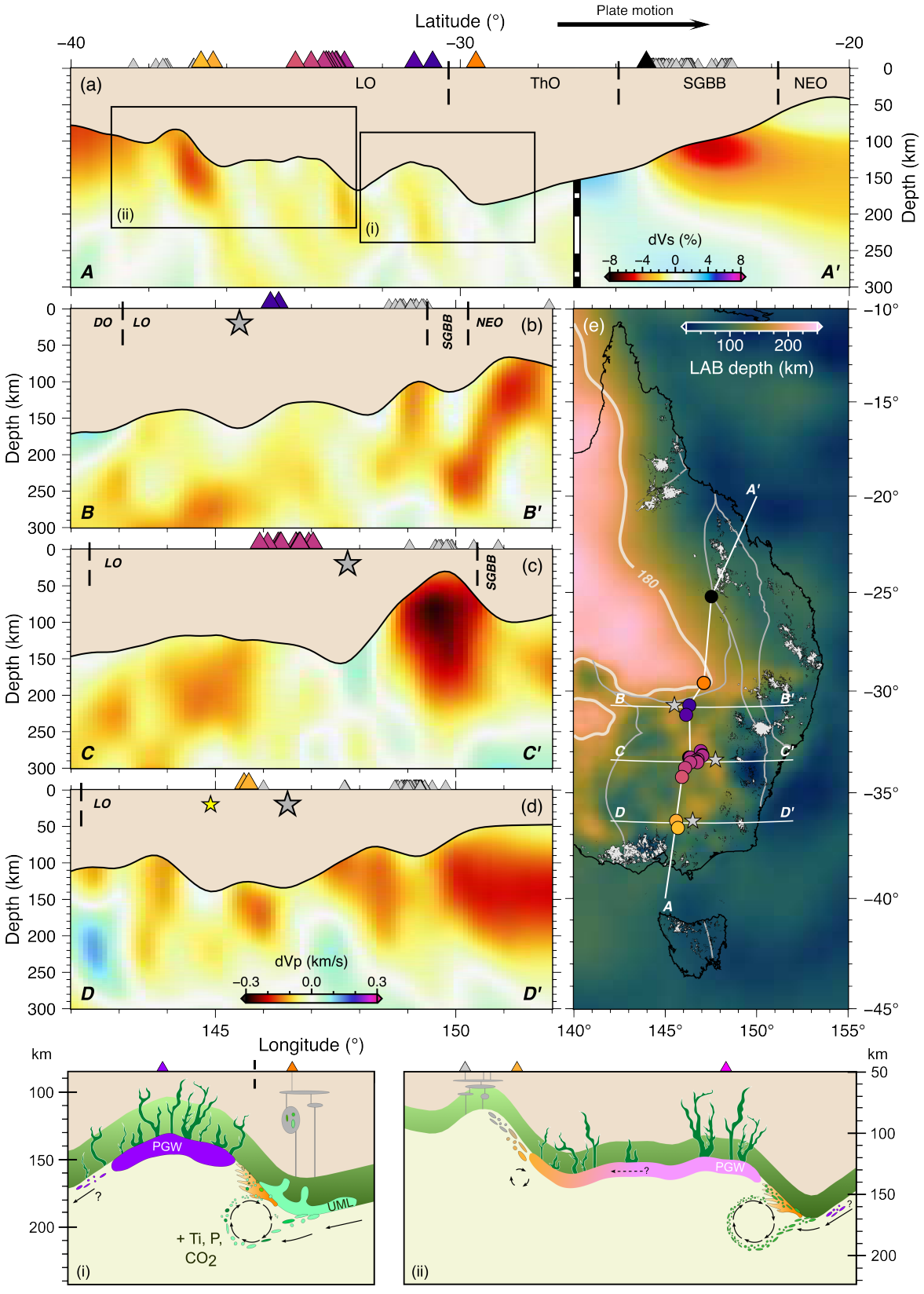

Fig. 14. (Caption next page.)

Fig. 14. LAB depth and seismic tomography profiles (a) along the Cosgrove track, (b) Byrock latitude, (c) through Lake Cargelligo and Tullibigeal, and (d) at Pine lodge with volcano locations projected on each transect. Transect location and direction are indicated in (e) along with the orogenic boundaries, volcanic fields of the EAVP (Shea et al., 2022), and 180 km LAB depth contour that roughly indicates the edge of cratonic Australia (Hoggard et al., 2020). Grey stars (b)–(e) show deepest LAB ridge position under each field noting the position relative to the volcano at the surface; yellow star in (d) shows isolated LAB ridge creating a melt channel beneath Pine Lodge. Insets show a schematic representation of the petro-geodynamic environment under Byrock (i), and Tullibigeal to Pine Lodge (ii). UML = ultra-mafic lamprophyre; PGW = phlogopite-garnet websterite; green gradient above LAB represents degree of metasomatism with cross-cutting veins providing a conduit for melt extraction; black arrows show direction of mantle flow relative to plate motion, and EDC cells. Plumbing systems (grey ellipses) beneath Bokhara River with xenoliths (i) and the Newer Volcanic Province (ii). In (a)–(d) the warm colours represent slow regions while cool colours show fast regions. Tomography sections beneath the EAPS in (a)–(d) come from high-resolution regional data by Rawlinson et al. (2017), while the section in (a) from -27° – -20° is lower resolution global data from de Laat et al. (2023). Volcano colours follow colour scales on geochemical plots (Tindarey = purple; Tullibigeal = pink; Shepparton = yellow), with the exception of Buckland (black) and the broader EAVP basalt (grey) volcanoes.

been suggested as a potential source of these signatures (Mather et al., 2020). As discussed above, our data suggests carbon is present in the source of the EAPS but isolating where that carbon originates is more challenging. Although some experimental work on subducted igneous crust has demonstrated that all carbon should be remobilised before reaching the transition zone (Thomson et al., 2016), this is an area of contention given much of the research has been done on mineralogically simple systems that create simplified melting reactions and phase stability fields. Drawing on the available experiments it is clear that this relationship will depend heavily on the assemblage and subduction geotherm. For example, experiments on a mix of 'dirty limestone' (i.e. natural limestone mixed with silicate sediment) show that carbonates infiltrated by chlorine-rich fluids can persist along colder geotherms and resist complete volatilisation (Chen et al., 2023). Even in the absence of significant chlorine, 'dirty limestone' assemblages can withstand melting at upper mantle conditions and may persist as a viable carbon reservoir in convergent margins (Chen et al., 2021). Similarly, higher pressure experiments indicate that the maximum upper stability limit for magnesite, and carbonates more broadly, is probably the very top of the lower mantle but would survive to the deep upper mantle (Libon et al., 2024; Thomson et al., 2014). Where hydrous-fluids are present several studies show the mobility of carbon increases, resulting in recycling rates that return only roughly one-third of subducted carbon to the surface (dependant on H_2O flux and depth; Farsang et al., 2021; Schmidt and Poli, 2003; Van Keken et al., 2011). However, as shown in Figures 12b, 13b, and c, none of the widely used whole–rock geochemical trace element ratios utilising fluid mobile (i.e. Ba) or sediment sourced (i.e. Ba, Th) elements support a definitive subduction, or subduction related aqueous fluid signature in the melts of the EAPS and EAVP. While a strong negative Pb anomaly often associated with fluid loss during subduction-driven magmatism is present in the EAVP basalts (Figure 7c) (Shea et al., 2022; Zhang et al., 2001), this is more or less absent from the EAPS lavas (Figure 7a).

Certainly the EAPS melts require carbon in the source as recorded in $(La/Yb)_N$ vs. Ti/Eu, high Zr/Hf ratios, and elevated CO_2 contents of the EAPS relative to other alkaline rocks (Figures 8d and 13a). A more likely source of carbon and subduction-like isotopic ratios than melting originating in the mantle transition zone could come from orogenic accretionary lithologies within the lithosphere. In the absence of a geologically contemporaneous carbon source, it becomes plausible that any carbon would have been introduced in metasomatic fluids or melts, produced by the melting of accreted lithospheric packages, and preserved as frozen melts like lamprophyres. This could include modified or partially devolatilised stored sediments locked in convergent margins, similar to those forming the Tasmanides, before being remelted and reacting with a peridotite to create an ultramafic lamprophyre (Figures 1b, 14a, e, and ii; Chen et al., 2021; Foley et al., 2009; Pintér et al., 2021). Carbon can exist within the mantle for geologically significant periods of time, evident from calculations of carbon recycling rates (e.g. Farsang et al., 2021), even under cratonic areas and contributes to a range of processes (Foley, 2008; Foley and Fischer, 2017; Foley et al., 2024; Wang et al., 2025). Geochemical evidence from mantle xenoliths and megacrysts reinforces the notion of significant carbon storage in the eastern Australian lithospheric mantle, even in the absence of physical measurements of carbon (Menzies and Wass, 1983; O'Reilly and Griffin, 1988; Robertson et al., 1985; Sutherland, 1996; Yaxley et al., 1991; Wass, 1979b; Wass and Rogers, 1980; Wass et al., 1980), including limited alluvial diamond occurrences of unknown origin *(that mostly predate Cenozoic volcanism)* (Barron et al., 2005; Davies et al., 2002; Griffin et al., 1998; Sutherland, 2003). The relative abundance of volatile elements in the EAPS lavas limits the range

of potential sources that could be mobilised to contribute to metasomatic change, and eventual melt generation to produce the chemistry observed (Figures 4e, 8a, and d). This would be most readily achieved if carbon, water, and phosphorus were stored in ultramafic sinks like redox frozen kimberlitic or lamprophyritic metasomes where hydrous minerals, apatite and carbonates (or diamond) are common crystallites (Barron et al., 1996, 2005; Foley et al., 2009; Foley, 2011; Irving and Frey, 1984; Menzies and Wass, 1983; O'Reilly and Griffin, 1988; Pintér et al., 2021, 2022; Rohrbach and Schmidt, 2011; Sutherland, 2003; Wass and Rogers, 1980; Wass et al., 1980). The probability of either metasome being the host for carbon and other volatile elements is primarily dependent on increased depth, or more precisely pressure, where kimberlites would be more stable at much deeper levels and higher pressure at or in excess of 160 km ($\approx$ 5 GPa) where diamond is likely to be stable (Giuliani et al., 2023; Jacob, 2004; Pintér et al., 2022; Veter et al., 2017). In Figure 13a the EAPS are plotted alongside the Mount Webb aillikites (Figure 1a; Sudholz et al., 2023) and likewise occupy the space between pure carbonatite and silicate metasomatism end–members, suggesting the metasomatic agent (or agents) may be intermediate between a silicic and carbonatitic character; a feature also observed recently in ultrapotassic rocks from northeastern China (Wang et al., 2025). Ultramafic lamprophyres and kimberlites encompass this space well, however an ultramafic lamprophyre is more viable as these agents tend to be more stable at shallower depths than kimberlites (Veter et al., 2017). LAB depths in Eastern Australia seldom exceed 150 km (Figure 1) which is roughly the source depth of the EAPS, and at these levels lamproitic compositions are suggested to be more sustainable than kimberlitic or lamprophyric melts (Veter et al., 2017). The similarity between the EAPS and the aillikites from Mount Webb as well as the elevated CO_2 contents of the EAPS relative to some lamproites and lamprophyres, despite having undergone degassing, reinforces that an ultramafic lamprophyre is a reasonable metasomatic agent for the EAPS source (Figures 8d and 13a). Based on the available evidence, this ultramafic lamprophyre required to metasomatise the source is most likely associated with the past melting of an accretionary sequence linked with the orogens of the Tasmanides, that was then stored before remelting.

Architectural control and extension: Incipient rifting has largely been neglected in the consideration of the geodynamic processes at play within the EAVP, and EAPS more specifically, with very few studies acknowledging the possibility of it having occurred (Berkesi et al., 2019; Johnson, 1989; Nelson et al., 1986; Sutherland and Barron, 2003). Nelson et al. (1986) and Nelson (1992) argue that the isotopic compositions of the EAPS are most similar to potassic and ultrapotassic rocks of the Bufumbira volcanics within the East African Rift; implying a link between source and process in the EAPS and EAR which may be linked to the age-progressive nature of both regions. During the orogenic accretion of the Tasmanides there is evidence of extensional cycles taking place between the majority of the major accretion events. The most well studied are the back–arc rifting observed in rocks from the Cambrian through to the Permian–Triassic with the formation of the Sydney–Gunnedah–Bowen basin that culminated in episodic shortening in the Mid-Permian (Figure 1b; Champion, 2016; Fergusson and Henderson, 2015; Glen, 2005). In the areas surrounding the EAPS eruptions dedicated structural geological studies are scarce primarily due to the thick regolith of predominantly Cenozoic sediments that often exceed 700 m thick. Deep seismic lines have been collected in the areas adjacent to Byrock (Figure 1c), specifically the Eromanga basin and Nelyambo trough, and to the south of Lake Cargelligo around Rankin Springs (Doublier et al., 2018; Glen et al., 2013; Kennett et al., 2016). The seismic lines carried out near Rankin Springs (i.e. roughly between Flagstaff Hill and Griffith; Figure 1d) show clear fault structures that are both shallow and steeply dipping, and occasionally extend to the surface (Kennett et al., 2016). Several rift basins are visible from a range of time periods. The clearest structures proximal to the EAPS are the horst and graben like features created by the Mount Jack fault and the Olepoloko fault (~50 km north of Byrock), and the flower structures of the Cobar Rift basin, ~160 km west of Byrock (Figure 1c; Doublier et al., 2018; Glen et al., 2013). The Olepoloko fault is one of the major faults in the region that extends from the surface to the Moho causing a ~9 km offset in Moho depth and marking the boundary between the Lachlan and Thompson orogens (Figure 1b; Doublier et al., 2018). The Cobar Rift basin is interpreted to be Devonian in age while the Olepoloko fault is Late- to Post-Devonian (Doublier et al., 2018). Unless these structures were later reactivated,

active extension in this area appears to have ceased in the Paleozoic, although it is noted by Glen et al. (2013) that the southern margin of the Thomson orogen appears to have remained a weak zone at least until the Triassic. Johnson (1989) also argued extensively for the potential role of thermal and tectonic uplift leading to rifting and emplacement the intraplate volcanics of the EAVP and EAPS noting the similarity to known rifts; for EAPS the most likely source of large–scale rifting identified would be reactivation of the orogenic margins. Some recent work, however, has suggested based on fluid inclusion analysis and petrogenesis of pargasite lherzolite xenoliths near McLean in the Mossman orogen (Figure 1a), that incipient rifting may have been occurring in that area as recently as ∼3 Ma (Berkesi et al., 2019).

The alkaline mafic character seen in the EAPS and broader EAVP, encompassing both the highly–alkaline, potassic, and more moderately alkali signatures, is comparable to volcanic rocks in well-defined rift systems such as the Rio Grande Rift (RGR), Labrador Sea Rift, and the East African Rift (EAR) (Gibson et al., 1993; Veter et al., 2017). Age progression is another similar characteristic as for both the RGR and EAR the unzipping of the rift results in clear age progressive magmatism (Ebinger et al., 2000; Klöcking et al., 2018; Williams, 1982). Finally, both in the EAVP and the EAR, the melts on the thickest portion of the lithosphere are sourced from the most heavily metasomatised portion of the underlying mantle (Rosenthal et al., 2009; Veter et al., 2017). Linking these together it becomes clearer that the strong architectural control exhibited within rift systems is analogous to the way stepped lithosphere in eastern Australia has been interpreted to induce adiabatic melting of the deepest and most enriched parts of the lithosphere to generate highly alkaline melts. In the absence of active crustal scale tectonic activity though, a more reasonable explanation for these characteristics is post-collisional relaxation leading to localised extension that may in turn trigger intraplate melting. A similar model has been evaluated in detail for the Eastern Mediterranean that shares many of the same geochemical features as the lavas presented here, including a north to south age-progression (Prelević et al., 2010, 2012, 2013). In their model Prelević et al. (2012) propose a multi-step formation sequence for the western Anatolian lamproites in the eastern Mediterranean that encompasses the ultra-depletion of the mantle before accretion to the lithosphere, then refertilisation by melting of sediments or crustal assemblages (i.e. orogenic delamination), and later upwelling of mantle through a tear in downgoing slabs to initiate melting of the overlying refertilised lithosphere. Elements of this model are supported by numerical models (e.g. Rey, 2001), and were also recently applied to the West Kimberley lamproites that like the EAPS are Cenozoic in age and exhibit large lithospheric steps coupled with an age-progression (Phillips et al., 2022). In the EAPS, several similarities can be drawn to this type of model with a few notable differences. The primary exception to the application of this model to Eastern Australia is the absence of any obvious slab remnant in the upper mantle. However, the lithospheric steps beneath Eastern Australia should essentially function in the same way by creating localised turbidity within the mantle allowing upwelling and decompression melting. Similarly to the Mediterranean occurrences, whole-rock HREE signatures of the EAPS suggest significant depletion is inherent in the source (Figure 7a). The EAPS melts also appear to have been enriched through interaction with a refertilised domain likely generated by the previous melting of an accretionary sequence to create a carbon-rich silicate melt similar to an ultra-mafic lamprophyre (Figures 12b, 13a, b, and d).

Therefore, mild extensional stresses due to post-collisional extension could have triggered melting of heavily metasomatised lithosphere, generating channels and deepening the steps in the lithosphere beneath the EAPS. In an intraplate setting absent of active subduction, this would be best characterised as a proto-rift style of magmatism that exploits refertilised conduits containing assemblages rich in hydrous minerals (Figures 12c, 14i, and ii), the occurrence of which beneath the EAPS is consistent with magnetotelluric modelling and the implementation of joint inversions of seismic and magnetotelluric data (Kirkby et al., 2020; Manassero et al., 2024). The heterogeneous and disparate nature of these hydrous zones, that likely contain modally high proportions of phlogopite, combined with expected low-volume melts would explain why volcanism is limited to a smaller population of volcanoes. Further, depletion of the source during melt extraction would make remelting more difficult and therefore limit the temporal scope of the volcanism, preventing the EAPS from advancing to a fractionated bimodal style which is present in the EAVP (Crossingham et al., 2018; Shea et al., 2022). The lack of modern and well–developed

rift structures coupled with a cessation of volcanism suggests that the extension has stalled, potentially in part due to the freezing of melt conduits and depletion of the mantle source. Nonetheless, a rift could develop in future if existing faults and melt conduits are reactivated and continue eroding the lithosphere base.

In summary, while the precise geodynamic conditions beneath the EAPS are unknown the evidence presented here provides broad constraints. Significant magmatic input from previous subduction is unlikely and any extension has not progressed past a "proto-rift" stage, indicating that post-collisional relaxation has occurred. In the absence of strong evidence for elevated mantle potential temperatures, the most plausible of the remaining options is a combination of edge-driven convection and shear-driven upwelling enhancing channelised melt flow from north to south with no plume input.

Conclusions

We propose that the outcrops formerly known as the NSW Leucitites are lamproites on both a mineralogical and chemical basis (Figures 2 and 6; Tables 1 and 4). We group these rocks together into the Eastern Australian Potassic Suite (EAPS). The two northernmost exposures of Byrock and El Capitan (Tindarey lamproites) display considerable heteromorphism and are chemically distinct from the remainder of the EAPS due to more significant trace element enrichment (Figures 1b, c, 7a, 12a–d, 13a, b, and d). The central portion of the suite (the Tullibigeal lamproites) are chemically and mineralogically similar to one another. Although the Tullibigeal lamproites are less enriched than the Tindarey lamproites, they are still potassic to ultrapotassic and display the characteristics of lamproites (Figures 1b, d, 12b, d, 13a, b, and d). Based on the published criteria both the Tindarey and Tullibigeal lamproites resemble cratonic or anorogenic lamproites more closely than orogenic lamproites, despite there being no known cratonic lithosphere in Eastern Australia. Weathering of outcrops south of 34°S has resulted in the alteration of leucite to create analcime, which masks or completely erases the potassic character of these rocks and we do not include them in the lamproite group at this time.

The source of the EAPS requires phlogopite with abundant pyroxene. Magmatic source depths in excess of 2 GPa are also necessary to ensure garnet is in the source, with the titanian affinity (TiO_2: 3.28–5.33 wt%) of the magmas inherited from oxide minerals (most likely rutile or titanite). Phosphorus and carbon in the source are likely present as apatite and carbonate minerals like magnesite or calcite which are reflected in the mineralogy of the samples as inclusions within phlogopite plates and carbonated melt pools (Figures 2c and e). We suggest that a phlogopite–garnet–websterite is the most likely source for the EAPS melting deeper than ~100 km. This source assemblage must have undergone metasomatism by a carbonatitic or ultramafic lamprophyric melt, likely prior to freezing and remelting, to impart a sufficiently phosphoric, carbonated and titanian mark on the final melt composition (P_2O_5: 0.65–1.80 wt%; Ti/Eu: 3692–6737; $(La/Yb)_N$: 24.88–89.66).

The temperatures recorded by our samples suggest low melting temperatures (av: 1244 °C) that are in line with ambient mantle beneath Eastern Australia (1250 °C); a geodynamic environment that lacks extreme heat anomalies (Figure 11). This negates a plume related genesis and reinforces a source prerequisite of a potassium-rich, likely hydrous or volatile bearing (i.e. carbonated/sulfidated), olivine-poor assemblage such as a mica-pyroxenite in the garnet stability field. This is further strengthened by the experiments of Shu et al. (2024, in revision) that generated EAPS-like melts from a similar assemblage. The geodynamic processes most likely to initiate melting in the lithospheric mantle beneath Eastern Australia are a combination of edge-driven convection and shear-driven upwelling with no plume input (Figure 14i and ii). The geodynamic conditions we propose for the generation of the EAPS lavas and their source are common in old stable continental regions with well–established architecture, similar to cratons. The chemistry of the EAPS supports a genesis whereby metasomatic episodes of volatile rich fluids or melts have sequentially fertilised the subcontinental lithosphere and lithospheric mantle of Eastern Australia (Figure

14i and ii). These episodes of metasomatism have aided in the destabilisation of the lithospheric mantle to the degree that deep channels have formed and enabled highly-enriched potassic magmatism mimicking the initial stages of rift related magmatism.

Data Availability

All original data collected and presented in this manuscript is available in Lanati and Shea (2025) at the DIGIS Geochemical Data Repository hosted by GFZ Data Services. Literature datasets that underwent filtering to make them comparable to the EAPS lavas are available as compiled or reference values (i.e. primitive mantle etc.) in the referenced papers included in the supplementary materials, or as precompiled files from the GEOROC database (**https://georoc.eu/**; versions 2023-12-01 or 2024-12-01).

Acknowledgments

The authors wish to acknowledge and pay our respects to the first nations people of Australia on whose lands the fieldwork and sample collection took place, the Wiradjuri, Wongaibon, Wailwan, and Yorta Yorta peoples. We would also like to thank the communities and landholders for hosting us and allowing us access to outcrops. Peter Weiland is thanked for his assistance and training with whole-rock XRF and trace-element geochemistry. Olivier Alard is thanked for assistance with the CHNS analyses, Luke Milan and the Lapidary laboratory at the University of New England are thanked for their expert petrographic slide preparation. We are also incredibly grateful to Maik Trogisch at the Institute für Mineralogie, University Münster, for his expert (and amazingly quick!) preparation of additional petrographic sections. Andreas Stracke, Felix Genske, and Mischa Böhnke are thanked for multiple constructive discussions around the robustness of metasomatised mantle source indicators and chemical geodynamics more broadly. Colour scale *"Plasma"* from Crameri (2018a) and Crameri (2018b) is used in this manuscript to prevent distortion of data and the exclusion of colour-vision impaired readers (Crameri et al., 2020); all figures have been checked in colour-vision impairment simulations to increase understandability and accessibility. The first author wishes to additionally acknowledge the highly collaborative and engaging environment provided by colleagues at the now defunct *Macquarie University Department of Earth and Planetary Sciences*, and *ARC Centre of Excellence for Core to Crust Fluid Systems*; several ideas and themes presented here could not have been developed without their influence and support. Finally, we wish to acknowledge the thoughtful and thorough reviews from Hayden Dalton, Lynton Jaques, Bruce Kjarsgaard, and Hugh O'Brien, which along with editorial handling from Sebastian Tappe significantly improved our manuscript.

Funding

Parts of this study were supported by a Geological Society of Australia – Victoria Division Postgraduate Grant, as well as a Macquarie University Postgraduate Research Fund award to AWL. SFF and JJS, and the broader study were supported by funding from an ARC Laureate Fellowship to SFF (FL180100134). JJS acknowledges funding from UKRI NERC grants NE/T012455/1 and NE/V011383/1. MK is supported by the German Research Foundation (DFG grant number KL3162/3-1; 503863705). AWL is funded by a Deutscher Akademischer Austauschdienst (German Research Exchange Service) Research Grant (Grant No. 57507869), and an Australian Government Research Training Program (RTP) Stipend and RTP Fee-Offset Scholarship through Macquarie University (Allocation No. 2018177). This work forms part of the first author's PhD thesis.

Author Contributions

AWL and JJS designed the study in consultation with SFF. AWL, JJS, and SFF undertook fieldwork. AWL and JJS undertook the sample preparation, and powder processing together. AWL completed the petrography, the majority of the whole rock geochemistry and CHNS

948 analyses, completed all data processing, produced the figures, and wrote the initial manuscript. JJS provided multiple edits to the manuscript
949 and helped streamline discussion points, especially around consistency with the literature of East Australian Volcanism. MK assisted with
950 data compilation, figure making and design, and provided significant input for the discussion. AR provided detailed feedback on figures and
951 several parts of the discussion. SFF, SK, and AR edited the manuscript, acquired funding and supervised this project. This project is part
952 of the broader Eastern Australian Volcanism project within the Earth Evolution group at Macquarie University led by SFF, of which the
953 first authors PhD project is a part. All authors have read and contributed to the reviewing and editing of the final manuscript.

References

Adam, J., Green, T., 2006. Trace element partitioning between mica- and amphibole-bearing garnet lherzolite and hydrous basanitic melt: 1. Experimental results and the investigation of controls on partitioning behaviour. Contributions to Mineralogy and Petrology 152, 1–17. doi:10.1007/s00410-006-0085-4.

Adam, J., Green, T.H., Sie, S.H., 1993. Proton microprobe determined partitioning of Rb, Sr, Ba, Y, Zr, Nb and Ta between experimentally produced amphiboles and silicate melts with variable F content. Chemical Geology 109, 29–49. doi:10.1016/0009-2541(93)90060-V.

Alard, O., Griffin, W.L., Lorand, J.P., Jackson, S.E., O'Reilly, S.Y., 2000. Non-chondritic distribution of the highly siderophile elements in mantle sulphides. Nature 407, 891–894. doi:10.1038/35038049.

Alard, O., Griffin, W.L., Pearson, N.J., Lorand, J.P., O'Reilly, S.Y., 2002. New insights into the Re-Os systematics of sub-continental lithospheric mantle from in situ analysis of sulphides. Earth and Planetary Science Letters 203, 651–663. doi:10.1016/S0012-821X(02)00799-9.

Alard, O., Halimulati, A., Gorojovsky, L., Wieland, P., 2022. Sulfur Mass Fractions in Thirty-Seven Geological Reference Materials by Titration, XRF and Elemental Analyser . Geostandards and Geoanalytical Research , 1–20doi:10.1111/ggr.12473.

Aldanmaz, E., Pearce, J.A., Thirlwall, M.F., Mitchell, J.G., 2000. Petrogenetic evolution of late Cenozoic, post-collision volcanism in western Anatolia, Turkey. Journal of Volcanology and Geothermal Research 102, 67–95. doi:10.1016/S0377-0273(00)00182-7.

Ananuer, H., Alard, O., in prep. C and h concentrations in 32 geo-reference materials measured by elemental and simultaneous thermal analysers.

Andersen, T., O'Reilly, S.Y., Griffin, W.L., 1984. The trapped fluid phase in upper mantle xenoliths from Victoria, Australia: implications for mantle metasomatism. Contributions to Mineralogy and Petrology 88, 72–85. doi:10.1007/BF00371413.

Aoki, K.I., Shiba, I., 1973. Pargasites in lherzolite and websterite inclusions from itinome-gata, Japan. The Journal of the Japanese Association of Mineralogists, Petrologists and Economic Geologists 68, 303–310. URL: http://www.jstage.jst.go.jp/article/ganko1941/68/10/68_10_303/_article, doi:10.2465/ganko1941.68.303.

Austrheim, H., Corfu, F., Renggli, C.J., 2021. From peridotite to fuchsite bearing quartzite via carbonation and weathering: with implications for the Pb budget of continental crust. Contributions to Mineralogy and Petrology 176, 1–14. URL: https://doi.org/10.1007/s00410-021-01851-z, doi:10.1007/s00410-021-01851-z.

Ball, P.W., Czarnota, K., White, N.J., Klöcking, M., Davies, D.R., 2021. Thermal Structure of Eastern Australia's Upper Mantle and Its Relationship to Cenozoic Volcanic Activity and Dynamic Topography. Geochemistry, Geophysics, Geosystems 22, 1–31. doi:10.1029/2021gc009717.

Barron, B.J., Barron, L.M., Duncan, G., 2005. Eclogitic and ultrahigh-pressure crustal garnets and their relationship to Phanerozoic subduction diamonds, Bingara Area, New England fold belt, Eastern Australia. Economic Geology 100, 1565–1582. doi:10.2113/gsecongeo.100.8.1565.

Barron, B.J., Sutherland, F.L., Robertson, A.D., 1996. Olivine 'leucitites', their xenolith and megacryst suites, Hoskings Peaks, north Queensland. Australian Journal of Earth Sciences 43, 231–244. URL: http://www.tandfonline.com/doi/abs/10.1080/08120099608728251, doi:10.1080/08120099608728251.

Bergman, S.C., 1987. Lamproites and other potassium-rich igneous rocks: A review of their occurrence, mineralogy and geochemistry. Geological Society Special Publication 30, 103–190. doi:10.1144/GSL.SP.1987.030.01.08.

Berkesi, M., Czuppon, G., Szabó, C., Kovács, I., Ferrero, S., Boiron, M.C., Peiffert, C., 2019. Pargasite in fluid inclusions of mantle xenoliths from northeast Australia (Mt. Quincan): evidence of interaction with asthenospheric fluid. Chemical Geology 508, 182–196.

doi:10.1016/j.chemgeo.2018.06.022.

Birch, W.D., 1976. Mineralogical note the occurrence of a leucite-bearing lava at cosgrove, Victoria. Journal of the Geological Society of Australia 23, 435–437. doi:10.1080/00167617608728957.

Birch, W.D., 1978. Mineralogy and geochemistry of the leucitite at cosgrove, Victoria. Journal of the Geological Society of Australia 25, 369–385. doi:10.1080/00167617808729047.

Birch, W.D., 1980. Mineralogy of vesicles in an olivine leucitite at Cosgrove, Victoria, Australia. Mineralogical Magazine 43, 597–603. doi:10.1180/minmag.1980.043.329.06.

Blackburn, G., Allison, G., Leaney, F., 1982. Further evidence on the age of tuff at Mt Gambier, South Australia. Transactions of the Royal Society of South Australia 106, 163–167.

Bracco Gartner, A.J., Nikogosian, I.K., Davies, G.R., Koornneef, J.M., 2023. The multi-component mantle source of Roman province ultrapotassic magmas revealed by melt inclusions. Geochimica et Cosmochimica Acta 355, 266–281. doi:10.1016/j.gca.2023.06.012.

Bracco Gartner, A.J.J., Nikogosian, I.K., Aartsen, J.M., Karlas, E.L., Davies, G.R., Koornneef, J.M., 2025. Orogenic lamproites from Italy formed by mixing of highly potassic and shoshonitic melts. Earth and Planetary Science Letters 654, 119228. URL: https://linkinghub.elsevier.com/retrieve/pii/S0012821X25000275, doi:10.1016/j.epsl.2025.119228.

Browne, W.R., 1933. Presidential address. An account of post-Palæozoic igneous activity in N.S.W. Journal and proceedings of the Royal Society of New South Wales 67, 1–95. URL: https://www.biodiversitylibrary.org/part/360074, doi:10.5962/p.360074.

Cannaò, E., Tiepolo, M., Borghini, G., Langone, A., Fumagalli, P., 2022. The influence of oxygen fugacity and chlorine on amphibole-liquid trace element partitioning at upper-mantle conditions. European Journal of Mineralogy 34, 35–57. doi:10.5194/ejm-34-35-2022.

Casalini, M., Avanzinelli, R., Tommasini, S., Natali, C., Bianchini, G., Prelević, D., Mattei, M., Conticelli, S., 2022. Petrogenesis of Mediterranean lamproites and associated rocks: The role of overprinted metasomatic events in the post-collisional lithospheric upper mantle. Geological Society Special Publication 513, 271–296. doi:10.1144/SP513-2021-36.

Champion, D., 2016. Geodynamic Synthesis of the Phanerozoic of eastern Australia. Second Edition. Record 2016/007. 2009. URL: http://www.ga.gov.au/metadata-gateway/metadata/record/90096/.

Chen, C., Förster, M.W., Foley, S.F., Liu, Y., 2021. Massive carbon storage in convergent margins initiated by subduction of limestone. Nature Communications 12. URL: http://dx.doi.org/10.1038/s41467-021-24750-0, doi:10.1038/s41467-021-24750-0.

Chen, C., Förster, M.W., Foley, S.F., Shcheka, S.S., 2023. Carbonate-rich crust subduction drives the deep carbon and chlorine cycles. Nature 620, 576–581. doi:10.1038/s41586-023-06211-4.

Cohen, B.E., Knesel, K.M., Vasconcelos, P.M., Schellart, W.P., 2013. Tracking the Australian plate motion through the Cenozoic: Constraints from 40Ar/39Ar geochronology. Tectonics 32, 1371–1383. doi:10.1002/tect.20084.

Cohen, B.E., Knesel, K.M., Vasconcelos, P.M., Thiede, D.S., Hergt, J.M., 2008. 40Ar/39Ar constraints on the timing and origin of Miocene leucitite volcanism in southeastern Australia. Australian Journal of Earth Sciences 55, 407–418. doi:10.1080/08120090701769514.

Cohen, B.E., Mark, D.F., Fallon, S.J., Stephenson, P.J., 2017. Holocene-Neogene volcanism in northeastern Australia: Chronology and eruption history. Quaternary Geochronology 39, 79–91. URL: http://dx.doi.org/10.1016/j.quageo.2017.01.003, doi:10.1016/j.quageo.2017.01.003.

Coltorti, M., Bonadiman, C., Hinton, R.W., Siena, F., Upton, B.G., 1999. Carbonatite metasomatism of the oceanic upper mantle: Evidence from clinopyroxenes and glasses in ultramafic xenoliths of Grande Comore, Indian Ocean. Journal of Petrology 40, 133–165. doi:10.1093/petroj/40.1.133.

Conceiçao, R.V., Green, D.H., 2004. Derivation of potassic (shoshonitic) magmas by decompression melting of phlogopite+pargasite lherzolite. Lithos 72, 209–229. doi:10.1016/j.lithos.2003.09.003.

Condamine, P., Couzinié, S., Fabbrizio, A., Devidal, J.L., Médard, E., 2022. Trace element partitioning during incipient melting of phlogopite-peridotite in the spinel and garnet stability fields. Geochimica et Cosmochimica Acta 327, 53–78. doi:10.1016/j.gca.2022.04.011.

Condamine, P., Médard, E., 2014. Experimental melting of phlogopite-bearing mantle at 1 GPa: Implications for potassic magmatism. Earth and Planetary Science Letters 397, 80–92. URL: http://dx.doi.org/10.1016/j.epsl.2014.04.027, doi:10.1016/j.epsl.2014.04.027.

Condamine, P., Médard, E., Devidal, J.L., 2016. Experimental melting of phlogopite-peridotite in the garnet stability field. Contributions to Mineralogy and Petrology 171, 1–26. doi:10.1007/s00410-016-1306-0.

Crameri, F., 2018a. Geodynamic diagnostics, scientific visualisation and StagLab 3.0. Geoscientific Model Development 11, 2541–2562. doi:10.5194/gmd-11-2541-2018.

Crameri, F., 2018b. Scientific colour maps. doi:10.5281/zenodo.1243862.

Crameri, F., Shephard, G.E., Heron, P.J., 2020. The misuse of colour in science communication. Nature Communications 11, 5444. URL: https://doi.org/10.1038/s41467-020-19160-7, doi:10.1038/s41467-020-19160-7.

Crossingham, T.J., Ubide, T., Vasconcelos, P.M., Mallmann, G., 2018. Parallel plumbing systems feeding a pair of coeval volcanoes in Eastern Australia. Journal of Petrology 59, 1035–1066. doi:10.1093/petrology/egy054.

Crossingham, T.J., Vasconcelos, P.M., Cunningham, T., Knesel, K.M., 2017. 40Ar/39Ar geochronology and volume estimates of the Tasmantid Seamounts: Support for a change in the motion of the Australian plate. Journal of Volcanology and Geothermal Research 343, 95–108. URL: http://dx.doi.org/10.1016/j.jvolgeores.2017.06.014, doi:10.1016/j.jvolgeores.2017.06.014.

Cundari, A., 1973. Petrology of the leucite-bearing lavas in New South Wales. Journal of the Geological Society of Australia 20, 466–492. URL: http://www.tandfonline.com/doi/abs/10.1080/00167617308728829, doi:10.1080/00167617308728829.

Cundari, A., Ferguson, A.K., 1982. Significance of the pyroxene chemistry from leucite-bearing and related assemblages. TMPM Tschermaks Mineralogische und Petrographische Mitteilungen 30, 189–204. doi:10.1007/BF01082329.

Cundari, A., Renard, J.G., Gleadow, A.J., 1978. Uranium-Potassium relationship and apatite fission-track ages for a differentiated leucitite suite from New South Wales (Australia). Chemical Geology 22, 11–20. URL: https://www.sciencedirect.com/science/article/pii/0009254178900177, doi:10.1016/0009-2541(78)90017-7.

Cundari, A., Salviulo, G., 1989. Ti solubility in diopsidic pyroxene from a suite of New South Wales leucitites (Australia). Lithos 22, 191–198. URL: https://www.sciencedirect.com/science/article/pii/0024493789900558, doi:10.1016/0024-4937(89)90055-8.

Curran, J.M., 1888. Note on a leucite-basalt from central New South Wales. Proceedings of the Linnean Society of New South Wales. 2, 974–975. doi:10.5962/bhl.part.29220.

Curran, J.M., 1891. A contribution to the microscopic structure of some Australian rocks. Journal and proceedings of the Royal Society of New South Wales 25, 179–233. URL: https://www.biodiversitylibrary.org/part/359111, doi:10.5962/p.359111.

Dalton, H., Giuliani, A., Fitzpayne, A., Peters, B.J., 2025. New geochemical and Sr-Nd-Hf isotopic constraints on the genesis of kimberlites and ultramafic lamprophyres from the Adelaide Fold Belt and Gawler Craton, South Australia. Mineralogy and Petrology URL: https://doi.org/10.1007/s00710-025-00938-w, doi:10.1007/s00710-025-00938-w.

Dasgupta, R., Hirschmann, M.M., 2006. Melting in the Earth's deep upper mantle caused by carbon dioxide. Nature 440, 659–662. doi:10.1038/nature04612.

Dasgupta, R., Hirschmann, M.M., Smith, N.D., 2007. Partial melting experiments of peridotite + CO2 at 3 GPa and genesis of alkalic ocean island basalts. Journal of Petrology 48, 2093–2124. doi:10.1093/petrology/egm053.

David, T.W.E., Anderson, W., 1889. The Leucite-basalts of N. S. Wales. Records of the Geological Survey of New South Wales 1, 153–172.

Davies, D.R., Rawlinson, N., Iaffaldano, G., Campbell, I.H., 2015. Lithospheric controls on magma composition along Earth's longest continental hotspot track. Nature 525, 511–514. URL: http://www.nature.com/articles/nature14903, doi:10.1038/nature14903.

Davies, R.M., O'Reilly, S.Y., Griffin, W.L., 2002. Multiple Origins of Alluvial Diamonds from New South Wales, Australia. Economic Geology 97, 109–123.

Dawson, J.B., 1984. Contrasting types of upper-mantle metasomatism. Kimberlites II: The Mantle and Crust-Mantle Relationships , 289–294doi:10.1016/b978-0-444-42274-3.50030-5.

Dawson, J.B., Smith, J.V., 1973. Alkalic pyroxenite xenoliths from the lashaine volcano, Northern Tanzania. Journal of Petrology 14, 113–131. doi:10.1093/petrology/14.1.113.

Day, H.W., 2012. A revised diamond-graphite transition curve. American Mineralogist 97, 52–62. doi:10.2138/am.2011.3763.

Dickinson, W.R., 1975. Potash-Depth (K-h) relations in continental margin and intra-oceanic magmatic arcs. Geology 3, 53–56. doi:10.1130/0091-7613(1975)3<53:PKRICM>2.0.CO;2.

Domanik, K.J., Holloway, J.R., 2000. Experimental synthesis and phase relations of phengitic muscovite from 6.5 to 11 GPa in a calcareous metapelite from the Dabie Mountains, China. Lithos 52, 51–77. doi:10.1016/S0024-4937(99)00084-5.

Doublier, M.P., Purdy, D.J., Hegarty, R., Nicoll, M.G., Zwingmann, H., 2018. Structural elements of the southern Thomson Orogen (Australian Tasmanides): a tale of megafolds. Australian Journal of Earth Sciences 65, 943–966. URL: https://doi.org/10.1080/08120099.2018.1526213, doi:10.1080/08120099.2018.1526213.

Dupuy, C., Liotard, J.M., Dostal, J., 1992. Zr/hf fractionation in intraplate basaltic rocks: Carbonate metasomatism in the mantle source. Geochimica et Cosmochimica Acta 56, 2417–2423. doi:10.1016/0016-7037(92)90198-R.

Duvernay, T., Davies, D.R., Mathews, C.R., Gibson, A.H., Kramer, S.C., 2021. Linking Intraplate Volcanism to Lithospheric Structure and Asthenospheric Flow. Geochemistry, Geophysics, Geosystems 22, 1–29. doi:10.1029/2021GC009953.

Duvernay, T., Davies, D.R., Mathews, C.R., Gibson, A.H., Kramer, S.C., 2022. Continental Magmatism: The Surface Manifestation of Dynamic Interactions Between Cratonic Lithosphere, Mantle Plumes and Edge-Driven Convection. Geochemistry, Geophysics, Geosystems 23. doi:10.1029/2022GC010363.

Ebinger, C.J., Yemane, T., Harding, D.J., Tesfaye, S., Kelley, S., Rex, D.C., 2000. Rift deflection, migration, and propagation: Linkage of the Ethiopian and Eastern rifts, Africa. Bulletin of the Geological Society of America 112, 163–176. doi:10.1130/0016-7606(2000)112<163:RDMAPL>2.0.CO;2.

Edgar, A.D., Lloyd, F.E., Vukadinovic, D., 1994. The role of fluorine in the evolution of ultrapotassic magmas. Mineralogy and Petrology 51, 173–193. doi:10.1007/BF01159726.

Edgar, A.D., Mitchell, R.H., 1997. Ultra high pressure-temperature melting experiments on an SiO2-rich lamproite from Smoky Butte, Montana: Derivation of siliceous lamproite magmas from enriched sources deep in the Continental Mantle. Journal of Petrology 38, 457–477. doi:10.1093/petroj/38.4.457.

Elkins-Tanton, L.T., Grove, T.L., 2003. Evidence for deep melting of hydrous metasomatized mantle: Pliocene high-potassium magmas from the Sierra Nevadas. Journal of Geophysical Research: Solid Earth 108. doi:10.1029/2002jb002168.

Elliott, T., Plank, T., Zindler, A., White, W., Bourdon, B., 1997. Element transport from slab to volcanic front at the Mariana arc. Journal of Geophysical Research: Solid Earth 102, 14991–15019. URL: https://agupubs.onlinelibrary.wiley.com/doi/10.1029/97JB00788,

doi:10.1029/97JB00788.

Erlank, A.J., Waters, F.G., Hawkesworth, C.J., Haggerty, S.E., Allsopp, H.L., Rickard, R.S., Menzies, M.A., 1987. Evidence for mantle metasomatism in peridotite nodules from the Kimberley pipes, South Africa. Mantle Metasomatism , 221–311URL: https://www.scopus.com/inward/record.uri?eid=2-s2.0-0023469399&partnerID=40&md5=8e5113147b2ca27467fa10bea5cf4bd1.

Ersoy, Y.E., Palmer, M.R., Uysal, I., Gündoğan, I., 2014. Geochemistry and petrology of the Early Miocene lamproites and related volcanic rocks in the Thrace Basin, NW Anatolia. Journal of Volcanology and Geothermal Research 283, 143–158. doi:10.1016/j.jvolgeores.2014.06.016.

Ewart, A., Chappell, B.W., Menzies, M.A., 1988. An overview of the geochemical and isotopic characteristics of the eastern australian cainozoic volcanic provinces. Journal of Petrology Special_Vo, 225–273. doi:10.1093/petrology/Special_Volume.1.225.

Ezad, I.S., Foley, S.F., 2022. Experimental partitioning of fluorine and barium in lamproites. American Mineralogist 107, 2008–2019. doi:10.2138/am-2022-8289.

Falloon, T.J., Green, D.H., 1988. Anhydrous partial melting of peridotite from 8 to 35 kb and the petrogenesis of morb. Journal of Petrology Special_Vo, 379–414. doi:10.1093/petrology/Special_Volume.1.379.

Falloon, T.J., Green, D.H., O'Neill, H.S.C., Hibberson, W.O., 1997. Experimental tests of low degree peridotite partial melt compositions: Implications for the nature of anhydrous near-solidus peridotite melts at 1 GPa. Earth and Planetary Science Letters 152, 149–162. doi:10.1016/s0012-821x(97)00155-6.

Farmer, G.L., Glazner, A.F., Manley, C.R., 2002. Did lithospheric delamination trigger late Cenozoic potassic volcanism in the southern Sierra Nevada, California? Bulletin of the Geological Society of America 114, 754–768. doi:10.1130/0016-7606(2002)114<0754:DLDTLC>2.0.CO;2.

Farsang, S., Louvel, M., Zhao, C., Mezouar, M., Rosa, A.D., Widmer, R.N., Feng, X., Liu, J., Redfern, S.A., 2021. Deep carbon cycle constrained by carbonate solubility. Nature Communications 12, 1–9. URL: http://dx.doi.org/10.1038/s41467-021-24533-7, doi:10.1038/s41467-021-24533-7.

Fergusson, C.L., Henderson, R.A., 2015. Early Palaeozoic continental growth in the Tasmanides of northeast Gondwana and its implications for Rodinia assembly and rifting. Gondwana Research 28, 933–953. URL: http://dx.doi.org/10.1016/j.gr.2015.04.001, doi:10.1016/j.gr.2015.04.001.

Foley, S., 1989. The genesis of lamproitic magmas in a reduced fluorine-rich mantle, in: Ross, J., Jaques, A.L., Ferguson, J., Green, D.H., O'Reilly, S.Y., Danchin, R.V., Janse, A.J.A. (Eds.), Kimberlites and related rocks, volume 1: their composition, occurrence, origin and emplacement. Carlton, Vic, pp. 616–631.

Foley, S., 1991. High-pressure stability of the fluor- and hydroxy-endmembers of pargasite and K-richterite. Geochimica et Cosmochimica Acta 55, 2689–2694. doi:10.1016/0016-7037(91)90386-J.

Foley, S., 1992a. Petrological characterization of the source components of potassic magmas: geochemical and experimental constraints. Lithos 28, 187–204. URL: https://linkinghub.elsevier.com/retrieve/pii/002449379290006K, doi:10.1016/0024-4937(92)90006-K.

Foley, S., 1992b. Vein-plus-wall-rock melting mechanisms in the lithosphere and the origin of potassic alkaline magmas. Lithos 28, 435–453. doi:10.1016/0024-4937(92)90018-T.

Foley, S., Venturelli, G., Green, D., Toscani, L., 1987. The ultrapotassic rocks: Characteristics, classification, and constraints for petrogenetic models. Earth-Science Reviews 24, 81–134. URL: https://linkinghub.elsevier.com/retrieve/pii/0012825287900018, doi:10.1016/0012-8252(87)90001-8.

Foley, S.F., 1993. An experimental study of olivine lamproite: First results from the diamond stability field. Geochimica et Cosmochimica Acta 57, 483–489. doi:10.1016/0016-7037(93)90448-6.

Foley, S.F., 2008. Rejuvenation and erosion of the cratonic lithosphere. Nature Geoscience 1, 503–510. doi:10.1038/ngeo261.

Foley, S.F., 2011. A reappraisal of redox melting in the earth's mantle as a function of tectonic setting and time. Journal of Petrology 52, 1363–1391. doi:10.1093/petrology/egq061.

Foley, S.F., Chen, C., Jacob, D.E., 2024. The effects of local variations in conditions on carbon storage and release in the continental mantle. National Science Review 11. URL: https://doi.org/10.1093/nsr/nwae098, doi:10.1093/nsr/nwae098.

Foley, S.F., Ezad, I.S., 2024. Melting of hydrous pyroxenites with alkali amphiboles in the continental mantle: 2. Trace element compositions of melts and minerals. Geoscience Frontiers 15, 101692. URL: https://doi.org/10.1016/j.gsf.2023.101692, doi:10.1016/j.gsf.2023.101692.

Foley, S.F., Ezad, I.S., van der Laan, S.R., Pertermann, M., 2022. Melting of hydrous pyroxenites with alkali amphiboles in the continental mantle: 1. Melting relations and major element compositions of melts. Geoscience Frontiers 13, 101380. URL: https://doi.org/10.1016/j.gsf.2022.101380, doi:10.1016/j.gsf.2022.101380.

Foley, S.F., Ezad, I.S., Shu, C., Förster, M.W., 2025. Melting of amphibole-apatite-rich metasomes in the continental mantle and comparison of melt compositions with natural igneous rocks. Lithos , 107976URL: https://doi.org/10.1016/j.lithos.2025.107976https://linkinghub.elsevier.com/retrieve/pii/S0024493725000350, doi:10.1016/j.lithos.2025.107976.

Foley, S.F., Fischer, T.P., 2017. An essential role for continental rifts and lithosphere in the deep carbon cycle. Nature Geoscience 10, 897–902. URL: http://dx.doi.org/10.1038/s41561-017-0002-7, doi:10.1038/s41561-017-0002-7.

Foley, S.F., Pertermann, M., 2021. Dynamic metasomatism experiments investigating the interaction between migrating potassic melt and garnet peridotite. Geosciences (Switzerland) 11. doi:10.3390/geosciences11100432.

Foley, S.F., Pintér, Z., 2018. Primary Melt Compositions in the Earth's Mantle, in: Kono, Y., Sanloup, C. (Eds.), Magmas Under Pressure. Elsevier, Amsterdam. chapter 1, pp. 3–42. doi:10.1016/B978-0-12-811301-1.00001-0.

Foley, S.F., Yaxley, G.M., Rosenthal, A., Buhre, S., Kiseeva, E.S., Rapp, R.P., Jacob, D.E., 2009. The composition of near-solidus melts of peridotite in the presence of CO2 and H2O between 40 and 60 kbar. Lithos 112, 274–283. URL: http://dx.doi.org/10.1016/j.lithos.2009.03.020, doi:10.1016/j.lithos.2009.03.020.

Förster, M.W., Bussweiler, Y., Prelević, D., Daczko, N.R., Buhre, S., Mertz-Kraus, R., Foley, S.F., 2021. Sediment-Peridotite Reaction Controls Fore-Arc Metasomatism and Arc Magma Geochemical Signatures. Geosciences 11, 372. URL: https://www.mdpi.com/2076-3263/11/9/372, doi:10.3390/geosciences11090372.

Förster, M.W., Prelević, D., Buhre, S., Mertz-Kraus, R., Foley, S.F., 2019. An experimental study of the role of partial melts of sediments versus mantle melts in the sources of potassic magmatism. Journal of Asian Earth Sciences 177, 76–88. URL: https://linkinghub.elsevier.com/retrieve/pii/S1367912019301270, doi:10.1016/j.jseaes.2019.03.014.

Fraser, K.J., Hawkesworth, C.J., Erlank, A.J., Mitchell, R.H., Scott-Smith, B.H., 1985. Sr, Nd and Pb isotope and minor element geochemistry of lamproites and kimberlites. Earth and Planetary Science Letters 76, 57–70. doi:10.1016/0012-821X(85)90148-7.

Frey, F.A., Green, D.H., 1974. The mineralogy, geochemistry and origin of Iherzolite inclusions in Victorian basanites. Geochimica et Cosmochimica Acta 38, 1023–1059. doi:10.1016/0016-7037(74)90003-9.

Frey, F.A., Green, D.H., Roy, S.D., 1978. Integrated models of basalt petrogenesis: A study of quartz tholeiites to olivine melilitites from South Eastern Australia utilizing geochemical and experimental petrological data. Journal of Petrology 19, 463–513. doi:10.1093/petrology/19.3.463.

Fritschle, T., Prelević, D., Foley, S.F., Jacob, D.E., 2013. Petrological characterization of the mantle source of Mediterranean lamproites: Indications from major and trace elements of phlogopite. Chemical Geology 353, 267–279. doi:10.1016/j.chemgeo.2012.09.006.

Funk, S.P., Luth, R.W., 2013. Melting phase relations of a mica-clinopyroxenite from the Milk River area, southern Alberta, Canada. Contributions to Mineralogy and Petrology 166, 393–409. doi:10.1007/s00410-013-0881-6.

Furman, T., Graham, D., 1999. Erosion of lithospheric mantle beneath the East African Rift system: Geochemical evidence from the Kivu volcanic province. Lithos 48, 237–262. doi:10.1016/S0024-4937(99)00031-6.

Gale, A., Dalton, C.A., Langmuir, C.H., Su, Y., Schilling, J.G., 2013. The mean composition of ocean ridge basalts. Geochemistry, Geophysics, Geosystems 14, 489–518. doi:10.1029/2012GC004334.

Gaul, O.F., Griffin, W.L., O'Reilly, S.Y., Pearson, N.J., 2000. Mapping olivine composition in the lithospheric mantle. Earth and Planetary Science Letters 182, 223–235. URL: http://www.sciencedirect.com/science/article/pii/S0012821X00002430, doi:http://dx.doi.org/10.1016/S0012-821X(00)00243-0.

Gaul, O.F., O'Reilly, S.Y., Griffin, W.L., 2003. Lithosphere structure and evolution in southeastern Australia. Special Paper of the Geological Society of America 372, 185–202. doi:10.1130/0-8137-2372-8.185.

Ghent, E.D., Edwards, B.R., Russell, J.K., 2019. Pargasite-bearing vein in spinel lherzolite from the mantlelithosphere of the North America cordillera. Canadian Journal of Earth Sciences 56, 870–885. doi:10.1139/cjes-2018-0239.

Gibson, S.A., Thompson, R.N., Leat, P.T., Morrison, M.A., Hendry, G.L., Dickin, A.P., Mitchell, J.G., 1993. Ultrapotassic magmas along the flanks of the oligo-miocene rio grande rift, USA: Monitors of the zone of lithospheric mantle extension and thinning beneath a continental rift. Journal of Petrology 34, 187–228. doi:10.1093/petrology/34.1.187.

Giuliani, A., Dalton, H., Pearson, D.G., 2024. Kimberlites: The deepest geochemical probes of Earth. volume 1. doi:10.1016/B978-0-323-99762-1.00064-4.

Giuliani, A., Schmidt, M.W., Torsvik, T.H., Fedortchouk, Y., 2023. Genesis and evolution of kimberlites. Nature Reviews Earth & Environment 4, 738–753. URL: https://www.nature.com/articles/s43017-023-00481-2, doi:10.1038/s43017-023-00481-2.

Glen, R.A., 2005. The Tasmanides of eastern Australia. Geological Society, London, Special Publications 246, 23–96. URL: http://sp.lyellcollection.org/lookup/doi/10.1144/GSL.SP.2005.246.01.02, doi:10.1144/GSL.SP.2005.246.01.02.

Glen, R.A., Belousova, E., Griffin, W.L., 2016. Different styles of modern and ancient non-collisional Orogens and implications for crustal growth: A Gondwanaland perspective. Canadian Journal of Earth Sciences 53, 1372–1415. doi:10.1139/cjes-2015-0229.

Glen, R.A., Korsch, R.J., Hegarty, R., Saeed, A., Djomani, Y.P., Costelloe, R.D., Belousova, E., 2013. Geodynamic significance of the boundary between the Thomson Orogen and the Lachlan Orogen, northwestern New South Wales and implications for Tasmanide tectonics. Australian Journal of Earth Sciences 60, 371–412. doi:10.1080/08120099.2013.782899.

Green, D.H., 2015. Experimental petrology of peridotites, including effects of water and carbon on melting in the Earth's upper mantle. Physics and Chemistry of Minerals 42, 95–122. URL: https://doi.org/10.1007/s00269-014-0729-2, doi:10.1007/s00269-014-0729-2.

Green, D.H., Hibberson, W.O., Rosenthal, A., Kovács, I., Yaxley, G.M., Falloon, T., Brink, F., 2014. Experimental study of the influence of water on melting and phase assemblages in the upper mantle. Journal of Petrology 55, 2067–2096. doi:10.1093/petrology/egu050.

Griffin, W.L., O'Reilly, S.Y., A., S., 1988. Mantle metasomatism beneath western Victoria, Australia: II. Isotopic geochemistry of Cr-diopside lherzolites and Al-augite pyroxenites. Geochimica et Cosmochimica Acta 52, 449–459. doi:10.1016/0016-7037(88)90100-7.

Griffin, W.L., O'Reilly, S.Y., Davies, R.M., 1998. Subduction-Related Diamond Deposits? Constraints, Possibilities, and New Data from Eastern Australia, in: Vokes, F.M., Marshall, B., Spry, P.G. (Eds.), Metamorphic and Metamorphogenic Ore Deposits. Society of Economic Geologists. January, pp. 1–20. URL: http://pubs.geoscienceworld.org/books/book/1221/chapter/107021009/SubductionRelated-Diamond-Deposits-Constraints, doi:10.5382/Rev.11.13.

1217 Griffin, W.L., Sutherland, F.L., Hollis, J.D., 1987. Geothermal profile and crust-mantle transition beneath east-central Queensland:
1218 Volcanology, xenolith petrology and seismic data. Journal of Volcanology and Geothermal Research 31, 177–203. doi:10.1016/
1219 0377-0273(87)90067-9.
1220 Griffin, W.L., Wass, S.Y., Hollis, J.D., 1984. Ultramafic Xenoliths from Bullenmerri and Gnotuk Maars, Victoria, Australia: Petrology of a
1221 Sub-Continental Crust-Mantle Transition. Journal of Petrology 25, 53–87. URL: http://petrology.oxfordjournals.org/, doi:10.1093/
1222 petrology/25.1.53.
1223 Gupta, A.K., Fyfe, W.S., 1975. Leucite survival; the alteration to analcime. The Canadian Mineralogist 13, 361–363.
1224 Harlow, G.E., 2003. Diopside + F-rich phlogopite at high P and T: Systematics, crystal chemistry and the stability of KMgF3, clinohumite
1225 and chondrodite. American Mineralogist 88, 1625.
1226 Harlow, G.E., Davies, R., 2004. Status report on stability of K-rich phases at mantle conditions. Lithos 77, 647–653. doi:10.1016/j.lithos.
1227 2004.04.010.
1228 Harte, B., 1983. Mantle peridotites and processes - the kimberlite sample. Continental Basalts and Mantle Xenoliths , 46–91.
1229 Harvey, M.H., Joplin, G.A., 1940. A note on some leucite bearing rocks from New South Wales with special reference to an ultrabasic
1230 occurrence at Murrumburrah. Journal and proceedings of the Royal Society of New South Wales 74, 419–441. URL: https://www.
1231 biodiversitylibrary.org/pdf4/100904400174258.pdf.
1232 Hauri, E.H., Maclennan, J., McKenzie, D., Gronvold, K., Oskarsson, N., Shimizu, N., 2018. CO2 content beneath northern Iceland and the
1233 variability of mantle carbon. Geology 46, 55–58. doi:10.1130/G39413.1.
1234 Heath, M., Phillips, D., Matchan, E.L., 2018. An evidence-based approach to accurate interpretation of 40Ar/39Ar ages from basaltic rocks.
1235 Earth and Planetary Science Letters 498, 65–76. doi:10.1016/j.epsl.2018.06.024.
1236 Heath, M., Phillips, D., Matchan, E.L., 2020. Basalt lava flows of the intraplate Newer Volcanic Province in south-east Australia (Melbourne
1237 region): 40Ar/39Ar geochronology reveals ∼8 Ma of episodic activity. Journal of Volcanology and Geothermal Research 389. doi:10.1016/
1238 j.jvolgeores.2019.106730.
1239 Herzberg, C., 2011. Identification of source lithology in the Hawaiian and Canary Islands: Implications for origins. Journal of Petrology 52,
1240 113–146. doi:10.1093/petrology/egq075.
1241 Herzberg, C., Asimow, P.D., 2008. Petrology of some oceanic island basalts: PRIMELT2.XLS software for primary magma calculation.
1242 Geochemistry, Geophysics, Geosystems 9. doi:10.1029/2008GC002057.
1243 Hirose, K., 1997. Partial melt compositions of carbonated peridotite at 3 GPa and role of CO2 in alkali-basalt magma generation. Geophysical
1244 Research Letters 24, 2837–2840. doi:10.1029/97GL02956.
1245 Hirose, K., Kushiro, I., 1993. Partial melting of dry peridotites at high pressures: Determination of compositions of melts segregated from
1246 peridotite using aggregates of diamond. Earth and Planetary Science Letters 114, 477–489. doi:10.1016/0012-821X(93)90077-M.
1247 Hirschmann, M.M., Kogiso, T., Baker, M.B., Stolper, E.M., 2003. Alkalic magmas generated by partial melting of garnet pyroxenite. Geology
1248 31, 481–484. doi:10.1130/0091-7613(2003)031<0481:AMGBPM>2.0.CO;2.
1249 Hofmann, A.W., Jochum, K.P., Seufert, M., White, W.M., 1986. Nb and Pb in oceanic basalts: new constraints on mantle evolution. Earth
1250 and Planetary Science Letters 79, 33–45. doi:10.1016/0012-821X(86)90038-5.
1251 Hoggard, M.J., Czarnota, K., Richards, F.D., Huston, D.L., Jaques, A.L., Ghelichkhan, S., 2020. Global distribution of sediment-hosted
1252 metals controlled by craton edge stability. Nature Geoscience 13, 504–510. URL: http://dx.doi.org/10.1038/s41561-020-0593-2,
1253 doi:10.1038/s41561-020-0593-2.

Hough, F.E., 1972. The petrogenesis of strongly alkaline mafic lavas and associated nodule suites from the West Eifel and south west Uganda. Ph.D. thesis. University of Reading.

Innocenzi, F., Ronca, S., Agostini, S., Benedetti, F., Lustrino, M., 2024. On the occurrence of kalsilite in melilite-bearing ultrapotassic lavas from the Roman Province (Vulsini Mts., central Italy). Lithos 482-483, 107704. URL: https://doi.org/10.1016/j.lithos.2024.107704, doi:10.1016/j.lithos.2024.107704.

Irvine, T.N., Baragar, W.R.A., 1971. A Guide to the Chemical Classification of the Common Volcanic Rocks. Canadian Journal of Earth Sciences 8, 523–548. URL: http://www.nrcresearchpress.com/doi/10.1139/e71-055, doi:10.1139/e71-055.

Irving, A.J., 1974. Geochemical and high pressure experimental studies of garnet pyroxenite and pyroxene granulite xenoliths from the delegate basaltic pipes, Australia. Journal of Petrology 15, 1–40. doi:10.1093/petrology/15.1.1.

Irving, A.J., Frey, F.A., 1984. Trace element abundances in megacrysts and their host basalts: Constraints on partition coefficients and megacryst genesis. Geochimica et Cosmochimica Acta 48, 1201–1221. doi:10.1016/0016-7037(84)90056-5.

Ishimaru, S., Arai, S., 2008. Calcic amphiboles in peridotite xenoliths from Avacha volcano, Kamchatka, and their implications for metasomatic conditions in the mantle wedge. Geological Society Special Publication 293, 35–55. doi:10.1144/SP293.3.

Ito, M., 1986. Kimberlites and their ultramafic xenoliths from western Kenya. TMPM Tschermaks Mineralogische und Petrographische Mitteilungen 35, 193–216. doi:10.1007/BF01082085.

Jacob, D., 2004. Nature and origin of eclogite xenoliths from kimberlites. Lithos 77, 295–316. URL: https://linkinghub.elsevier.com/retrieve/pii/S0024493704001045, doi:10.1016/j.lithos.2004.03.038.

Jacob, D.E., Viljoen, K.S., Grassineau, N.V., 2009. Eclogite xenoliths from Kimberley, South Africa - A case study of mantle metasomatism in eclogites. Lithos 112, 1002–1013. URL: http://dx.doi.org/10.1016/j.lithos.2009.03.034, doi:10.1016/j.lithos.2009.03.034.

Jaques, A.L., 2002. Australian diamond deposits, kimberlites, and related rocks. 1: 5 000 000 scale map. URL: https://www.ga.gov.au/pdf/RR0114.pdf.

Jaques, A.L., Foley, S.F., 2018. Insights into the petrogenesis of the West Kimberley lamproites from trace elements in olivine. Mineralogy and Petrology 112. doi:10.1007/s00710-018-0612-9.

Jaques, A.L., Lewis, J.D., Smith, C.B., 1986. The Kimberlites and Lamproites of Western Australia. volume 132. Government Printing Office, Perth.

Jaques, A.L., Lewis, J.D., Smith, C.B., Gregory, G.P., Ferguson, J., Chappell, B.W., McCulloch, M.T., 1984. The diamond-bearing ultrapotassic (lamproitic) rocks of the West Kimberley region, Western Australia.. volume 11. Elsevier Science Publishers B.V. URL: http://dx.doi.org/10.1016/B978-0-444-42273-6.50023-7, doi:10.1016/b978-0-444-42273-6.50023-7.

Jia, Y., Kerrich, R., Gupta, A.K., Fyfe, W.S., 2003. 15N-enriched Gondwana lamproites, eastern India: Crustal N in the mantle source. Earth and Planetary Science Letters 215, 43–56. doi:10.1016/S0012-821X(03)00426-6.

Jochum, K.P., Nohl, U., Herwig, K., Lammel, E., Stoll, B., Hofmann, A.W., 2005. GeoReM: A new geochemical database for reference materials and isotopic standards. Geostandards and Geoanalytical Research 29, 333–338. doi:10.1111/j.1751-908x.2005.tb00904.x.

Johnson, B., Goldblatt, C., 2015. The nitrogen budget of Earth. Earth-Science Reviews 148, 150–173. URL: http://dx.doi.org/10.1016/j.earscirev.2015.05.006, doi:10.1016/j.earscirev.2015.05.006, arXiv:1505.03813.

Johnson, R. (Ed.), 1989. Intraplate Volcanism in Eastern Australia and New Zealand. Cambridge University Press.

Judd, J.W., 1887. On the Discovery of Leucite in Australia. Mineralogical Magazine and Journal of the Mineralogical Society 7, 194–195. URL: https://www.cambridge.org/core/product/AD6A8061FFF8A3882C0B31DD671B657B, doi:DOI:10.1180/minmag.1887.007.35.06.

Katz, R.F., Spiegelman, M., Langmuir, C.H., 2003. A new parameterization of hydrous mantle melting. Geochemistry, Geophysics, Geosystems 4, 1–19. doi:10.1029/2002GC000433.

Kennett, B., Saygin, E., Fomin, T., Blewett, R.S., 2016. Deep Crustal Seismic Reflection Profiling, Australia: 1978-2015. 2nd ed., Australian National University Press, Acton.

King, S.D., Anderson, D.L., 1995. An alternative mechanism of flood basalt formation. Earth and Planetary Science Letters 136, 269–279. doi:10.1016/0012-821X(95)00205-Q.

King, S.D., Anderson, D.L., 1998. Edge-driven convection. Earth and Planetary Science Letters 160, 289–296. doi:10.1016/S0012-821X(98)00089-2.

Kirkby, A.L., Musgrave, R.J., Czarnota, K., Doublier, M.P., Duan, J., Cayley, R.A., Kyi, D., 2020. Lithospheric architecture of a Phanerozoic orogen from magnetotellurics: AusLAMP in the Tasmanides, southeast Australia. Tectonophysics 793, 228560. URL: https://doi.org/10.1016/j.tecto.2020.228560, doi:10.1016/j.tecto.2020.228560.

Klemme, S., van der Laan, S., Foley, S., Günther, D., 1995. Experimentally determined trace and minor element partitioning between clinopyroxene and carbonatite melt under upper mantle conditions. Earth and Planetary Science Letters 133, 439–448. URL: https://linkinghub.elsevier.com/retrieve/pii/0012821X9500098W, doi:10.1016/0012-821X(95)00098-W.

Klöcking, M., White, N.J., Maclennan, J., McKenzie, D., Fitton, J.G., 2018. Quantitative Relationships Between Basalt Geochemistry, Shear Wave Velocity, and Asthenospheric Temperature Beneath Western North America. Geochemistry, Geophysics, Geosystems 19, 3376–3404. doi:10.1029/2018GC007559.

Kogiso, T., Hirschmann, M.M., Frost, D.J., 2003. High-pressure partial melting of garnet pyroxenite: Possible mafic lithologies in the source of ocean island basalts. Earth and Planetary Science Letters 216, 603–617. doi:10.1016/S0012-821X(03)00538-7.

Konzett, J., 1997. Phase relations and chemistry of Ti-rich K-richterite-bearing mantle assemblages: an experimental study to 8.0 GPa in a Ti-KNCMASH system. Contributions to Mineralogy and Petrology 128, 385–404. doi:10.1007/s004100050316.

Konzett, J., Fei, Y., 2000. Transport and storage of potassium in the earth's upper mantle and transition zone: An experimental study to 23 GPa in simplified and natural bulk compositions. Journal of Petrology 41, 583–603. doi:10.1093/petrology/41.4.583.

Konzett, J., Sweeney, R.J., Thompson, A.B., Ulmer, P., 1997. Potassium amphibole stability in the upper mantle: An experimental study in a peralkaline KNCMASH system to 8 · 5 GPa. Journal of Petrology 38, 537–568. doi:10.1093/petroj/38.5.537.

Konzett, J., Ulmer, P., 1999. The stability of hydrous potassic phases in lherzolitic mantle-An experimental study to 9.5 GPa in simplified and natural bulk compositions. Journal of Petrology 40, 629–652. doi:10.1093/petroj/40.4.629.

de Laat, J.I., Lebedev, S., Celli, N.L., Bonadio, R., Chagas de Melo, B., Rawlinson, N., 2023. Structure and evolution of the Australian plate and underlying upper mantle from waveform tomography with massive data sets. Geophysical Journal International 234, 153–189. URL: https://doi.org/10.1093/gji/ggad062, doi:10.1093/gji/ggad062.

Lambart, S., Laporte, D., Provost, A., Schiano, P., 2012. Fate of pyroxenite-derived melts in the peridotitic mantle: Thermodynamic and experimental constraints. Journal of Petrology 53, 451–476. doi:10.1093/petrology/egr068.

Lambart, S., Laporte, D., Schiano, P., 2009. An experimental study of pyroxenite partial melts at 1 and 1.5 GPa: Implications for the major-element composition of Mid-Ocean Ridge Basalts. Earth and Planetary Science Letters 288, 335–347. URL: http://dx.doi.org/10.1016/j.epsl.2009.09.038, doi:10.1016/j.epsl.2009.09.038.

Lambart, S., Laporte, D., Schiano, P., 2013. Markers of the pyroxenite contribution in the major-element compositions of oceanic basalts: Review of the experimental constraints. Lithos 160-161, 14–36. URL: http://dx.doi.org/10.1016/j.lithos.2012.11.018, doi:10.1016/j.lithos.2012.11.018.

Lanati, A.W., Shea, J.J., 2025. Chemical analyses of the Eastern Australian Potassic Suite: Whole-rock major, trace, and volatile element geochemistry. doi:https://doi.org/10.5880/digis.2025.005.

Lanati, A.W., Shea, J.J., Foley, S.F., Klöcking, M.S., Rohrbach, A., Gerdes-Berndt, J., Klemme, S., in prep. The petrology, geochemistry, & origin of the east australian potassic suite: The minerals.

LaTourrette, T., Hervig, R.L., Holloway, J.R., 1995. Trace element partitioning between amphibole, phlogopite, and basanite melt. Earth and Planetary Science Letters 135, 13–30. doi:10.1016/0012-821X(95)00146-4.

Le Bas, M.J., 1989. Nephelinitic and basanitic rocks. Journal of Petrology 30, 1299–1312. doi:10.1093/petrology/30.5.1299.

Le Bas, M.J., Le Maitre, R.W., Streckeisen, A., Zanettin, B., 1986. A chemical classification of volcanic rocks based on the total alkali-silica diagram. Journal of Petrology 27, 745–750. doi:10.1093/petrology/27.3.745.

Le Bas, M.J., Streckeisen, A.L., 1991. The IUGS systematics of igneous rocks. Journal of the Geological Society 148, 825–833. URL: http://jgs.lyellcollection.org/content/148/5/825.shorthttp://jgs.lyellcollection.org/cgi/doi/10.1144/gsjgs.148.5.0825, doi:10.1144/gsjgs.148.5.0825.

Le Maitre, R.W., Streckeisen, A., Zanettin, B., Le Bas, M.J., Bonin, B., Bateman, P. (Eds.), 2002. Igneous Rocks: A Classification and Glossary of Terms: Recommendations of the International Union of Geological Sciences Subcommission on the Systematics of Igneous Rocks. 2 ed., Cambridge University Press, Cambridge. URL: https://www.cambridge.org/core/product/7F458E82BF81BF6A011CEA0D41DE9311, doi:DOI:10.1017/CBO9780511535581.

Lee, C.T.A., Cheng, X., Horodyskyj, U., 2006. The development and refinement of continental arcs by primary basaltic magmatism, garnet pyroxenite accumulation, basaltic recharge and delamination: Insights from the Sierra Nevada, California. Contributions to Mineralogy and Petrology 151, 222–242. URL: https://link.springer.com/article/10.1007/s00410-005-0056-1, doi:10.1007/s00410-005-0056-1.

Lee, C.T.A., Luffi, P., Plank, T., Dalton, H., Leeman, W.P., 2009. Constraints on the depths and temperatures of basaltic magma generation on Earth and other terrestrial planets using new thermobarometers for mafic magmas. Earth and Planetary Science Letters 279, 20–33. doi:10.1016/j.epsl.2008.12.020.

Libon, L., Spiekermann, G., Blanchard, I., Kaa, J.M., Dominijanni, S., Sieber, M.J., Förster, M., Albers, C., Morgenroth, W., McCammon, C., Schreiber, A., Roddatis, V., Glazyrin, K., Husband, R.J., Hennet, L., Appel, K., Wilke, M., 2024. Reevaluating the fate of subducted magnesite in the Earth's lower mantle. Physics of the Earth and Planetary Interiors 355. doi:10.1016/j.pepi.2024.107238.

Liu, Z., Shea, J.J., Foley, S.F., Bussweiler, Y., Rohrbach, A., Klemme, S., Berndt, J., 2021. Clarifying source assemblages and metasomatic agents for basaltic rocks in eastern Australia using olivine phenocryst compositions. Lithos 390-391, 106122. URL: https://doi.org/10.1016/j.lithos.2021.106122, doi:10.1016/j.lithos.2021.106122.

Lloyd, F.E., Arima, M., Edgar, A.D., 1985. Partial melting of a phlogopite-clinopyroxenite nodule from south-west Uganda: an experimental study bearing on the origin of highly potassic continental rift volcanics. Contributions to Mineralogy and Petrology 91, 321–329. doi:10.1007/BF00374688.

Lloyd, F.E., Bailey, D.K., 1975. Light element metasomatism of the continental mantle: The evidence and the consequences. Physics and Chemistry of the Earth 9, 389–416. doi:10.1016/0079-1946(75)90030-0.

Lustrino, M., Fedele, L., Agostini, S., Prelević, D., Salari, G., 2019. Leucitites within and around the Mediterranean area. Lithos 324-325, 216–233. doi:10.1016/j.lithos.2018.11.007.

Lustrino, M., Wilson, M., 2007. The circum-Mediterranean anorogenic Cenozoic igneous province. Earth-Science Reviews 81, 1–65. doi:10.1016/j.earscirev.2006.09.002.

Luth, R.W., 1997. Experimental study of the system phlogopite-diopside from 3.5 to 17 GPa. American Mineralogist 82, 1198–1209. doi:10.2138/am-1997-11-1216.

Mallik, A., Dasgupta, R., Tsuno, K., Nelson, J., 2016. Effects of water, depth and temperature on partial melting of mantle-wedge fluxed by hydrous sediment-melt in subduction zones. Geochimica et Cosmochimica Acta 195, 226–243. URL: http://dx.doi.org/10.1016/j.gca.2016.08.018, doi:10.1016/j.gca.2016.08.018.

Mallik, A., Nelson, J., Dasgupta, R., 2015. Partial melting of fertile peridotite fluxed by hydrous rhyolitic melt at 2–3 GPa: implications for mantle wedge hybridization by sediment melt and generation of ultrapotassic magmas in convergent margins. Contributions to Mineralogy and Petrology 169. doi:10.1007/s00410-015-1139-2.

Manassero, M.C., Özaydın, S., Afonso, J.C., Shea, J.J., Ezad, I.S., Kirkby, A., Thiel, S., Fomin, I., Czarnota, K., 2024. Lithospheric Structure and Melting Processes in Southeast Australia: New Constraints From Joint Probabilistic Inversions of 3D Magnetotelluric and Seismic Data. Journal of Geophysical Research: Solid Earth 129, 1–30. doi:10.1029/2023JB028257.

Mandler, B.E., Grove, T.L., 2016. Controls on the stability and composition of amphibole in the Earth's mantle. Contributions to Mineralogy and Petrology 171, 1–20. doi:10.1007/s00410-016-1281-5.

Mather, B.R., Dietmar Müller, R., Seton, M., Ruttor, S., Nebel, O., Mortimer, N., 2020. Intraplate volcanism triggered by bursts in slab flux. Science Advances 6, 1–8. doi:10.1126/sciadv.abd0953.

Matthews, S., Shorttle, O., Maclennan, J., Rudge, J.F., 2021. The global melt inclusion C/Ba array: Mantle variability, melting process, or degassing? Geochimica et Cosmochimica Acta 293, 525–543. URL: https://doi.org/10.1016/j.gca.2020.09.030, doi:10.1016/j.gca.2020.09.030.

Matthews, S., Shorttle, O., Rudge, J.F., Maclennan, J., 2017. Constraining mantle carbon: CO2-trace element systematics in basalts and the roles of magma mixing and degassing. Earth and Planetary Science Letters 480, 1–14. URL: https://doi.org/10.1016/j.epsl.2017.09.047, doi:10.1016/j.epsl.2017.09.047.

McCulloch, M.T., Jaques, A.L., Nelson, D.R., Lewis, J.D., 1983. Nd and Sr isotopes in kimberlites and lamproites from Western Australia: An enriched mantle origin. Nature 302, 400–403. URL: https://www.nature.com/articles/302400a0, doi:10.1038/302400a0.

McDonough, W.F., 1990. Constraints on the composition of the continental lithospheric mantle. Earth and Planetary Science Letters 101, 1–18. doi:10.1016/0012-821X(90)90119-I.

McDougall, I., Wellman, P., 1976. Potassium-argon ages for some australian mesozoic igneous rocks. Journal of the Geological Society of Australia 23, 1–9. doi:10.1080/00167617608728916.

McQueen, K.G., Gonzalez, O.R., Roach, I.C., Pillans, B.J., Dunlap, W.J., Smith, M.L., 2007. Landscape and regolith features related to Miocene leucitite lava flows, El Capitan northeast of Cobar, New South Wales. Australian Journal of Earth Sciences 54, 1–17. doi:10.1080/08120090600923311.

Menzies, M.A., Wass, S.Y., 1983. CO 2-and LREE-rich mantle below eastern Australia: a REE and isotopic study of alkaline magmas and apatite-rich mantle xenoliths from the Southern Highlands Province, Australia. Earth and Planetary Science Letters 65, 387–302.

Middlemost, E.A., 1975. The basalt clan. Earth Science Reviews 11, 337–364. doi:10.1016/0012-8252(75)90039-2.

Mitchell, R.H., 1995. Melting experiments on a sanidine phlogopite lamproite at 4-7 gpa and their bearing on the sources of lamproitic magmas. Journal of Petrology 36, 1455–1474. doi:10.1093/petrology/36.5.1455.

Mitchell, R.H., 2020. Igneous Rock Associations 26. Lamproites, Exotic Potassic Alkaline Rocks: A Review of their Nomenclature, Characterization and Origins. Geoscience Canada 47, 119–142. URL: https://journals.lib.unb.ca/index.php/GC/article/view/31174, doi:10.12789/geocanj.2020.47.162.

Mitchell, R.H., 2021. Potassic Alkaline Rocks: Leucitites, Lamproites, and Kimberlites, in: Alderton, D., Elias, S.A. (Eds.), Encyclopedia of Geology. 2 ed.. Elsevier, pp. 215–239. URL: https://linkinghub.elsevier.com/retrieve/pii/B9780124095489124820, doi:10.1016/B978-0-12-409548-9.12482-0.

Mitchell, R.H., Bergman, S.C., 1991. Petrology of Lamproites. 1 ed., Springer New York, New York. doi:10.1007/978-1-4615-3788-5.

Miyawaki, R., Hatert, F., Pasero, M., Mills, S.J., 2021. Newsletter 61. Mineralogical Magazine 85, 459–463. URL: https://www.cambridge.org/core/product/identifier/S0026461X21000487/type/journal_article, doi:10.1180/mgm.2021.48.

Müller, D., Groves, D.I., 1993. Direct and indirect associations between potassic igneous rocks, shoshonites and gold-copper deposits. Ore Geology Reviews 8, 383–406. URL: https://www.sciencedirect.com/science/article/pii/016913689390035W, doi:10.1016/0169-1368(93)90035-W.

Müller, D., Rock, N.M., Groves, D.I., 1992. Geochemical discrimination between shoshonitic and potassic volcanic rocks in different tectonic settings: A pilot study. Mineralogy and Petrology 46, 259–289. URL: http://link.springer.com/10.1007/BF01173568, doi:10.1007/BF01173568.

Nelson, D.R., 1992. Isotopic characteristics of potassic rocks: evidence for the involvement of subducted sediments in magma genesis. Lithos 28, 403–420. doi:10.1016/0024-4937(92)90016-R.

Nelson, D.R., McCulloch, M.T., Sun, S.S., 1986. The origins of ultrapotassic rocks as inferred from Sr, Nd and Pb isotopes. Geochimica et Cosmochimica Acta 50, 231–245. doi:10.1016/0016-7037(86)90172-9.

Ngwenya, N.S., Tappe, S., 2021. Diamondiferous lamproites of the Luangwa Rift in central Africa and links to remobilized cratonic lithosphere. Chemical Geology 568, 120019. URL: https://doi.org/10.1016/j.chemgeo.2020.120019, doi:10.1016/j.chemgeo.2020.120019.

Novella, D., Frost, D.J., 2014. The composition of hydrous partial melts of garnet peridotite at 6GPa: Implications for the origin of group II Kimberlites. Journal of Petrology 55, 2097–2124. doi:10.1093/petrology/egu051.

O'Neill, C.J., Moresi, L., Jaques, A.L., 2005. Geodynamic controls on diamond deposits: Implications for Australian occurrences. Tectonophysics 404, 217–236. doi:10.1016/j.tecto.2005.04.010.

O'Reilly, S.Y., 1987. Volatile-rich mantle beneath eastern Australia, in: Nixon, P.H. (Ed.), Mantle Xenoliths. John Wiley & Sons, Chichester, UK, pp. 661–670.

O'Reilly, S.Y., Griffin, W., 1988. Mantle metasomatism beneath western Victoria, Australia: I. Metasomatic processes in Cr-diopside lherzolites. Geochimica et Cosmochimica Acta 52, 433–447. URL: https://linkinghub.elsevier.com/retrieve/pii/0016703788900993, doi:10.1016/0016-7037(88)90099-3.

O'Reilly, S.Y., Griffin, W.L., 1984. Sr isotopic heterogeneity in primitive basaltic rocks, southeastern Australia: correlation with mantle metasomatism. Contributions to Mineralogy and Petrology 87, 220–230. URL: http://link.springer.com/10.1007/BF00373055, doi:10.1007/BF00373055.

O'Reilly, S.Y., Griffin, W.L., 1985. A xenolith-derived geotherm for southeastern Australia and its geophysical implications. Tectonophysics 111, 41–63. doi:10.1016/0040-1951(85)90065-4.

O'Reilly, S.Y., Griffin, W.L., 2000. Apatite in the mantle: Implications for metasomatic processes and high heat production in Phanerozoic mantle. Lithos 53, 217–232. doi:10.1016/S0024-4937(00)00026-8.

O'Reilly, S.Y., Griffin, W.L., 2013. Mantle metasomatism, in: Harlov, D.E., Austrheim, H. (Eds.), Metasomatism and the Chemical Transformation of Rock. Lecture Notes in Earth System Sciences. 1 ed.. Springer Berlin Heidelberg. 9783642283932. chapter 12, pp. 471–533. doi:10.1007/978-3-642-28394-9_12.

O'Reilly, S.Y., Griffin, W.L., Pearson, N.J., Jackson, S.E., Belousova, E.A., Alard, O., Saeed, A., 2008. Taking the pulse of the Earth: Linking crustal and mantle events. Australian Journal of Earth Sciences 55, 983–995. doi:10.1080/08120090802097450.

Palme, H., O'Neill, H., 2013. Cosmochemical Estimates of Mantle Composition, in: Treatise on Geochemistry: Second Edition. Elsevier. volume 3, pp. 1–39. URL: https://www.sciencedirect.com/science/article/pii/B9780080959757002011?via%3Dihub, doi:10.1016/B978-0-08-095975-7.00201-1.

Paul, B., Hergt, J.M., Woodhead, J.D., 2005. Mantle heterogeneity beneath the Cenozoic volcanic provinces of central Victoria inferred from trace-element and Sr, Nd, Pb and Hf isotope data. Australian Journal of Earth Sciences 52, 243–260. URL: http://www.tandfonline.com/doi/abs/10.1080/08120090500139448, doi:10.1080/08120090500139448.

Pe-Piper, G., Piper, D.J., 1992. Geochemical variation with time in the Cenozoic high-k volcanic rocks of the island of Lesbos, Greece: significance for shoshonite petrogenesis. Journal of Volcanology and Geothermal Research 53, 371–387. URL: https://www.sciencedirect.com/science/article/pii/037702739290092R, doi:10.1016/0377-0273(92)90092-R.

Pe-Piper, G., Zhang, Y., Piper, D.J., Prelević, D., 2014. Relationship of Mediterranean type lamproites to large shoshonite volcanoes, Miocene of Lesbos, NE Aegean Sea. Lithos 184-187, 281–299. doi:10.1016/j.lithos.2013.11.004.

Pearce, J.A., 1983. Role of the sub-continental lithosphere in magma genesis at active continental margins. Continental Basalts and Mantle Xenoliths , 230–249.

Pearson, D.G., Woodhead, J., Janney, P.E., 2019. Kimberlites as geochemical probes of earth's mantle. Elements 15, 387–392. doi:10.2138/GSELEMENTS.15.6.387.

Pearson, N.J., Griffin, W.L., Alard, O., O'Reilly, S.Y., 2006. The isotopic composition of magnesium in mantle olivine: Records of depletion and metasomatism. Chemical Geology 226, 115–133. doi:10.1016/j.chemgeo.2005.09.029.

Peccerillo, A., Taylor, S.R., 1976. Geochemistry of eocene calc-alkaline volcanic rocks from the Kastamonu area, Northern Turkey. Contributions to Mineralogy and Petrology 58, 63–81. URL: http://link.springer.com/10.1007/BF00384745, doi:10.1007/BF00384745.

Pertermann, M., Hirschmann, M.M., 2003. Partial melting experiments on a MORB-like pyroxenite between 2 and 3 GPa: Constraints on the presence of pyroxenite in basalt source regions from solidus location and melting rate. Journal of Geophysical Research: Solid Earth 108, 1–17. doi:10.1029/2000jb000118.

Phillips, D., Clarke, W., Jaques, A.L., 2022. Age and origin of the West Kimberley lamproites, Western Australia. Lithos 432-433, 106913. URL: https://doi.org/10.1016/j.lithos.2022.106913, doi:10.1016/j.lithos.2022.106913.

Pintér, Z., Foley, S.F., Yaxley, G.M., 2022. Diamonds, dunites, and metasomatic rocks formed by melt/rock reaction in craton roots. Communications Earth and Environment 3, 1–8. doi:10.1038/s43247-022-00630-3.

Pintér, Z., Foley, S.F., Yaxley, G.M., Rosenthal, A., Rapp, R.P., Lanati, A.W., Rushmer, T., 2021. Experimental investigation of the composition of incipient melts in upper mantle peridotites in the presence of CO2 and H2O. Lithos 396-397, 106224. doi:10.1016/j.lithos.2021.106224.

Plank, T., 2005. Constraints from Thorium/Lanthanum on sediment recycling at subduction zones and the evolution of the continents. Journal of Petrology 46, 921–944. doi:10.1093/petrology/egi005.

Plank, T., Langmuir, C.H., 1998. The chemical composition of subducting sediment and its consequences for the crust and mantle. Chemical Geology 145, 325–394. doi:10.1016/S0009-2541(97)00150-2.

Powell, W., O'Reilly, S., 2007. Metasomatism and sulfide mobility in lithospheric mantle beneath eastern Australia: Implications for mantle Re-Os chronology. Lithos 94, 132–147. doi:10.1016/j.lithos.2006.06.010.

Powell, W., Zhang, M., O'Reilly, S.Y., Tiepolo, M., 2004. Mantle amphibole trace-element and isotopic signatures trace multiple metasomatic episodes in lithospheric mantle, western Victoria, Australia. Lithos 75, 141–171. doi:10.1016/j.lithos.2003.12.017.

Prelević, D., Akal, C., Foley, S.F., 2008a. Orogenic vs anorogenic lamproites in a single volcanic province: Mediterranean-type lamproites from Turkey. IOP Conference Series: Earth and Environmental Science 2, 012024. doi:10.1088/1755-1307/2/1/012024.

Prelević, D., Akal, C., Foley, S.F., Romer, R.L., Stracke, A., Van den Bogaard, P., 2012. Ultrapotassic mafic rocks as geochemical proxies for post-collisional dynamics of orogenic lithospheric mantle: The case of southwestern Anatolia, Turkey. Journal of Petrology 53, 1019–1055. doi:10.1093/petrology/egs008.

Prelević, D., Foley, S.F., 2007. Accretion of arc-oceanic lithospheric mantle in the Mediterranean: Evidence from extremely high-Mg olivines and Cr-rich spinel inclusions in lamproites. Earth and Planetary Science Letters 256, 120–135. doi:10.1016/j.epsl.2007.01.018.

Prelević, D., Foley, S.F., Cvetković, V., 2007. A review of petrogenesis of Mediterranean Tertiary lamproites: A perspective from the Serbian ultrapotassic province. Special Paper of the Geological Society of America 418, 113–129. doi:10.1130/2007.2418(06).

Prelević, D., Foley, S.F., Cvetković, V., L. Romer, R., 2004. The analcime problem and its impact on the geochemistry of ultrapotassic rocks from Serbia. Mineralogical Magazine 68, 633–648. doi:10.1180/0026461046840209.

Prelević, D., Foley, S.F., Romer, R., Conticelli, S., 2008b. Mediterranean tertiary lamproites derived from multiple source components in postcollisional geodynamics. Geochimica et Cosmochimica Acta 72, 2125–2156. doi:10.1016/j.gca.2008.01.029.

Prelević, D., Foley, S.F., Romer, R.L., Cvetković, V., Downes, H., 2005. Tertiary ultrapotassic volcanism in Serbia: Constraints on petrogenesis and mantle source characteristics. Journal of Petrology 46, 1443–1487. doi:10.1093/petrology/egi022.

Prelević, D., Jacob, D.E., Foley, S.F., 2013. Recycling plus: A new recipe for the formation of Alpine-Himalayan orogenic mantle lithosphere. Earth and Planetary Science Letters 362, 187–197. URL: https://www.sciencedirect.com/science/article/pii/S0012821X1200653X#aep-keywords-id18, doi:10.1016/j.epsl.2012.11.035.

Prelević, D., Stracke, A., Foley, S.F., Romer, R.L., Conticelli, S., 2010. Hf isotope compositions of Mediterranean lamproites: Mixing of melts from asthenosphere and crustally contaminated mantle lithosphere. Lithos 119, 297–312. doi:10.1016/j.lithos.2010.07.007.

Prider, R.T., 1939. Some minerals from the leucite-rich rocks of the West Kimberley area, Western Australia. Mineralogical Magazine and Journal of the Mineralogical Society 25, 373–387. URL: https://www.cambridge.org/core/article/some-minerals-from-the-leuciterich-rocks-of-the-west-kimberley-area-western-australia/79BE347327D000D424521C6508C4B851, doi:DOI:10.1180/minmag.1939.025.166.01.

Putirka, K., Jean, M., Cousens, B., Sharma, R., Torrez, G., Carlson, C., 2012. Cenozoic volcanism in the Sierra Nevada and Walker Lane, California, and a new model for lithosphere degradation. Geosphere 8, 265–291. doi:10.1130/GES00728.1.

Putirka, K.D., 2008. Thermometers and barometers for volcanic systems. Reviews in Mineralogy and Geochemistry 69, 61–120. doi:10.2138/rmg.2008.69.3.

Putnis, C.V., Geisler, T., Schmid-Beurmann, P., Stephan, T., Giampaolo, C., 2007. An experimental study of the replacement of leucite by analcime. American Mineralogist 92, 19–26. doi:10.2138/am.2007.2249.

Rawlinson, N., Davies, D.R., Pilia, S., 2017. The mechanisms underpinning Cenozoic intraplate volcanism in eastern Australia: Insights from seismic tomography and geodynamic modeling. Geophysical Research Letters 44, 9681–9690. URL: https://onlinelibrary.wiley.com/doi/abs/10.1002/2017GL074911, doi:10.1002/2017GL074911.

Rawlinson, N., Pilia, S., Young, M., Salmon, M., Yang, Y., 2016. Crust and upper mantle structure beneath southeast Australia from ambient noise and teleseismic tomography. Tectonophysics 689, 143–156. doi:10.1016/j.tecto.2015.11.034.

Rehfeldt, T., Foley, S.F., Jacob, D.E., Carlson, R.W., Lowry, D., 2008. Contrasting types of metasomatism in dunite, wehrlite and websterite xenoliths from Kimberley, South Africa. Geochimica et Cosmochimica Acta 72, 5722–5756. URL: http://dx.doi.org/10.1016/j.gca.2008.08.020, doi:10.1016/j.gca.2008.08.020.

Rey, P., 2001. From lithospheric thickening and divergent collapse to active continental rifting. Geological Society Special Publication 184, 77–88. doi:10.1144/GSL.SP.2001.184.01.05.

Robertson, A.D., Sutherland, F.L., Hollis, J.D., 1985. Upper mantle xenoliths and megacrysts and the origin of the Brigooda Basalt and Breccia, near Proston, Queensland. Papers (University of Queensland. Dept. of Geology) 11, 58 – 71. URL: https://espace.library.uq.edu.au/view/UQ:734631.

Robinson, J.A., Wood, B.J., 1998. The depth of the spinel to garnet transition at the peridotite solidus. Earth and Planetary Science Letters 164, 277–284. doi:10.1016/S0012-821X(98)00213-1.

Robinson, J.A., Wood, B.J., Blundy, J.D., 1998. The beginning of melting of fertile and depleted peridotite at 1.5 GPa. Earth and Planetary Science Letters 155, 97–111. doi:10.1016/s0012-821x(97)00162-3.

Rock, N.M.S., 1991. Lamprophyres. 1 ed., Springer, New York. doi:10.1007/978-1-4757-0929-2.

Rohrbach, A., Schmidt, M.W., 2011. Redox freezing and melting in the Earths deep mantle resulting from carbon-iron redox coupling. Nature 472, 209–214. doi:10.1038/nature09899.

Rosenthal, A., Foley, S.F., Pearson, D.G., Nowell, G.M., Tappe, S., 2009. Petrogenesis of strongly alkaline primitive volcanic rocks at the propagating tip of the western branch of the East African Rift. Earth and Planetary Science Letters 284, 236–248. doi:10.1016/j.epsl.2009.04.036.

Roux, J., Hamilton, D.L., 1976. Primary igneous analcite-an experimental study. Journal of Petrology 17, 244–257. doi:10.1093/petrology/17.2.244.

Rudnick, R.L., Gao, S., 2013. Composition of the Continental Crust. volume 4. 2 ed., Elsevier Ltd. URL: http://dx.doi.org/10.1016/B978-0-08-095975-7.00301-6, doi:10.1016/B978-0-08-095975-7.00301-6.

Rudnick, R.L., McDonough, W.F., Chappell, B.W., 1993. Carbonatite metasomatism in the northern Tanzanian mantle: petrographic and geochemical characteristics. Earth and Planetary Science Letters 114, 463–475. doi:10.1016/0012-821X(93)90076-L.

Sarkar, S., Dalton, H., Giuliani, A., Phillips, D., Graham Pearson, D., Nowell, G.M., Woodhead, J.D., Hergt, J., Maas, R., Lynton Jaques, A., Chalapathi Rao, N.V., Weiss, Y., Ghosh, S., 2025. Extreme enriched-mantle (EM) compositions recorded by the Sr-Nd-Hf isotopes of global cratonic lamproites. Geochimica et Cosmochimica Acta 394, 220–243. doi:10.1016/j.gca.2025.02.014.

Schmidt, M.W., 1996. Experimental constraints on recycling of potassium from subducted oceanic crust. Science 272, 1927. doi:10.1126/science.272.5270.1927.

Schmidt, M.W., Poli, S., 2003. Generation of Mobile Components during Subduction of Oceanic Crust. Treatise on Geochemistry 3-9, 567–591. doi:10.1016/B0-08-043751-6/03034-6.

Seton, M., Williams, S., Mortimer, N., Meffre, S., Micklethwaite, S., Zahirovic, S., 2019. Magma production along the Lord Howe Seamount Chain, northern Zealandia. Geological Magazine 156, 1605–1617. doi:10.1017/S0016756818000912.

Shea, J., Foley, S., Dalton, H., Lanati, A., Phillips, D., 2024. Mid-Jurassic volcanism at Bokhara River and insights into metasomatism in the lithospheric mantle of the Thomson Orogen, eastern Australia. Australian Journal of Earth Sciences 0, 1–13. URL: https://doi.org/10.1080/08120099.2024.2302360, doi:10.1080/08120099.2024.2302360.

Shea, J.J., Ezad, I.S., Foley, S.F., Lanati, A.W., 2022. The Eastern Australian Volcanic Province, its primitive melts, constraints on melt sources and the influence of mantle metasomatism. Earth-Science Reviews 233, 104168. URL: https://doi.org/10.1016/j.earscirev.

2022.104168, doi:10.1016/j.earscirev.2022.104168.

Shea, J.J., Foley, S.F., 2019. Evidence for a carbonatite-influenced source assemblage for intraplate basalts from the Buckland Volcanic Province, Queensland, Australia. Minerals 9. doi:10.3390/min9090546.

Shu, C., Foley, S.F., Ezad, I.S., Daczko, N.R., Shcheka, S.S., 2024. Experimental Melting of Phlogopite Websterite in the Upper Mantle between 1.5 and 4.5 GPa. Journal of Petrology 65. URL: https://academic.oup.com/petrology/article/doi/10.1093/petrology/egae030/7631318, doi:10.1093/petrology/egae030.

Shu, C., Foley, S.F., Shea, J.J., Lanati, A.W., Daczko, N.R., Shcheka, S.S., in revision. Short timeframe between formation and remelting of the phlogopite websterite source for leucitites along earth's longest continental hotspot track.

Smith, B.W., Prescott, J.R., 1987. Thermoluminescence dating of the eruption at Mt Schank, South Australia. Australian Journal of Earth Sciences 34, 335–342. doi:10.1080/08120098708729415.

Stonier, G.A., 1893. On the Occurrence of Leucite-Basalt at Lake Cudgellico (Cargelligo). Records of the Geological Survey of New South Wales 3, 71–74.

Stracke, A., Bourdon, B., 2009. The importance of melt extraction for tracing mantle heterogeneity. Geochimica et Cosmochimica Acta 73, 218–238. URL: http://dx.doi.org/10.1016/j.gca.2008.10.015, doi:10.1016/j.gca.2008.10.015.

Sudholz, Z.J., Reddicliffe, T.H., Jaques, A.L., Yaxley, G.M., Haynes, M., Gorbatov, A., Czarnota, K., Frigo, C., Maas, R., Knowles, B., 2023. Petrology, Age, and Rift Origin of Ultramafic Lamprophyres (Aillikites) at Mount Webb, a New Alkaline Province in Central Australia. Geochemistry, Geophysics, Geosystems 24, 1–29. doi:10.1029/2023GC011120.

Sudo, A., Tatsumi, Y., 1990. Phlogopite and K-amphibole in the upper mantle: Implication for magma genesis in subduction zones. Geophysical Research Letters 17, 29–32. URL: https://agupubs.onlinelibrary.wiley.com/doi/10.1029/GL017i001p00029, doi:10.1029/GL017i001p00029.

Sutherland, F.L., 1983. Timing, trace and origin of basaltic migration in eastern Australia. Nature 305, 123–126. URL: https://doi.org/10.1038/305123a0, doi:10.1038/305123a0.

Sutherland, F.L., 1996. Alkaline rocks and gemstones, Australia: A review and synthesis. Australian Journal of Earth Sciences 43, 323–343. doi:10.1080/08120099608728259.

Sutherland, F.L., 2003. 'Boomerang' migratory intraplate Cenozoic volcanism, eastern Australian rift margins and the Indian-Pacific mantle boundary. Special Paper of the Geological Society of America 372, 203–221. doi:10.1130/0-8137-2372-8.203.

Sutherland, F.L., Barron, L.M., 2003. Diamonds of multiple origins from New South Wales: Further data and discussion. Australian Journal of Earth Sciences 50, 975–981. doi:10.1111/j.1400-0952.2003.01038.x.

Sweeney, R.J., Thompson, A.B., Ulmer, P., 1993. Phase relations of a natural MARID composition and implications for MARID genesis, lithospheric melting and mantle metasomatism. Contributions to Mineralogy and Petrology 115, 225–241. doi:10.1007/BF00321222.

Takahashi, E., 1986. Melting of a dry peridotite KLB-1 up to 14 GPa: Implications on the Origin of peridotitic upper mantle. Journal of Geophysical Research 91, 9367. doi:10.1029/jb091ib09p09367.

Tappe, S., Foley, S.F., Jenner, G.A., Kjarsgaard, B.A., 2005. Integrating ultramafic lamprophyres into the IUGS classification of igneous rocks: Rationale and implications. Journal of Petrology 46, 1893–1900. doi:10.1093/petrology/egi039.

Tappe, S., Romer, R.L., Stracke, A., Steenfelt, A., Smart, K.A., Muehlenbachs, K., Torsvik, T.H., 2017. Sources and mobility of carbonate melts beneath cratons, with implications for deep carbon cycling, metasomatism and rift initiation. Earth and Planetary Science Letters 466, 152–167. URL: http://dx.doi.org/10.1016/j.epsl.2017.03.011, doi:10.1016/j.epsl.2017.03.011.

Tappe, S., Shaikh, A.M., Wilson, A.H., Stracke, A., 2022. Evolution of ultrapotassic volcanism on the Kaapvaal craton: deepening the orangeite versus lamproite debate. Geological Society Special Publication 513, 17–44. doi:10.1144/SP513-2021-84.

Tapu, A.T., Ubide, T., Vasconcelos, P.M., 2023. Increasing complexity in magmatic architecture of volcanoes along a waning hotspot. Nature Geoscience 16, 371–379. doi:10.1038/s41561-023-01156-9.

Thomson, A.R., Walter, M.J., Kohn, S.C., Brooker, R.A., 2016. Slab melting as a barrier to deep carbon subduction. Nature 529, 76–79. doi:10.1038/nature16174.

Thomson, A.R., Walter, M.J., Lord, O.T., Kohn, S.C., 2014. Chemistry and mineralogy of earth's mantle. Experimental determination of melting in the systems enstatite-magnesite and magnesite-calcite from 15 to 80 GPa. American Mineralogist 99, 1544–1554. doi:10.2138/am.2014.4735.

Tiepolo, M., Oberti, R., Zanetti, A., Vannucci, R., Foley, S.F., 2007. Trace-element partitioning between amphibole and silicate melt. Reviews in Mineralogy and Geochemistry 67, 417–452. doi:10.2138/rmg.2007.67.11.

Tilley, C.E., 1950. Some aspects of magmatic evolution. Quarterly Journal of the Geological Society of London 106, 37–61. doi:10.1144/GSL.JGS.1950.106.01-04.04.

Toyokuni, G., Zhao, D., 2024. Slab-Plume Interactions Beneath Australia and New Zealand: New Insight From Whole-Mantle Tomography. Geochemistry, Geophysics, Geosystems 25. doi:10.1029/2024GC011739.

Trønnes, R.G., 2002. Stability range and decomposition of potassic richterite and phlogopite end members at 5-15 GPa. Mineralogy and Petrology 74, 129–148. doi:10.1007/s007100200001.

Turner, S., Foden, J., George, R., Evans, P., Varne, R., Elburg, M., Jenner, G., 2003. Rates and processes of potassic magma evolution beneath Sangeang Api Volcano, East Sunda Arc, Indonesia. Journal of Petrology 44, 491–516. doi:10.1093/petrology/44.3.491.

Van Keken, P.E., Hacker, B.R., Syracuse, E.M., Abers, G.A., 2011. Subduction factory: 4. Depth-dependent flux of H2O from subducting slabs worldwide. Journal of Geophysical Research: Solid Earth 116. doi:10.1029/2010JB007922.

Veter, M., Foley, S.F., Mertz-Kraus, R., Groschopf, N., 2017. Trace elements in olivine of ultramafic lamprophyres controlled by phlogopite-rich mineral assemblages in the mantle source. Lithos 292-293, 81–95. doi:10.1016/j.lithos.2017.08.020.

Wade, A., Prider, R.T., 1940. The leucite-bearing rocks of the West Kimberley area, Western Australia. Quarterly Journal of the Geological Society of London 96, 39. URL: https://www.lyellcollection.org/doi/10.1144/GSL.JGS.1940.096.01-04.04, doi:10.1144/GSL.JGS.1940.096.01-04.04.

Walter, M., 1998. Melting of Garnet Peridotite and the Origin of Komatiite and Depleted Lithosphere. Journal of Petrology 39, 29–60. doi:10.1093/petrology/39.1.29.

Wang, K., Plank, T., Walker, J.D., Smith, E.I., 2002. A mantle melting profile across the Basin and Range, SW USA. Journal of Geophysical Research: Solid Earth 107. doi:10.1029/2001jb000209.

Wang, Q., Wyman, D.A., Xu, J.F., Zhao, Z.H., Jian, P., Xiong, X.L., Bao, Z.W., Li, C.F., Bai, Z.H., 2006. Petrogenesis of Cretaceous adakitic and shoshonitic igneous rocks in the Luzong area, Anhui Province (eastern China): Implications for geodynamics and Cu-Au mineralization. Lithos 89, 424–446. URL: https://www.sciencedirect.com/science/article/pii/S0024493706000302#aep-acknowledgment-id44, doi:10.1016/j.lithos.2005.12.010.

Wang, X., Wang, Z., Cheng, H., Zong, K., Wang, C.Y., Ma, L., Cai, Y.C., Foley, S., Hu, Z., 2022. Gold endowment of the metasomatized lithospheric mantle for giant gold deposits: Insights from lamprophyre dykes. Geochimica et Cosmochimica Acta 316, 21–40. URL: https://doi.org/10.1016/j.gca.2021.10.006, doi:10.1016/j.gca.2021.10.006.

Wang, Y., Foley, S.F., 2018. Hybridization Melting Between Continent-Derived Sediment and Depleted Peridotite in Subduction Zones. Journal of Geophysical Research: Solid Earth 123, 3414–3429. doi:10.1029/2018JB015507.

Wang, Y., Foley, S.F., Buhre, S., Soldner, J., Xu, Y., 2021. Origin of potassic postcollisional volcanic rocks in young, shallow, blueschist-rich lithosphere. Science Advances 7. doi:10.1126/sciadv.abc0291.

Wang, Y., Prelević, D., Buhre, S., Foley, S.F., 2017. Constraints on the sources of post-collisional K-rich magmatism: The roles of continental clastic sediments and terrigenous blueschists. Chemical Geology 455, 192–207. doi:10.1016/j.chemgeo.2016.10.006.

Wang, Z.N., Wang, Y., Sossi, P., He, Y., Peng, Y., Lu, W.N., Wu, H., 2024. Calcium isotopic composition of the bulk silicate Earth: A komatiite perspective. Lithos 480-481, 107638. URL: https://doi.org/10.1016/j.lithos.2024.107638, doi:10.1016/j.lithos.2024.107638.

Wang, Z.X., Liu, S.A., Prelević, D., Li, S., Wang, Z.Z., Wu, T., Liu, J., 2025. Mg, Zn and Fe isotope evidence for derivation of K-rich basalts from the mantle hybridized by recycled carbonate-bearing silicate sediments. Geochimica et Cosmochimica Acta 394, 244–257. doi:10.1016/j.gca.2025.02.016.

Warr, L.N., 2021. IMA–CNMNC approved mineral symbols. Mineralogical Magazine 85, 291–320. doi:10.1180/mgm.2021.43.

Wass, S.Y., 1979a. Fractional crystallization in the mantle of late-stage kimberlitic liquids—evidence in xenoliths from the Kiama Area, N.S.W., Australia, in: The Mantle Sample: Inclusion in Kimberlites and Other Volcanics. American Geophysical Union, Washington, D. C.. volume 16, pp. 366–373. URL: http://doi.wiley.com/10.1029/SP016p0366, doi:10.1029/SP016p0366.

Wass, S.Y., 1979b. Multiple origins of clinopyroxenes in alkali basaltic rocks. Lithos 12, 115–132.

Wass, S.Y., Henderson, P., Elliot, C.J., 1980. Chemical heterogeneity and metasomatism in the upper mantle: evidence from rare earth and other elements in apatite-rich xenoliths in basaltic rocks from eastern Australia. Philosophical Transactions of the Royal Society of London. Series A, Mathematical and Physical Sciences 297, 333–346. URL: https://royalsocietypublishing.org/doi/10.1098/rsta.1980.0219, doi:10.1098/rsta.1980.0219.

Wass, S.Y., Rogers, N.W., 1980. Mantle metasomatism-precursor to continental alkaline volcanism. Geochimco ct Cosmorhrmco Acra 44, 1811–1823.

Wellman, P., Cundari, A., McDougall, I., 1970. Potassium – argon ages for leucite-bearing rocks from New South Wales, Australia. Journal and Proceedings ofthe Royal Society ofNew South Wales 103, 103–107.

Wellman, P., McDougall, I., 1974. Potassium-argon ages on the cainozoic volcanic rocks of New South Wales. Journal of the Geological Society of Australia 21, 247–272. doi:10.1080/00167617408728849.

Wheller, G., Varne, R., Foden, J., Abbott, M., 1987. Geochemistry of quaternary volcanism in the Sunda-Banda arc, Indonesia, and three-component genesis of island-arc basaltic magmas. Journal of Volcanology and Geothermal Research 32, 137–160. URL: https://linkinghub.elsevier.com/retrieve/pii/0377027387900412, doi:10.1016/0377-0273(87)90041-2.

Wilkinson, J.F., 1975. Ultramafic inclusions and high pressure megacrysts from a nephelinite sill, Nandewar Mountains, north-eastern New South Wales, and their bearing on the origin of certain ultramafic inclusions in alkaline volcanic rocks. Contributions to Mineralogy and Petrology 51, 235–262. doi:10.1007/BF00372144.

Wilkinson, J.F.G., Hensel, H.D., 1991. An analcime mugearite-megacryst association from north-eastern New South Wales: implications for high-pressure amphibole-dominated fractionation of alkaline magmas. Contributions to Mineralogy and Petrology 109, 240–251. URL: http://link.springer.com/10.1007/BF00306482, doi:10.1007/BF00306482.

Willbold, M., Stracke, A., 2006. Trace element composition of mantle end-members: Implications for recycling of oceanic and upper and lower continental crust. Geochemistry, Geophysics, Geosystems 7, 1–30. doi:10.1029/2005GC001005.

1665 Williams, L.A.J., 1982. Physical aspects of magmatism in continental rifts, in: Pálmason, G. (Ed.), Continental and Oceanic Rifts. volume 8,
1666 pp. 193–222. URL: http://www.agu.org/books/gd/v008/GD008p0193/GD008p0193.shtml, doi:10.1029/GD008p0193.
1667 Winterburn, P.A., Harte, B., Gurney, J.J., 1990. Peridotite xenoliths from the Jagersfontein kimberlite pipe: I. Primary and primary-
1668 metasomatic mineralogy. Geochimica et Cosmochimica Acta 54, 329–341. doi:10.1016/0016-7037(90)90322-C.
1669 Woolley, A.R., Bergman, S.C., Edgar, A.D., Le Bas, M.J., Mitchell, R.H., Rock, N.M., Scott Smith, B.H., 1996. Classification of
1670 lamprophyres, lamproites, kimberlites, and the kalsilitic, melilitic, and leucitic rocks. Canadian Mineralogist 34, 175–186.
1671 Yang, J.H., Sun, J.F., Chen, F., Wilde, S.A., Wu, F.Y., 2007. Sources and petrogenesis of late triassic dolerite dikes in the Liaodong
1672 Peninsula: Implications for post-collisional lithosphere thinning of the eastern North China Craton. Journal of Petrology 48, 1973–1997.
1673 doi:10.1093/petrology/egm046.
1674 Yaxley, G.M., Crawford, A.J., Green, D.H., 1991. Evidence for carbonatite metasomatism in spinel peridotite xenoliths from western
1675 Victoria, Australia. Earth and Planetary Science Letters 107, 305–317. doi:10.1016/0012-821X(91)90078-V.
1676 Yaxley, G.M., Green, D.H., Kamenetsky, V., 1998. Carbonatite metasomatism in the southeastern Australian lithosphere. Journal of
1677 Petrology 39, 1917–1930. doi:10.1093/petroj/39.11-12.1917.
1678 Yaxley, G.M., Kamenetsky, V., Green, D.H., Falloon, T.J., 1997. Glasses in mantle xenoliths from western Victoria, Australia, and their
1679 relevance to mantle processes. Earth and Planetary Science Letters 148, 433–446. doi:10.1016/s0012-821x(97)00058-7.
1680 Zhang, M., O'Reilly, S.Y., 1997. Multiple sources for basaltic rocks from Dubbo, eastern Australia: Geochemical evidence for plume-
1681 lithospheric mantle interaction. Chemical Geology 136, 33–54. doi:10.1016/S0009-2541(96)00130-1.
1682 Zhang, M., O'Reilly, S.Y., Chen, D., 1999. Location of Pacific and Indian mid-ocean ridge-type mantle in two time slices: Evidence from
1683 Pb, Sr, and Nd isotopes for Cenozoic Australian basalts. Geology 27, 39–42. doi:10.1130/0091-7613(1999)027<0039:LOPAIM>2.3.CO;2.
1684 Zhang, M., Stephenson, P.J., O'Reilly, S.Y., McCulloch, M.T., Norman, M., 2001. Petrogenesis and geodynamic implications of late
1685 Cenozoic basalts in North Queensland, Australia: Trace-element and Sr-Nd-Pb Isotope Evidence. Journal of Petrology 42, 685–719.
1686 doi:10.1093/petrology/42.4.685.
1687 Zinngrebe, E., Foley, S.F., 1995. Metasomatism in mantle xenoliths from Gees, West Eifel, Germany: Evidence for the genesis of calc-alkaline
1688 glasses and metasomatic Ca-enrichment. Contributions to Mineralogy and Petrology 122, 79–96. doi:10.1007/s004100050114.

Figure captions

Fig. 1. (a) Distribution of the EAVP (green) and EAPS (orange) outcrops as defined in Shea et al. (2022) and this contribution, respectively. Map coloured by depth of the lithosphere-asthenosphere boundary (LAB) from Rawlinson et al. (2017). Orogenic blocks (grey lines) and the western boundary of the Tasmanides (red dashed line) inferred to demarcate cratonic Australia to the west and orogenic Australia to the east from Glen et al. (2016); note mismatch to LAB depth where the 180 km contour is used by geophysical studies (Hoggard et al., 2020). Yellow line = the interpreted path of the Cosgrove plume (Davies et al., 2015) with inferred offshore progression of the plume (dotted line); open circles along the path mark the approximate locations of the outcrops with preferred ages as described in Cohen et al. (2008). (b) Zoom of Eastern Australia that also shows the location of the basanitic diatremes from Bokhara River (orange diamond) (Shea et al., 2024), leucite-bearing lavas at Jugiong and Harden (Harvey and Joplin, 1940), and EAPS sample areas (white boxes). Panels (c), (d), and (e) show the north, central and southern field areas and EAPS sample locations (pink circles) of this study. Dashed black lines = LAB contours at 120 and 150 km. These depths are commonly inferred to represent the depth of melting for the source assemblages of the leucite–bearing EAPS lavas. The volcanic fields around Shepparton from Paul et al. (2005) are included in (e), while the Mount Webb aillikites of Sudholz et al. (2023) are shown in (a) along with kimberlites of the Adelaide Fold Belt (*AFB*; Dalton et al., 2025), and Kimberley block kimberlites and *(Cenozoic)* West Kimberley lamproites (Jaques et al., 1984, 1986); the chemistry of these lavas are compared with the EAPS lavas in text. Abbreviations: Cratonic Australia (CrA); Delamarian orogen (DO); Lachlan orogen (LO); Mossman orogen (MO); New England orogen (NEO); Sydney–Gunnedah–Bowen basin (SGBB); and Thomson orogen (ThO).

Fig. 2. Summary of petrographic textures and phases of the EAPS. Selected samples arranged north to south starting with (a) 0901 – Byrock, (b) 0801 – El Capitan, (c) 1402x4 – Wallaroy Hill, (d) 2202 – Lake Cargelligo, (e) 0102 – Lake Cargelligo, and (f) 2001 – Pine Lodge (Cosgrove). Coloured circles in top right of each panel correspond to the colour scale used for the EAPS samples in all geochemical plots; see Figure 3. Key features include porphyritic texture of (a) compared to a more equigranular texture in (b); (a) including small ($<$ 20 μm) apatite and carbonate grains entrained in poikilitic phlogopite. (d) shows prevalence of sanidine in some samples, also contrasting the porphyritic texture of (a). (c) and (e) show examples of where nepheline is present, highlighting the restricted formation in melt pools (glass). (f) displays highly altered texture of Pine Lodge (Cosgrove), with most olivine converted to iddingsite and only rare olivine cores preserved. Diopside and phlogopite are also present at Pine Lodge (f); diopside appears fluid mediated with spindly, wavy forms and all leucite at least partly transformed to analcime. Multiple labels for the same mineral present in (a) – (f) highlight varying forms, textures, and sizes within the sample. All images are plane polarised light on thin sections ($\approx$30 μm) except (c) which is a thick section ($>$ 100 μm). Large anhedral olivine are xenocrysts e.g. (b), (d), and (e). Mineral abbreviations used are the IMA-CNMNC approved symbols (Miyawaki et al., 2021), taken from the compilation of (Warr, 2021). Anl = Analcime; Di = Diopside; Idd = Iddingsite; Lct = Leucite; Nph = Nepheline; Ol = Olivine; Phl = Phlogopite; Rct = Richterite; Sa = Sanidine.

Fig. 3. Major element discrimination diagrams showing data from this study in (a) unnormalised total–alkali versus silica (TAS), (b) K_2O vs. Na_2O, and (c) K_2O vs. Si_2O space. Note: that for volatile–rich (i.e. $H_2O^+ \geq$ 2wt% and $CO_2 \geq$ 0.5 wt%, or LOI $\geq$ 2.5 wt% (Le Maitre et al., 2002)) samples like ours the TAS cannot be used for classification purposes, but is provided for a general comparison. TAS (a) after Tilley (1950) with volcanic rock classification fields (Le Bas et al., 1986), and alkalinity divide (label: *A–SA;* Irvine and Baragar, 1971). Potassium–sodium diagram (b) after Middlemost (1975); ultrapotassic field divide follows Foley et al. (1987). Potassium–silica diagram (c) after Middlemost (1975) and Peccerillo and Taylor (1976); dividing lines and field names of Wheller et al. (1987). Range of published EAVP data that passes chemical screens *(see text for specifics)* represented by polygons (darkest grey); i.e. highest density of points usually $>$ 80% of all analyses. EAPS symbols (large circles) coloured by latitude in (a)–(c). Data sources: Shea et al. (2022)(EAVP and EAPS Lit); Shea et al. (2024) (Bokhara River); Sudholz et al. (2023) (Webb Aillikites); Paul et al. (2005) (Pine Lodge and Shepparton); Sarkar et al. (2025)

(anorogenic lamproites only); Casalini et al. (2022) (orogenic and anorogenic lamproites); Farmer et al. (2002) (Sierra Nevada leucitites); Plank (2005) (Arcs); Willbold and Stracke (2006) (OIBs); Palme and O'Neill (2013) (primitive mantle (PM)); McDonough (1990) (sub–continental lithospheric mantle (SCLM)); Gale et al. (2013) (N-MORB). Roman province and selected kimberlites compiled from GEOROC database (**https://georoc.eu/**; version 2023-12-01). Full list of data references in the Supplement.

Fig. 4. Major element 'Harker' variation diagrams displaying all major and selected minor elements against MgO wt% with EAPS lavas plotted together with published data. EAVP prim point density polygon covers > 80% of all analyses in most cases. Data sources for published literature as in Figure 3; full references in the Supplement.

Fig. 5. Alkaline major element variation diagrams and select trace elements against MgO wt% for EAPS lavas and published data. EAVP prim point density polygon covers > 80% of all analyses in most cases. Data sources for published literature as in Figure 3; full references in the Supplement.

Fig. 6. Lamproite discrimination diagrams as defined by Foley et al. (1987), showing the EAPS lavas analysed in this study compared to values for other alkaline lavas. Group I, II, and III refer to I – lamproites, II – kamafugites, III – leucitites (Foley et al., 1987). Coloured pentagons correspond to high-pressure hydrous pyroxenite experiments from Shu et al. (2024) and Shu et al. (in revision). Note the EAPS lavas south of Griffith (34°S; yellow and orange circles) are not ultrapotassic. Pyroxenite and peridotite partial melt divide is plotted in (b) as shown in Herzberg (2011) and Herzberg and Asimow (2008). Data sources for published literature as in Figure 3; full references in the Supplement.

Fig. 7. Trace element variation diagrams with measured trace elements normalised to primitive mantle (PM) values from Palme and O'Neill (2013). All panels show new analyses from this study coloured by latitude with N–MORB values from Gale et al. (2013) and SCLM values from McDonough (1990) included for reference. Panels (b) – (d) shows EAPS comparison with published values for other Australian lavas; (b) published EAPS (note variability in the number of points per element) and the Shepparton lavas analysed by Paul et al. (2005); (c) EAVP primitive lavas; and (d) Bokhara River basanite and Mount Webb ailikite (orange and yellow diamonds, respectively). (d) also includes West Greenland kimberlites (black crosses and grey band; Tappe et al., 2017). The grey bands in panels (c)–(h) represent the absolute range for the dataset plotted within the band; the average pattern for each dataset shown as line with symbol. (a) EAPS (this study); (b) EAPS published values; (c) EAVP primitive lavas; (d) Bokhara, UML & Kimberlite; (e) Anorogenic lamproites (Casalini et al. (2022) only; comparison between Sarkar et al. (2025) and Casalini et al. (2022) in Supplementary Figure 2); (f) Orogenic lamproites; (g) Roman Province leucitites; (h) Sierra Nevada leucitites. Data sources for published literature as in Figure 3; full references in the Supplement.

Fig. 8. Volatile element results plotted against relevant trace element ratios or Mg#. H_2O (a) and N (b) are plotted against Ba/La based on similar behaviour and likely source (sediments). Sulfur (c) shows a degree of degassing with samples from the same outcrops showing both high and low-S for similar Mg#. CO_2 (d) also exhibits degassing, but still overlaps with global lamproites, lamprophyres, and some kimberlites. Colours for EAPS (this study) follow the scale plotted on panel (d). Published values are screened for Mg# $\geq$ 55 and represent converted total abundances for all species of that element reported. Data sources:"All MORB" in (b) from Johnson and Goldblatt (2015) and Gale et al. (2013); GEOROC precompiled files (kimberlites, peridotites, pyroxenites, lamproites, lamprophyres, and leucitites); kimberlites from Tappe et al. (2017) highlighted in black; Jia2003 (N-only; lamproites and lamprophyres; Jia et al. (2003)). Full reference list for GEOROC files in the Supplement.

Fig. 9. FeO_T/MnO vs. MgO source component discrimination diagram with grey box showing the range of values for partial melts from an anhydrous peridotite source defined by Herzberg (2011). Melts outside this range are inferred to be generated by pyroxenite partial melts. EAVP prim point density polygon covers > 80% of all analyses. Data sources for published literature as in Figure 3; full references in the Supplement.

Fig. 10. Mantle source lithologies in (log-scale) TiO_2 versus total alkali ($Na_2O + K_2O$) from experimentally derived partial melt (inset legend); compilation after Shea et al. (2022). EAPS and comparison datasets included for context. EAVP prim point density polygon covers > 80% of all analyses. Data sources for published literature as in Figure 3; full references in the Supplement.

Fig. 11. Calculated temperatures vs latitude south (a) and depth (b) for the EAPS Lavas (colour scale in (a); orange diamonds = Bokhara River basanites). Dashed coloured lines in (a) show averages for north, central, and south EAPS; open black and grey circles represent age-progressive (plume related) and non-age-progressive EAVP basalts, respectively (full references in the Supplement; Shea et al., 2022). Grey fields in (b) are the LAB depths beneath eastern Australia, while coloured lines are experimentally determined solidi for mantle assemblages compared with the SEAG (black solid and dashed line) and mantle adiabats (dotted lines below 3.5 GPa). Dark grey dot-dash line intercepting 6 GPa = graphite (Gr) to diamond (Di) stability line (Day, 2012). Reduced peridotite solidus below 2 GPa and dry pyroxenite (MIX1G) solidus roughly follow K01 and KD, respectively (Foley et al., 2009; Pintér et al., 2021; Kogiso et al., 2003). Dashed pressure error bar = EAPS, solid = EAVP (Rawlinson et al., 2017). Data sources: F09 = Foley et al. (2009) oxidised peridotite; G14 = Green et al. (2014) pyrolite +0.4 wt% H_2O; F22 = Foley et al. (2022) hydrous pyroxenite; S23 = Shu et al. (2024) phlogopite-websterite; CM = phlogopite lherzolite (Condamine and Médard, 2014; Condamine et al., 2016); K01 and KD = 0.1 wt% H_2O and dry lherzolite (Katz et al., 2003); TQ = Tinaquillo (depleted) lherzolite (Robinson et al., 1998; Robinson and Wood, 1998); W98 = KR43004 fertile lherzolite (Walter, 1998).

Fig. 12. Dominant mantle source trace element ratio discrimination plots of the EAPS showing **(a)** Nb vs. Nb/U indicating primitive-mantle derived magmas; Nb/U is sensitive to crustal contamination; mantle array from Hofmann et al. (1986). **(b)** Nb/Yb vs. Th/Yb showing mantle array and arrows illustrating subduction enrichment, assimilation and fractional crystallisation (FC, AFC), and intraplate enrichment after Ersoy et al. (2014) and Pearce (1983). **(c)** Sr/Rb vs. Ba/Rb with phlogopite- and amphibole-bearing source compositional vectors (arrows) after Furman and Graham (1999). **(d)** La/Nb vs. Tb/Yb with garnet and inferred source melt depth arrows, after Wang et al. (2002). Reference values: PM (Palme and O'Neill, 2013); MORBs (Gale et al., 2013); SCLM (McDonough, 1990); UCC (Rudnick and Gao, 2013); Arcs (Plank, 2005); OIBs (Willbold and Stracke, 2006); and GLOSS (Plank and Langmuir, 1998). EAVP prim point density polygon covers > 80% of all analyses. Data sources for published literature as in Figure 3; full references in the Supplement.

Fig. 13. Trace element ratio demarcation plots of the EAPS showing **(a)** Primitive mantle-normalised La/Yb vs. Ti/Eu displaying carbonatite and silicate metasomatism end-members compared to carbonatite metasomatised xenoliths (shaded green rectangle) from Yaxley et al. (1991); after Coltorti et al. (1999); Klemme et al. (1995); Rudnick et al. (1993). **(b)** Primitive mantle-normalised La/Sm, as an indicator of mantle source enrichment, versus Ba/La for identifying melts associated with subduction related slab fluids, after Aldanmaz et al. (2000) and Elliott et al. (1997). **(c)** La/Nb vs. Ba/Nb plotted with arrows showing general trends expected for melting with pelagic sediments, melts derived from mixed source, and arc-style melting. **(d)** La vs. La/Yb showing source enrichment, partial melt/ melt degree, and fractionation trends. Reference values: PM (Palme and O'Neill, 2013); MORBs (Gale et al., 2013); SCLM (McDonough, 1990); UCC (Rudnick and Gao, 2013); Arcs (Plank, 2005); OIBs (Willbold and Stracke, 2006); and GLOSS (Plank and Langmuir, 1998). EAVP prim point density polygon covers > 80% of all analyses. Data sources for published literature as in Figure 3; full references in the Supplement.

Fig. 14. LAB depth and seismic tomography profiles (a) along the Cosgrove track, (b) Byrock latitude, (c) through Lake Cargelligo and Tullibigeal, and (d) at Pine lodge with volcano locations projected on each transect. Transect location and direction are indicated in (e) along with the orogenic boundaries, volcanic fields of the EAVP (Shea et al., 2022), and 180 km LAB depth contour that roughly indicates the edge of cratonic Australia (Hoggard et al., 2020). Grey stars (b)–(e) show deepest LAB ridge position under each field noting the position relative to the volcano at the surface; yellow star in (d) shows isolated LAB ridge creating a melt channel beneath Pine Lodge. Insets show a schematic representation of the petro-geodynamic environment under Byrock (i), and Tullibigeal to Pine Lodge (ii). UML = ultra-mafic

lamprophyre; PGW = phlogopite-garnet websterite; green gradient above LAB represents degree of metasomatism with cross-cutting veins providing a conduit for melt extraction; black arrows show direction of mantle flow relative to plate motion, and EDC cells. Plumbing systems (grey ellipses) beneath Bokhara River with xenoliths (i) and the Newer Volcanic Province (ii). In (a)–(d) the warm colours represent slow regions while cool colours show fast regions. Tomography sections beneath the EAPS in (a)–(d) come from high-resolution regional data by Rawlinson et al. (2017), while the section in (a) from -27° – -20° is lower resolution global data from de Laat et al. (2023). Volcano colours follow colour scales on geochemical plots (Tindarey = purple; Tullibigeal = pink; Shepparton = yellow), with the exception of Buckland (black) and the broader EAVP basalt (grey) volcanoes.